

MECHANICAL BEHAVIOR OF PARTICULATE SYSTEMS:
EXPERIMENTS AND MODELING

By

CLAUDIA V. GENOVESE

A DISSERTATION PRESENTED TO THE GRADUATE SCHOOL
OF THE UNIVERSITY OF FLORIDA IN PARTIAL FULFILLMENT
OF THE REQUIREMENTS FOR THE DEGREE OF
DOCTOR OF PHILOSOPHY

UNIVERSITY OF FLORIDA

2003

Copyright 2003

by

Claudia V. Genovese

ACKNOWLEDGMENTS

I am profoundly grateful to my advisor, Dr. Ray Bucklin, and my co-advisor, Dr. Oana Cazacu, for scientific guidance, material support and endless patience. I also would like to thank Dr. Nicolaie Cristescu for his continuous help. I extend my gratitude to Dr. Murat Balaban and Dr. Arthur Teixeira who were very kind to advise me and guide me during the first year in this country and now for taking the time to read this dissertation and to make comments on it.

I express my gratitude to Dr. Raluca Rosca for her help and advice in the numerical simulations. I also thank the following: the Engineering Research Center for funding this project; the ERC faculty; and the Agricultural and Biological Engineering Department and staff for their assistance.

I am thankful for the love and support of my husband, family and friends.

TABLE OF CONTENTS

	<u>page</u>
ACKNOWLEDGMENTS	iii
LIST OF TABLES	vii
LIST OF FIGURES.....	viii
ABSTRACT.....	xiv
 CHAPTER	
1 INTRODUCTION.....	1
2 BACKGROUND.....	4
2.1 Introduction	4
2.2 Literature Review	5
2.3 Constitutive Models.....	11
2.3.1 The von Mises and Drucker-Prager Models.....	12
2.3.2 Cam-clay Model	14
2.3.3 Cap Model	16
2.3.4 Lade Model (1977)	19
2.3.5 Advantages and Shortcomings of the Existing Models	22
3 SHEAR CELL TESTERS	25
3.1 Introduction	25
3.2 Direct Shear Testers.....	25
3.2.1 The Jenike Shear Tester	27
3.2.2 Test Protocol and Data Reduction	27
3.2.3 Other Testing Devices.....	31
3.3 Indirect Shear Tester	33
3.3.1 Uniaxial Compression.....	33
3.3.2 Biaxial Compression Tester	39
3.3.3 Triaxial Compression Tester	41
4 EXPERIMENTAL STUDY OF THE QUASI-STATIC DEFORMATION OF DRY SILICA POWDER.....	43
4.1 Introduction	43

4.2 Methodology and Experimental Set up.....	44
4.2.1 Background.....	45
4.2.2 Testing Procedure	45
4.2.3 System under Study	47
4.3 Results of Monotonic Deviatoric Tests on Silica	48
4.4 Results on Cyclic Deviatoric Tests.....	56
4.5 Modeling the Behavior in the Elastic Regime.....	60
4.6 Modeling the Observed Irreversibility in Behavior using Elastic/Perfect Plastic Models	65
4.7 Two-Surface Elastic/Plastic Model, Lade(1977)	67
4.7.1 Determination of the Plastic Collapse Strain Increment	68
4.7.2 Flow Rule for Hydrostatic Conditions.....	75
4.7.3 Determination of the Plastic Expansive Strain Increment	76
4.7.4 Flow Rule for Deviatoric Conditions.....	77
4.7.5 Work Hardening Law.....	82
4.8 Summary of the Parameters involved in Lade Model (1977) and the Corresponding Numerical Values for Silica Powder.....	84
 5 STUDY OF THE QUASI-STATIC DEFORMATION OF DRY POLYMER PELLETS	 87
5.1 Introduction	87
5.2 Experimental Program	87
5.2.1 System under Study	87
5.2.2 Methodology.....	88
5.3 Results of Monotonic Deviatoric Tests.....	88
5.4 Results of Cyclic Deviatoric Tests	93
5.5 Modeling the Behavior in the Elastic Regime.....	96
5.6 Modeling the Observed Irreversibility in Behavior using Elastic/Perfect Plastic Models.....	98
5.7 Two-Surface Elastic/Plastic Model	100
5.7.1 Determination of the Plastic Collapse Strain Increment	100
5.7.2 Determination of the Plastic Expansive Strain Increment	101
5.7.3 Flow Rule for Deviatoric Conditions.....	103
5.7.4 Work Hardening Law.....	104
5.8 Summary of the Parameters involved in Lade Model (1977) and the Corresponding Numerical Values for PE Pellets	106
 6 NUMERICAL SIMULATION	 109
6.1 Introduction	109
6.2 Numerical Considerations.....	110
6.3 The Closest Point Projection Algorithm and its Application to the Integration of Drucker-Prager Model	113
6.3.1 Description of the Closest Point Projection Iteration for Drucker-Prager Model	114
6.3.2 Integration of a Iteration in the Load Cycle	116

6.3.3 Comments on the implementation of General Closest Point Projection Algorithm for Drucker-Prager	117
6.3.4 Comparison between Drucker-Prager Predictions under Deviatoric Stress Conditions and Data on Silica Powder and PE Pellets	119
6.3.5 Conclusions Concerning the Predictive Capabilities of Drucker-Prager Model	124
6.4 Closest Point Projection Algorithm and Convex Cutting Plane Algorithm Applied to Isotropic Hardening Models.....	125
6.4.1 Theoretical Predictions using Lade Model for Silica Powder subjected to Hydrostatic Compression	132
6.4.2 Numerical Simulation Results of Hydrostatic Test on PE Pellets.....	138
6.4.3 Conclusions for Hydrostatic Test on Silica Powder and PE Pellets	138
6.5 Convex Cutting Plane Algorithm applied to Deviatoric Hardening Lade Model	139
6.5.1 Numerical Simulation Results of Deviatoric Tests on Silica Powder	141
6.5.2 Numerical Simulation Results of Deviatoric Tests on PE Pellets under Deviatoric Test Conditions	147
6.5.3 Conclusions for Deviatoric Tests on Silica Powder and PE Pellets	152
6.6 Conclusions	153
5 CONCLUSION	154
APPENDIX	
A TRIAXIAL EXPERIMENTAL DATA.....	159
B ELASTIC PARAMETERS	169
C DETERMINATION OF PLASTIC STRAINS	171
D NUMERICAL SIMULATION DETAILS	179
E PARAMETRIC STUDY OF THE HYDROSTATIC HARDENING LAW	182
LIST OF REFERENCES.....	186
BIOGRAPHICAL SKETCH	196

LIST OF TABLES

<u>table</u>	<u>page</u>
2.1 Classification of particulate solids depending on size.....	6
2.2 Disadvantages and advantages of Cam-clay, Cap and Lade models.....	23
4.1 Strength of the material and dilatancy threshold as a function of the confining pressure obtained in monotonic tests.....	56
4.2 Elastic constants as determined from data obtained in a cyclic triaxial compression test under a confining pressure of 27 kPa.....	60
4.3 Elastic constants as obtained in a cyclic test at 70 kPa of confining pressure.....	61
4.4 Parameters of Lade model (1977) for silica powder	85
5.1 Strength of the material and dilatancy threshold as a function of the confining pressure obtained in monotonic tests.....	93
5.2 Elastic constants as obtained in a cyclic triaxial compression test under a confining pressure of 35 kPa.	97
5.3 Parameters of Lade model (1977) for PE pellets	107
6.1 Differences and common steps in the CPP and CCP algorithms	127
6.2 Material and hardening constants for Lade's parameters of silica powder used in the hydrostatic numerical simulations	133
6.3 Plastic and hardening constants for Silica powder and PE pellets to implement Lade model in the deviatoric numerical simulations.....	141

LIST OF FIGURES

<u>Figure</u>	<u>page</u>
2.1. Powder Classification chart based on size and particle density	7
2.2. Cam-clay yield surface	15
2.3. Elliptic cap model.....	17
2.4. Conical yield surface and spherical yield cap in triaxial plane	20
3.1. Mohr- circles and yield locus	26
3.2. Schematic diagrams of the yield loci of different bulk solids.....	27
3.3. Jenike shear cell.....	28
3.4. Jenike's shear apparatus for determination of flow properties of granular material.....	29
3.5. Yield loci and shear stresses	30
3.6. Shape of shear zone in a Jenike tester	30
3.7. Schultze shear cell	32
3.8. Peschl shear cell.....	32
3.5. Uniaxial Compression test	33
3.6. Measurements of the unconfined yield strength.....	34
3.7. Gerritsen tester	35
3.8. The Postec uniaxial tester	36
3.8.a. Schematic view of the Bates tester	37
3.9. The Johanson Indicizer	37
3.10. Biaxial test.....	39

3.10 a, 3.10.b: Types of biaxial tests	40
3.11. Triaxial compression.....	41
4.1. Experimental set up	46
4.2. Instron machine (model 5566) and the triaxial compression cell.....	47
4.3. Silica powder micro-graph.....	48
4.4. Deviatoric stress vs. axial strain at 93 kPa of confining pressure	50
4.5. Deviatoric stress vs. volumetric strain at 93 kPa of confining pressure	51
4.6. Volumetric strain profiles at confining pressures of 93 kPa, 40 kPa, and 70 kPa	52
4.7. Triaxial compression cell with deformed specimen.....	53
4.8. Specimen after a deviatoric test	54
4.9. Layers of particles dilating as they are sheared.....	55
4.10. Specimen after a hydrostatic test.....	55
4.11. Deviatoric stress vs. axial strain at 27 kPa confining pressure	57
4.12. Deviatoric stress vs. volumetric strain at 27 kPa confining pressure	58
4.13. Change in creep direction at the transition from compressibility to dilatancy (lateral confining pressure of 27 kPa)	59
4.14. Experimental variation of E (average values) with confining pressure compared to Duncan and Chang power law	62
4.15. Experimental variation of E (average values) with confining pressure compared to exponential variation of E (equation 4.3)	63
4.16. Experimental variation of K (average values) with confining pressure compared to exponential variation of K (equation 4.5)	64
4.17: Mohr-Coulomb yield Surface.....	65
4.18. Drucker-Prager yield Surface.....	67
4.19. Pressure vs. volumetric strain curve obtained in hydrostatic test	70

4.20. Collapse stress work/atmospheric pressure vs. f_c/p_a^2 , using power law variation for K in the computation of the elastic behavior. Fitted curve results: $d=0.913$, $U=0.0122$	71
4.21. Collapse stress work/atmospheric pressure vs. f_c/p_a^2 , using exponential law variation for K in the computation of the elastic behavior. Fitted curve results: $d=0.913$, $U=0.0122$	72
4.22. Collapse stress work/atmospheric pressure vs. f_c/p_a^2 , using exponential law variation for K in the computation of the elastic behavior. Fitted curve results: $d=1$, $U=0.0122$	74
4.23. Collapse stress work/atmospheric pressure vs. f_c/p_a^2 , using exponential law variation for K in the computation of the elastic behavior. Fitted curve results: $d=1$, $U=0.0121$	75
4.24. Experimental $\log \left[\left(\frac{I_1^3}{I_3} \right) - 27 \right]$ vs. $\log I_1 / p_a$ at failure	77
4.25. Variation of η_2 with f_p and σ_3	80
4.26. Variation of the intercepts with σ_3	81
4.27. Variation of W_{peak} with confining pressure	83
4.28. Variation of z with confining pressure	84
4.29: (a) Silica yield surfaces in a triaxial plane; (b) representation of the silica conical yield surface in the octahedral plane	86
5.1: Triaxial test on PE pellets in progress	89
5.2: PE specimen in triaxial test apparatus	89
5.3. Deviatoric stress vs. axial strain at 14.7 kPa of confining pressure	90
5.4. Deviatoric stress vs. volumetric strain at 14.7 kPa of confining pressure	91
5.5. Axial strain profiles at confining pressures of 14.7 kPa, and 35 kPa	92
5.6. Deviatoric stress vs. axial strain at 35 kPa confining pressure	94
5.7. Deviatoric stress vs. volumetric strain at 35 kPa confining pressure	95

5.8. Change in creep direction (arrow directions) at the transition from compressibility to dilatancy (lateral confining pressure of 35 kPa	96
5.9. Comparison of Young's modulus E , between the theoretical predictions (using equation 5.4) and data (circles)	98
5.10. Mohr-Coulomb yield surface for PE pellets	99
5.11. Drucker-Prager yield surface for PE pellets.....	100
5.12. Pressure vs. volumetric strain curve obtained in hydrostatic test	101
5.13. Experimental $\log \left[\left(\frac{I_1^3}{I_3} \right) - 27 \right]$ vs. $\log I_1 / p_a$ at failure	102
5.14. Variation of η_2 with f_p and σ_3	103
5.15. Variation of W_{peak} with confining pressure.....	105
5.16. Variation of z with confining pressure.....	106
5.17. PE pellets yield surfaces in a triaxial plane.....	108
6.1. Comparison between Drucker-Prager simulation and experimental deviatoric stress versus axial strain at 70.6 kPa and 93.6 kPa confining pressures for silica powder. Elastic moduli values are $E=46\,836$ kPa at 70.6 kPa confining pressure and $E=111\,443$ kPa at 93.6 kPa confining pressure	120
6.2. Comparison between Drucker-Prager predictions and experimental stress vs volumetric strain at 70.6 kPa and 93.6 kPa confining pressures for silica powder. The simulations correspond to constant values of the bulk modulus: $K=46\,836$ kPa at 70.6 kPa confining pressure and $K=111\,443.43$ kPa at 93.6 kPa of confining pressure	121
6.3. Comparison between Drucker-Prager predictions and experimental deviatoric stress vs. axial strain at 35 kPa of confining pressure for PE pellets. In the numerical simulations the elastic moduli were taken constant: $E=27555$ kPa	122
6.4. Comparison between Drucker-Prager model predictions and experimental deviatoric stress vs. volumetric strain at 35 kPa of confining pressure for PE pellets. In the numerical simulations: $E=27555$ kPa.....	123
6.5. Comparison between Drucker-Prager simulation and experimental deviatoric stress vs. axial strain; for PE pellets. Effect on the confining pressure. Constant elastic moduli: $E=27555$ kPa.....	124

6.6. Comparison between simulated and experimental hydrostatic data. Simulation results were obtained using the <i>CPP</i> algorithm and power law variation for elastic parameters (Lade 1977) ($K_{ur}=796.91$, $n_{ur}=0.78080$, $U=0.0122$, $d=0.913$)	134
6.7. Comparison between simulation and experimental hydrostatic data. Simulation results were obtained using the <i>Cutting Plane</i> algorithm and power law variation for elastic parameters (Lade 1977) ($K_{ur}=796.91$, $n_{ur}=0.78080$, $U=0.0122$, $d=0.913$)	135
6.8. Mean stress vs. volumetric strain. Simulated data were obtained using the Cutting plane algorithm, silica's fit for elastic and hardening constants and exponential law variation for elastic parameters ($K_{\infty} = 2.5 \cdot 10^5$, $\psi = -1.399 \cdot 10^5$, $\beta = 1.21 \cdot 10^{-3}$, $U=0.0122$, $d=0.913$)	136
6.9. Mean stress vs. volumetric strain. Cutting plane algorithm. Silica's fit for elastic and hardening constants ($K_{\infty} = 2.5 \cdot 10^5$, $\psi = -1.399 \cdot 10^5$, $\beta = 1.21 \cdot 10^{-3}$, $U=0.0122$, $d=0.913$ and 1). Effects of hardening constant (d) on silica powder simulation.....	137
6.10. Mean stress vs. volumetric strain. Hydrostatic experiment on PE pellets. The simulation data were obtained using the CCP algorithm and constant elastic moduli.....	139
6.11. Simulated and experimental deviatoric stress vs. axial strain at 70.6 kPa for silica powder. Variable elastic parameters, $K = K_{\infty} + \psi \cdot e^{-\beta \frac{I_1}{p_a}}$, $K_{\infty} = 2.5 \cdot 10^5$, $\psi = -1.399 \cdot 10^5$ and $\beta = 1.21 \cdot 10^{-3}$	142
6.12. Simulated and experimental deviatoric stress vs. volumetric strain at 70.6 kPa for silica powder. Variable elastic parameter, $K = K_{\infty} + \psi \cdot e^{-\beta \frac{I_1}{p_a}}$, $K_{\infty} = 2.5 \cdot 10^5$, $\psi = -1.399 \cdot 10^5$ and $\beta = 1.21 \cdot 10^{-3}$	143
6.13. Simulated and experimental deviatoric stress vs. axial strain. Comparison on simulation results at 70.6 and 93.6 kPa of confining pressures for silica powder, exponential variation of the elastic parameters with the mean stress was considered.....	144
6.14. Simulated and experimental deviatoric stress vs. volumetric strain at 70.6 and 93.6 kPa of confining pressures for silica powder; an exponential variation of the elastic parameters with mean stress was considered in the simulations.....	145

6.15. Simulated deviatoric stress vs. axial strain. Simulation results at 40, 70.6, 93.6, 150 and 200 kPa of confining pressure, using exponential variation for the elastic parameters	146
6.16. Deviatoric stress vs. volumetric strain. Simulation results at 40, 70.6, 93.6, 150 and 200 kPa of confining pressure, using exponential variation for the elastic parameters	147
6.17. Simulated and experimental deviatoric stress vs. axial strain at 14.7 kPa of confining pressure. Simulation data obtained using the CCP algorithm and constant elastic moduli, $K=1.7 \cdot 10^4$ kPa.....	148
6.18. Simulated and experimental deviatoric stress vs. volumetric strain for PE pellets at 14.7 kPa of confining pressure. Simulation data obtained using the CCP algorithm and constant elastic moduli, $K=1.7 \cdot 10^4$ kPa	149
6.19. Simulated and experimental deviatoric stress vs. axial strain at 14.7 and 35 kPa of confining pressure for PE pellets. Effect of the confining pressure. Simulation data obtained using the CCP algorithm and constant elastic moduli, $K=1.7 \cdot 10^4$ kPa.....	150
6.20. Simulated and experimental deviatoric stress vs. volumetric strain at 14.7 and 35 kPa of confining pressure for PE pellets. Simulation data obtained using the CCP algorithm and constant elastic moduli, $K=1.7 \cdot 10^4$ kPa	151
6.21. Simulated deviatoric stress vs. axial strain for PE pellets at 14.7, 90, 150 and 200 kPa of confining pressure. Simulation data obtained using the CCP algorithm and constant elastic moduli, $K=1.7 \cdot 10^4$ kPa	152

KEY TO SYMBOLS

[A]	consistent tangent moduli	$\left[\frac{\text{Force}}{\text{length}^2} \right]$
B	expansive plastic stress work constant	$\left[\frac{\text{Force}}{\text{length}^2} \right]^{-1}$
c	cohesion	$\left[\frac{\text{Force}}{\text{length}^2} \right]$
C	matrix of elastic moduli	$\left[\frac{\text{Force}}{\text{length}^2} \right]$
d	collapse exponent of plastic stress work	
D	plastic moduli	$\left[\frac{\text{Force}}{\text{length}^2} \right]$
$d\varepsilon$	total strain increment	$\left[\frac{\text{length}}{\text{length}} \right]$ or $\left[\frac{\text{length}^3}{\text{length}^3} \right]$
$d\varepsilon^{col}$	plastic collapse strain increment	$\left[\frac{\text{length}}{\text{length}} \right]$ or $\left[\frac{\text{length}^3}{\text{length}^3} \right]$
$d\varepsilon^{exp}$	plastic expansive strain increment	$\left[\frac{\text{length}}{\text{length}} \right]$ or $\left[\frac{\text{length}^3}{\text{length}^3} \right]$
$d\varepsilon^{el}$	elastic strain increment	$\left[\frac{\text{length}}{\text{length}} \right]$ or $\left[\frac{\text{length}^3}{\text{length}^3} \right]$
$d\varepsilon^{pl}$	plastic strain increment	$\left[\frac{\text{length}}{\text{length}} \right]$ or $\left[\frac{\text{length}^3}{\text{length}^3} \right]$

$d\lambda$proportionality constant in the flow rule for plastic strains

$d\lambda_c$ proportionality constant in the flow rule for collapse plastic strains $\left[\frac{Force}{length^2} \right]^{-1}$

$d\lambda_p$proportionality constant in the flow rule for expansive plastic strains $\left[\frac{Force}{length^2} \right]^{-2}$

E Young's modulus $\left[\frac{Force}{length^2} \right]$

E_∞ asymptotic value of Young modulus function $\left[\frac{Force}{length^2} \right]$

f_f cap model yield surface $\left[\frac{Force}{length^2} \right]$

f_c cap yield surface $\left[\frac{Force}{length^2} \right]^2$

f_p conical yield surface

f_{p60} 60% of the total value of f_p

F_u compaction force $[Force]$

F_f applied force at failure $[Force]$

g plastic potential function $\left[\frac{Force}{length^2} \right]$

g_c plastic potential function for collapse plastic strains $\left[\frac{Force}{length^2} \right]^2$

g_p plastic potential function for expansive plastic strains $\left[\frac{Force}{length^2} \right]^3$

G	shear modulus	$\left[\frac{\text{Force}}{\text{length}^2} \right]$
h	hardening moduli	$\left[\frac{\text{Force}}{\text{length}^2} \right]$
H	expansive plastic stress work constant	$\left[\frac{\text{Force}}{\text{length}^2} \cdot \text{length} \right]$
I_1	first invariant of the stress tensor	$\left[\frac{\text{Force}}{\text{length}^2} \right]$
I_2	second invariant of the stress tensor	$\left[\frac{\text{Force}}{\text{length}^2} \right]^2$
I_3	third invariant of the stress tensor	$\left[\frac{\text{Force}}{\text{length}^2} \right]^3$
J_2	second invariant of the stress deviator	$\left[\frac{\text{Force}}{\text{length}^2} \right]^2$
J_3	third invariant of the stress deviator	$\left[\frac{\text{Force}}{\text{length}^2} \right]^3$
k	number of iterations	
k_{max}	maximum number of iterations	
k_{vM}	von Mises material constant	$\left[\frac{\text{Force}}{\text{length}^2} \right]$
k_{DP}	Drucker-Prager material constant	$\left[\frac{\text{Force}}{\text{length}^2} \right]$
K	Bulk modulus	$\left[\frac{\text{Force}}{\text{length}^2} \right]$

K_{∞}	asymptotic value for Bulk modulus	$\left[\frac{Force}{length^2} \right]$
K_{ur}	Duncan and Chang Young modulus constant	$\left[\frac{Force}{length^2} \right]$
l_0	initial length of the sample	$[length]$
l	current length of the sample	$[length]$
L	exponent that models the variation of W_{peak}	
M	Cam clay material constant	
m	Lade model material constant	
n_{ur}	exponent of Duncan and Chang Young modulus expression	
n	strain step increment	
N	vertical force	$[Force]$
p_a	atmospheric pressure	$\left[\frac{Force}{length^2} \right]$
p_0	Cam clay model hardening parameter	$\left[\frac{Force}{length^2} \right]$
p	mean pressure ($I_1/3$),	$\left[\frac{Force}{length^2} \right]$
P	material constant that models the variation of W_{peak}	
r	slope of the straight line that models the variation of the intercept of η_2	
R^2	correlation regression	
R_{n+1}	flow rule residuals	
S	shearing force	$\left[\frac{Force}{length^2} \right]$

t	intercept of the straight line that models the variation of the intercept of η_2
T	average value of the straight line η_2 .
TOL_1	tolerance number with respect to the yield function
TOL_2	tolerance number with respect to the flow rule residuals
U	collapse modulus of collapse plastic stress work
V	current volume of the sample $[length^3]$
V_0	initial volume of the sample $[length^3]$
w_c	collapse strain hardening parameter $\left[\frac{Force}{length^2} \right]^2$
w	expansive strain hardening parameter
W_c	plastic stress work due to plastic collapse strain $\left[\frac{Force}{length^2} \right]$
W_p	plastic stress work due to expansive collapse strain $\left[\frac{Force}{length^2} \right]$
W_{peak}	maximum plastic stress work $\left[\frac{Force}{length^2} \right]$
W_{p60}	60% plastic stress work $\left[\frac{Force}{length^2} \right]$
\dot{W}	plastic stress work rate $\left[\frac{Force}{length^2} \cdot \frac{1}{time} \right]$
x	value of I_1 at the center of the elliptic cap
X	cap model hardening parameter $\left[\frac{Force}{length^2} \right]$
z	expansive plastic stress work constant

α_{DP}	Drucker-Prager material constant
β	material constant for bulk modulus
δ	Young's modulus law exponent
δ_{ij}	Kronecker delta
ϕ	angle of internal friction
μ	Lamé coefficient
λ	Lamé coefficient
ν	Poisson ratio
ν^p	plastic Poisson ratio
ρ_i	initial density $\left[\frac{\text{mass}}{\text{length}^3} \right]$
σ	normal stress $\left[\frac{\text{Force}}{\text{length}^2} \right]$
σ_{ij}	stress component of the stress tensor $\left[\frac{\text{Force}}{\text{length}^2} \right]$
$\dot{\sigma}_{ij}$	stress rate component $\left[\frac{\text{Force}}{\text{length}^2 \cdot \text{time}} \right]$
σ_1	major principal stress or axial stress $\left[\frac{\text{Force}}{\text{length}^2} \right]$
σ_2	intermedia principal stress or confining pressure or lateral stress $\left[\frac{\text{Force}}{\text{length}^2} \right]$
σ_3	minor principal stress or confining pressure or lateral stress $\left[\frac{\text{Force}}{\text{length}^2} \right]$

σ_s	normal stress at steady-state shear	$\left[\frac{\text{Force}}{\text{length}^2} \right]$
σ_p	normal stress at failure	$\left[\frac{\text{Force}}{\text{length}^2} \right]$
τ	shear stress	$\left[\frac{\text{Force}}{\text{length}^2} \right]$
τ_p	shear stress at failure	$\left[\frac{\text{Force}}{\text{length}^2} \right]$
τ_s	shear stress at steady-state shear	$\left[\frac{\text{Force}}{\text{length}^2} \right]$
σ_c	unconfined yield strength	$\left[\frac{\text{Force}}{\text{length}^2} \right]$
σ_u	consolidation stress in uniaxial testers	$\left[\frac{\text{Force}}{\text{length}^2} \right]$
σ_d	deviatoric stress, $(\sigma_1 - \sigma_3)$	$\left[\frac{\text{Force}}{\text{length}^2} \right]$
ψ	material constant for Bulk modulus	$\left[\frac{\text{Force}}{\text{length}^2} \right]$
ϵ_{VP}	plastic volumetric strain	$\left[\frac{\text{length}^3}{\text{length}^3} \right]$
ϵ_l	axial strain	$\left[\frac{\text{length}}{\text{length}} \right]$
ϵ_v	volumetric strain	$\left[\frac{\text{length}^3}{\text{length}^3} \right]$
ϵ_{ij}	components of the stress tensor	

η_1	Lade model material constant when reaches failure	$\left[\frac{Force}{length^2} \right]$
η_2	Lade model material constant for a given f_p and σ_3	
κ	intercept of straight line z	
γ	material constant for Young's modulus	$\left[\frac{Force}{length^2} \right]$
ξ	slope of the straight line z	
ω	ratio of the major and minor axis length of the elliptic cap	
Ω	cap model hardening constant	
Ψ_n	initial plastic work	$\left[\frac{Force}{length^2} \right]$
Ψ_{n+l}	final plastic work	$\left[\frac{Force}{length^2} \right]$
$\Delta\gamma$	plastic consistency parameter	
Π	cap model hardening constant	$\left[\frac{Force}{length^2} \right]^{-1}$

Abstract of Dissertation Presented to the Graduate School
of the University of Florida in Partial Fulfillment of the
Requirements for the Degree of Doctor of Philosophy

MECHANICAL BEHAVIOR OF PARTICULATE SYSTEMS:
EXPERIMENTS AND MODELING

By

Claudia V. Genovese

August 2003

Chair: Ray A. Bucklin

Cochair: Oana Cazacu

Major Department: Agricultural and Biological Engineering

Despite their technological importance, the understanding of the deformation mechanisms of particulate systems as well as the amount of information on material properties is still limited. Generally, the material properties are determined using shear testing, yet in order to predict the bulk material response during storage or transport, data corresponding to a variety of deformation, loading conditions, and shear rates are needed.

The main goal of this dissertation was to investigate the mechanical behavior of silica powder under general loading conditions and use or develop a model capable of predicting the observed behavior. Monotonic and cyclic confined compression tests were performed. The test results showed a strong non-linearity and stress-path dependency of the response. Elastic/plastic models were applied to silica. The simulation results show that a good agreement with data can be obtained only if hardening is taken into account. Modifications to existing theories were proposed resulting in an improved accuracy.

Another objective of this dissertation was to provide a protocol to be used in industry for characterization and modeling of the behavior of new systems. An industrial system, polyethylene pellets, was studied. It was shown that only one hydrostatic and two confined compression tests are sufficient to characterize the deformation and failure behavior of the material and determine the model parameters. Comparison of results showed close agreement between theory and experimental data, thus demonstrating that the approach taken is very useful in predicting the behavior of industrial systems for general loading conditions.

CHAPTER 1 INTRODUCTION

Almost every industry handles powders/bulk solids, either as raw materials or as final products. Examples include chemicals and chemical processing, foods, detergents, ceramics, minerals and pharmaceuticals. Powders are often stored in a container such as a bin, hopper or silo, and removed through an opening in the bottom of that container under the influence of gravity. The reliability of the process involved depends on the flowability of these powders. Free flowing powders do not often cause handling problems. However, most powders are cohesive, that is, they have the tendency to agglomerate or stick together over time. This tendency to agglomerate leads to the formation of arches or bridges within the powder mass and must be prevented for the material to flow out of a storage facility or a railcar. For a stable arch to form, the bulk solid must gain enough strength to support itself within the constraints of the container. The strength is a function of the degree of compaction of the material. Therefore, an important issue that needs to be addressed is characterization of the compaction behavior of powder systems under loading conditions as close as possible to the ones encountered in the field.

To fully understand the material behavior of bulk solids, experiments that induce general 3-D stress or strains in the material specimen are required. However, this is an impossible task and simplified tests are used instead. In these tests, only some of the stress or strain components vary independently. In powder mechanics and technology

measurements under shear conditions are generally used to characterize the bulk behavior. Among the shear testers, Jenike's shear cell is the most commonly used. Using such a device it is impossible to monitor continuously the evolution of deformation under the applied stress. The design of the tester is based on the assumption that the bulk solid displays rigid-hardening/softening plastic behavior. Moreover, the determination of the yield loci is based on the assumption that the material has reached steady-state deformation. However, some powders deform without ever reaching steady state deformation (see van der Kraan 1996). To characterize transient state deformation, other types of testers need to be used. Such a tester is the triaxial apparatus (von Karman 1911). In such a tester, axisymmetric compression is achieved and continuous measurements of deformation up to failure can be taken. A large volume of literature exists documenting triaxial tests on soils, but there is little published information regarding triaxial test results on powders (Tripodi et al. 1994a). A triaxial test consists of two stages, (1) hydrostatic and (2) deviatoric. In the hydrostatic part of the test, the specimen is subjected to an all-around pressure, which is gradually increased up to a given level, say σ_3 . In the deviatoric part, once the desired confining pressure σ_3 has been reached, the lateral pressure is kept constant while an axial load is applied to the sample through a loading piston.

In order to perform the triaxial tests on powders conducted in this study, the testing procedure was modified to permit measurements of volume deformation at very low stresses and under dry conditions. Reliable and complete data on the deformation, failure and flow behavior allow a fundamental understanding of powder compaction, flow initiation, and powder flow. Based on data from such tests, continuum models with

improved predictive capabilities can be used to determine the material behavior for loading conditions, which are not accessible through testing.

The main goals of this research were to study the mechanical behavior of silica powder under general loading conditions, to use/or develop a model capable of predicting the observed behavior and to examine whether the approach adopted for silica could be applicable to an industrial system. The specific objectives were as follows:

1. to characterize the mechanical behavior of silica using a triaxial tester,
2. to examine whether an elastic/perfect plastic approach can be adopted to model the observed behavior,
3. if the effect of accumulated plastic deformation on the behavior can not be neglected, use or develop a general stress-strain theory that predicts with accuracy the main features of the observed behavior,
4. to provide identification procedures for model parameters and perform parametric studies in order to evaluate the sensitivity of the response to change in parameters values,
5. to develop routines in order to numerically simulate the behavior and compare the theoretical predictions with data,
6. to analyze the efficiency and robustness of the numerical algorithms and provide recommendations concerning which algorithm to be used for a given model,
7. to examine whether the material characterization and data analysis used for silica could be applied to industrial systems such as polyethylene (PE) pellets.

CHAPTER 2 BACKGROUND

2.1 Introduction

Design of storage structures and handling facilities for bulk solids is not a new engineering problem. However, development of improved bulk solids storage and handling equipment continues to be severely impeded by limited knowledge concerning the behavior and characteristics of bulk solids under externally applied loads. One major obstacle to advances in this subject has been the lack of relevant experimental data for the materials and loading situations encountered in the field. One of the objectives of this dissertation was to generate compression data in the low-range pressures and load strain rate regime for an “academic” system, monosized silica, and an industrial system, polymeric pellets. To set the background and motivation for the experimental investigation conducted, a literature review of the subject is presented first.

The outline of this chapter is as follows: First, the concept of bulk solids is introduced, as well as the following methods of classifying bulk solids:

- powder or granular materials depending on particle size,
- cohesive or free-flowing materials depending on particle sizes and system's initial density,
- fluid-like or solid-like depending on the dynamical state.

Afterwards, a review of testing procedures used to assess the mechanical properties of bulk solids is given. Finally, a survey of continuum models of the behavior of powders under compression is presented.

2.2 Literature Review

A bulk solid is an assembly of particulate solid components dispersed in an interstitial fluid such that the individual particles are substantially in contact with near neighbors. If the interstitial fluid is a gas, a gas-solid interface occurs and the particulate solids are said to be dry. When the interstitial fluid is a liquid, a liquid-solid interface occurs and the particulate solid is said to be saturated or partially saturated depending on the amount of liquid (Chou et al. 2001). However, this definition is very general and depending upon the size of the constituents, bulk solids may be classified in the following categories:

A **powder** is defined as a particulate solid system containing particles of about 100 μm and smaller. If the majority of the particles are larger in size, the particulate solid is called a **granular material**. A classification of particulate solids based on particle size given by Richards and Brown (1970) and Nedderman (1992) is shown in table 2.1.

Geldhart (1973) proposed a classification of the particulate solids based on their fluidization behavior. Depending on particle size and density, he designated 4 types of powders: A, B, C and D. Type A powders are of low cohesion and are intermediate between categories B and C. These materials are readily fluidized. Type B particles fluidize readily and bed expansion is small, with rapid collapse when gas ceases (this group includes sand-like materials). Type C materials consist of small particles and surface forces play an important role in their mechanical behavior. These materials

cannot usually be fluidized in the conventional sense. They typically form channels, or cause impediments to flow (see Figure 2.1).

One of the main difficulties in mathematically describing the mechanical behavior of a particle assembly, whether cohesive or cohesionless, is that its state, i.e. solid or liquid, is not well defined. Jaeger and Nagel (1992) suggest that a powder cannot be classified as either a solid or a liquid due to the unusual behavior associated with powders. That is, powder materials can display a complex range of dynamic behavior that in some ways can be parallel to all of the behaviors of solids, liquids, and gases.

Table 2.1: Classification of particulate solids depending on size

Classification	Particle size range (micro)
Ultra-fine	<1
Superfine	1-10
Granular powder	10-100
Granular solid	100-3000
Broken solid	>3000

Source: Richards and Brown 1970 and Nedderman 1992.

Nevertheless, depending on the strain rate, a powder may exhibit two distinct types of behaviors: it can flow like a fluid at high strain rates or it can agglomerate to form clusters and behave like a solid for low strain rates (Rietma 1991; Jaeger et al 1996; Chou 1999). Since no universally accepted governing equations have been developed as has been done for fluid mechanics and solids mechanics, the characterization of powder materials has been the subject of much research including recent studies by Donsi and

Ferrari (1991), Rastogi et al. (1993), Mei et al. (2000), Tardos (1997) and Klausner et al. (2000).

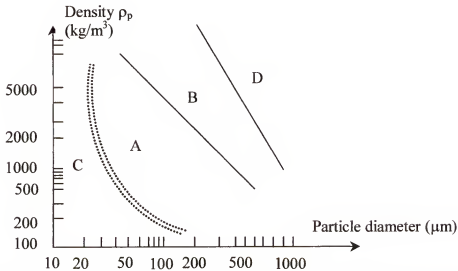


Figure 2.1: Powder classification chart depending on size and particle density (Geldhart 1973)

When powders flow in the high shear regime (strain rate of deformation higher than 1/s), individual powder particles are sufficiently energized so that the powder assembly behaves like a free flowing fluid. This regime has received significant attention (see Savage and Jeffery 1981; Jenkins and Savage 1983; Lun et al. 1984; Jenkins and Richman 1986). The basic modeling strategy in these studies was to derive equations based on microscopic models of individual particle interactions.

In a low shear regime (rates of deformation lower than 10^{-6} /s) inertia effects can be neglected and the powder is said to be in a quasi-static state. The main mechanism of deformation is related to stresses generated by normal forces in relatively continuous contacts between particles (Gutfraind and Pouliquen 1996). Quasi-static conditions appear in material storage in a bin or a hopper or in material handling, and in the case of

slow flow that occurs at discharge. The strength of the powder structure determines the magnitude of the forces that must be applied to initiate flow. The draw down of bulk materials from bins and hoppers may be interrupted by the formation of arches or domes. Above an arch or dome, the material is at rest (consolidated) and additional energy must be supplied, e.g., through vibration or air flow. Consequently, the arch or dome is broken and the discharge is resumed (Drescher 1991). This discontinuous flow behavior of the material, such as stick slip type behavior, is principally caused by forces transmitted by friction through the contact points of the particles in the bulk material. The consolidation and non-rapid flow of cohesive particle solids occur at pressures between 0.1 and 100 kPa and deformation rates lower than 1/s (Molerus 1978; Tomas 2000). Particularly, difficulties arise when attempts are made to predict the mechanical behavior of these bulk solids under externally applied loads. In order to design storage devices for bulk solids more efficiently, it is essential to measure accurately the behavior of powder systems under loading conditions similar to the conditions encountered in storage facilities.

In powder technology, the most widely used tester is the Jenike tester (1961, 1964) where the bulk solid is assumed to obey a Mohr-Coulomb theory. The main assumption of this theory is that under increased shear stress, bulk solid reaches steady state deformation. At steady-state, the yield locus is approximated by

$$\tau = c + \sigma \cdot \tan \phi \quad (2.1)$$

where τ is the magnitude of the shear stress on the failure plane, σ is the normal stress on the plane (compressive stresses are assumed to be positive), c is the cohesion, and ϕ is the angle of internal friction. The cohesion and the slope of the yield locus can be measured using the above mentioned shear tester during steady state deformation, which is the flow

with no change in stresses and bulk density. Although the Jenike tester is the standard measurement device for bin and hopper design purposes, it shows limitations. One of these limitations is that it is difficult to use for highly elastic bulk solids due to the limited allowed material displacement. More details about the strengths and weaknesses of the Jenike shear tester will be given in Chapter 3.

Carr and Walker (1967) sought to develop a material strength apparatus as an alternative to the Jenike shear cell. This device is an annular shear cell with unlimited displacement. This torsional shear cell is often used for materials that exhibit large deformations (above 10%) (Aloufi and Santamarina 1995). Schulze (1996) designed an alternative ring shear cell, where measurements could be achieved at consolidation stresses down to 500 Pa. However, problems with sample preparation were an undesired complication. This annular cell also produces a non-homogenous stress distribution. These disadvantages explain why this cell has not become standard equipment in powder technology.

In all the testers mentioned above, the state of stresses is not homogeneous and therefore unknown (van der Kraan 1996). van der Kraan (1996) and Bell et al. (1995) suggested that the actual shear planes in these shear testers deviate from the assumed shear planes (horizontal shear plane in Jenike shear cell). Since the hypothesis of horizontal shear plane is used in data reduction, stresses at incipient flow (initiation of flow, frictional forces are fully mobilized) calculated using these devices are underestimated and the extent to which this occurs is not quantifiable. Furthermore, Kamath and Puri (1997) indicated that these testers force the test sample to shear along a predetermined plane, which may not be the natural shear plane. Nevertheless, for powder

materials that deform in steady state, the Jenike shear tester is the most widely used for hopper design.

However, a bulk material can deform without ever reaching steady state deformation. Examples include tabletting and caking behavior (see Schwedes 1996). The deformation is transient and compaction is dominant. Therefore, in order to simulate processes in which uniaxial compaction is dominant, other types of testers are required. With uniaxial testers, the strength of a granular material known to cake could be measured (Adams 1993). Several uniaxial compression testers have been developed. Examples are the Gerritsen tester (Gerritsen 1986), the Postec uniaxial tester (Maltby 1993), the Johanson hang-up indicizer (Johanson 1992) and the Bates/Ajax uniaxial shear tester. With these systems, fairly homogeneous samples and stress distributions are obtained. Descriptions of the different testers as well as their respective advantages and disadvantages will be presented in Chapter 3.

In a real storage facility, the bulk material is in a three-dimensional state of stress that uniaxial testers cannot duplicate. Unlike the behavior of metals, the response of a powder is greatly influenced by the confining pressure. There is a large body of experimental data that show that the strength of powder materials is an increasing function of the confining pressure (Clower et al. 1973; Cristescu 1989; Hardin et al. 1990; Bock et al. 1991; Saada 1999; Genovese et al. 2002; Park and Kim 2001; Abdel-Hadi et al. 2002).

Consequently indirect shear testers where shear planes can develop freely and transient state deformation occurs are required. In order to properly characterize the stress-strain behavior, strain measurements have to be performed as well (Lade and

Duncan 1975; Nova and Wood 1979; Zhang et al. 1989; Tripodi et al. 1994a; Puri et al. 1995; Schwedes 1996). These requirements are only fulfilled by the triaxial tester (Bishop and Henkel 1962), which is described in detail in chapter 3. The triaxial tester was first designed by von Karman (1911) and was intended for studying the behavior of rocks under pressure. Triaxial tests have been also widely used for the study of soil behavior, agricultural grains, metal powders, composite powders, etc. (Terzaghi and Peck 1948; Lorenzen 1957; Stewart et al. 1968; Sridhar and Fleck 2000).

Because proper design of storage facilities is essential, there is a need to incorporate in the design methodology a constitutive model whose parameters are identified from calibration tests. The most important information needed from these calibration tests is the complete state of stresses and strains. A triaxial tester was used in this thesis to provide this information.

2.3 Constitutive Models

Most of the existing theories for designing storage facilities and determining bin-loads under quasi-static conditions originated in the field of soil mechanics. Theoretical studies began as early as the eighteenth century when Coulomb (1773) presented an analysis of earth pressure against retaining walls. Coulomb hypothesized that the soil fails along a plane of rupture and the wedge of earth formed between the plane of rupture and the wall exerts a force upon the wall due to its self-weight. Rankine (1857) developed a retaining wall theory by making a stress analysis of a homogeneous, cohesionless, and incompressible soil mass in which friction between the wall and soil was assumed to be negligible. The Equivalent Fluid Density Theory sometimes used in grain bin design assumes that the pressure caused by the granular material can be calculated by a hydrostatic formula with the use of an equivalent fluid density. The use

of this theory caused failure of many bin designs due to the vertical wall load, that is produced by the grain-wall friction. Roberts (1882) reported that the incremental weight of the grain material transmitted to the bin floor decreased with grain height and the remainder of the grain material was supported by the walls by means of grain-wall friction. Jansen (1895) developed a differential equation which took into account the effect of the grain-wall friction to predict grain bin pressures. However, he assumed that the wall friction coefficient, pressure ratio and bulk density are constant throughout a grain material. Ross (1960) presented a theoretical approach to the analysis of forces acting in a grain bin by analyzing the forces acting on individual particles. During subsequent years many theoretical and experimental studies concerning dynamic and static grain pressures distributions on bins were carried out (Jenike 1961; Savage and Yong 1970; Clower et al 1973; Thompson and Ross 1984; Drescher 1991; Schulze and Schewdes 1992; Blight and Gohnert 1993; among others). The underlying assumption of all these methods is that the bulk material can be considered as a rigid plastic solid obeying a Mohr-Coulomb yield condition, which assumes that the yield locus coincides with the failure surface. The Mohr-Coulomb yield condition involves only two principal stresses (σ_1 and σ_3 , major and minor stress respectively) and neglects the influence of the intermediate principal stress (σ_2) on shear strength.

2.3.1 The von Mises and Drucker-Prager Models

The von Mises criterion predicts that yield occurs when the value of the second invariant of the stress deviator tensor (J_2) is equal to a certain constant value. Mathematically, it is expressed as,

$$f(J_2) = \sqrt{J_2} - k_{vM} = 0 \quad (2.2)$$

where, $J_2 = \frac{1}{6}[(\sigma_1 - \sigma_2)^2 + (\sigma_2 - \sigma_3)^2 + (\sigma_3 - \sigma_1)^2]$, σ_i , $i = 1 \dots 3$ are the principal stresses and k_{vM} is the material constant defining the onset of yielding.

To include the effects of hydrostatic stress on the shearing resistance of the material such as soil, the von Mises yield criterion was modified by Drucker and Prager (1952) to include the first invariant of the stress tensor (I_1). Thus:

$$f = \sqrt{J_2} - \alpha_{DP} \cdot I_1 - k_{DP} = 0 \quad (2.3)$$

$I_1 = \sigma_1 + \sigma_2 + \sigma_3$; α_{DP} and k_{DP} are material constants, related to the frictional and cohesive strengths of the materials, respectively.

These models assume that the yield surface is fixed in stress space and a state of stress outside the surface is not stable. The material could undergo plastic deformation only if the stress point is on the failure surface. However, it has been observed that many granular materials experience plastic deformations from the very beginning of loading, that is, if the material is unloaded from a given state during loading, it does not return to its original configuration and experiences irreversible deformations. Thus, the behavior is defined by a series of yield surfaces prior to reaching the failure or the final yield surface. During the successive yielding, the material hardens and exhibits strain or work hardening behavior. The yield surfaces that define this hardening behavior are often called *hardening caps*. Drucker et al. (1957) were the first to suggest that soil might be modeled as an elasto-plastic strain hardening material. They introduced a spherical end-cap to the Drucker-Prager model in order to control the plastic volumetric change of soil (dilatancy). In the development of their model, there are two important innovations:

- the introduction of the idea of spherical cap.

- use of the current soil density (specific volume or void ratio) as the strain-hardening parameter.

This strain-or work-hardening model was a major step toward a more realistic representation of soil behavior. Three specific isotropic hardening cap laws are reviewed in the following paragraphs.

2.3.2 Cam-clay Model

The experimental evidence indicates that for particulate materials a clear distinction exists between the stress condition at which the irreversible behavior initiates and those stress conditions corresponding to failure. The Cambridge group under the leadership of Roscoe (Roscoe et al. 1963; Schofield and Wroth 1968) extended the basic concept of Drucker et al. (1957) and developed several plasticity-based models based on experimental data from triaxial tests on clay. These models are based on the observation of steady-state flow and the concept of critical state line. When a sample is subjected to a triaxial compression test, further loading produces an elastic-plastic response and subsequent yield surfaces have the same shape (isotropic hardening). Eventually, the load path arrives at the critical state line, where the associated flow rule demands that deformations may continue only in a constant volume manner. Thus, failure is implied. Volumetric strain is assumed to be partially recoverable but shearing strain is totally recoverable.

The original Cam-clay model assumes the cap is bullet shaped. The model predicts larger shear deformations than those observed for small shear stress levels. In order to overcome this limitation, a modified version of the Cam-clay model was suggested by Burland (1965) where the bullet-shaped surface of the Cam-clay model was replaced with an elliptical shape. Subsequently, an extension of this model to a three

dimensional stress state, known as modified Cam-clay, was proposed by Roscoe and Burland (1968).

The modified Cam-clay model is an isotropic, nonlinear elastic hardening plastic model. In this model, only volumetric strain is assumed to be partially recoverable, that is, elastic distortional strain (shearing strain) is assumed to be identically zero. Elastic volumetric strain is nonlinearly dependent on hydrostatic pressure and independent of deviatoric stresses.

A Cam-clay yield surface and the projection of the critical state line in the $p - \sqrt{J_2}$ space are shown in Figure 2.2. The yield curve in the p (mean pressure) vs. $\sqrt{J_2}$ space has an elliptic shape and is expressed as

$$f = p^2 - p_0 p + \frac{J_2}{M^2} = 0 \quad (2.4)$$

where M is a material constant and p_0 is a strain hardening parameter representing the value of p at the intersection of the yield cap with the p -axis.

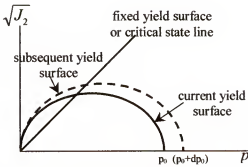


Figure 2.2: Cam-clay yield surface

On the other hand, the critical-state line, which controls the failure of material, intercepts the elliptic yield surface at its maximum point and is defined by an extended von Mises type expression:

$$\sqrt{J_2} = M \cdot p \quad (2.5)$$

Tripodi et al. (1994b) and Puri et al. (1995) used a modified Cam-clay model to simulate the compaction behavior of wheat flour. It became evident that the constitutive model was inadequate. Shinohara (1984) reported that for each confining pressure, there exists a stress value for which the slope of the octahedric shear stress versus volumetric strain curve changes sign, i.e., above which the volume expands. Therefore, the behavior of such powders is not described correctly for undrained conditions by the critical state class of models. It was necessary to develop a constitutive model of enough generality to properly account for the existence of the two regimes of volumetric behavior, i.e., compressible and dilatant regimes, respectively.

2.3.3 Cap Model

In recent years, the Roscoe surface has been further modified and refined by DiMaggio and Sandler (1971), Baladi and Rohani (1979), and Sandler and Rubin (1979) among others. This class of models is known as cap models

Initially developed for sands, various authors have applied cap models, not only for geotechnical engineering applications (Nelson and Baladi 1977; Baladi and Rohani 1979; Chen and McCarron 1983; Minuzo and Chen 1984; Daddazio et al. 1987) but also for ceramic materials with some success (Crawford and Lindskog 1983; Trasorras et al. 1989; Gethin et al. 1994; Aydin et al. 1996; Chtourou et al. 1995; Chtourou et al. 2002). The loading function for the cap model shown in Figure 2.3 is assumed to be isotropic and consists of the following two parts:

- a failure surface that describes the perfectly plastic material response:

$$f_f(I_1, J_2) = 0 \quad (2.6)$$

- an elliptic strain-hardening cap, which expands isotropically about the hydrostatic axis:

$$f_c(I_1, J_2, X) = 0 \quad (2.7)$$

The movement of the cap is controlled by the increase or decrease in the plastic volumetric strain through the hardening function X . Thus, dilation/compaction properties may be represented. In conclusion, three types of material responses may be represented: elastic, perfect plastic and strain hardening. Details concerning these three responses and the specific expressions of the functions f_f and f_c are given in the following.

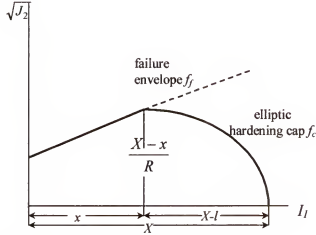


Figure 2.3: Elliptic cap model

The elastic behavior can be modeled as linear elastic or by using various types of non-linear elastic models (Lade and Duncan 1975; Lade 1977; Cazacu et al. 1997; Cristescu 1989; Genovese et al. 2002).

The yield/failure criteria (f_f) used with this model is the Drucker-Prager shear failure surface function (equation 2.3).

The strain-hardening elliptic cap is described by,

$$f_c = [I_1 - L(x)]^p + [\omega]^p \cdot J_2 - [X - L(x)]^p = 0 \quad (2.10)$$

where, x represents the value of I_1 at the center of the elliptic cap,

$L(x)=1$ for $x<0$ (in compression)

$L(x)=0$ for $x>0$ (in tension)

ω is the ratio of the major and minor axis lengths for the elliptic cap and X is the hardening function.

$$X = \frac{1}{\Pi} \cdot \ln \left(1 + \frac{\varepsilon_v^p}{\Omega} \right) \quad (2.11)$$

Π and Ω are hardening constants and ε_v^p is the plastic volumetric strain.

If the state of stress is within the envelope described by the functions $f_f = 0$ and $f_c = 0$, the material is assumed to be elastic, if not the material undergoes plastic deformation. Plastic flow is defined by a flow rule. The plastic strain increment is then assumed to be parallel to the stress gradient of a plastic potential function (g).

$$d\varepsilon_{ij}^p = d\lambda \frac{dg}{d\sigma_{ij}} \quad i, j = 1 \dots 3 \quad (2.12)$$

where $d\lambda$ is the proportionality constant.

As already mentioned, the cap surface hardens or softens as a function of the volumetric plastic strain. If yielding is governed by the cap (isotropic loading), there is only volumetric compaction and the material hardens, whereas, the yielding is governed by the shear failure surface there is volumetric dilation (which causes shear induced softening). This model is associated, that is, the plastic potential function g , is considered to be the same as the yield function.

However, test data show that the assumption concerning associated flow rule is not applicable for a wide range of confining pressures especially low pressures (Baladi

1988; Watson et al. 1997). Aydin et al. (1996), and Baladi and Rohani (1979) using this model for different materials (ceramic powders and saturated sands) explained this behavior by observing that α_{DP} and k_{DP} are not constant as stated in the model and should be replaced by the appropriate functions of stress or strain invariants.

All the models discussed so far neglect the effect of the third invariant on the behavior. However, all three principal stresses, i.e., σ_1 , σ_2 , σ_3 have important effects on the mechanical behavior of powders (Bardett 1990; Peric and Ayari 2000a; Alawaji et al. 1992; Lade 1977, 1984; Lade and Boonyachut 1982; Kim and Lade 1984; Saxena et al. 1988). A model that represents the failure condition more realistically is the Lade model (1977), which involves all the invariants of the stress tensor.

2.3.4 Lade Model (1977)

Lade model (1977) for cohesive soils belongs also to the class of cap models. The model consists of two yield surfaces (see Figure 2.4): (1) a curved conical yield surface and (2) a spherical cap. The spherical cap surface is controlled by the collapse of the soil skeleton (collapse strains) during isotropic compression. Failure is controlled entirely by the curved-conical yield surface, which describes shear (expansive) deformation.

Therefore, the total strain increments, $d\varepsilon$, are divided into an elastic component, $d\varepsilon^{el}$, a plastic collapse component, $d\varepsilon^{col}$, and a plastic expansive component, $d\varepsilon^{exp}$, such that:

$$d\varepsilon = d\varepsilon^{el} + d\varepsilon^{col} + d\varepsilon^{exp} \quad (2.13)$$

The cap type of yield surface is expressed in terms of the first and second invariants of the stress tensor, I_1 , and I_2 as follows:

$$\text{Cap type: } f_c = I_1^2 + 2I_2 \quad (2.14)$$

$I_2 = \sigma_1\sigma_2 + \sigma_2\sigma_3 + \sigma_3\sigma_1$ represents the second invariant of the stress tensor.

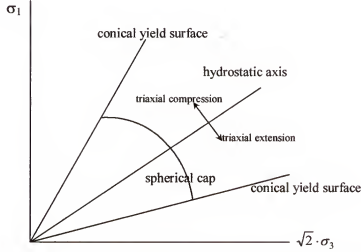


Figure 2.4: Conical yield surface and spherical yield cap in triaxial plane (Lade 1977).

The cap surface expands isotropically as the value of f_c increases. The associated flow rule is assumed.

On the other hand, in order to make the failure surface curved as observed for most soils, the frictional angle is assumed to decrease with increasing magnitude of the hydrostatic pressure. In this manner, the conical yield surface has been developed in terms of the first and third invariants of the stress tensor, I_1 and I_3 :

$$\text{Conical yield surface: } f_p = \left(\frac{I_1^3}{I_3} - 27 \right) \left(\frac{I_1}{p_a} \right)^m \quad (2.15)$$

$$\text{at failure } f_p = \eta_i \quad (2.16)$$

where η_i and m are material parameters, $I_3 = \sigma_1 \cdot \sigma_2 \cdot \sigma_3$ and p_a is the atmospheric pressure.

It is often assumed in plasticity theory that the plastic potential and the yield criterion are identical. As was mentioned earlier, this assumption is employed in this model for plastic collapse strains. However, it was found that this assumption is not accurate for the plastic expansive strain component (Poorooshasb et al. 1966; Lade and Duncan 1973, 1976). Assuming a plastic potential surface g_p , different from a yield surface avoids excessive dilation (Vermeer 1978; Oka and Adachi 1985; Zienkiewicz et al. 1985). In order to account for this, Lade (1977) incorporated another function in his model similar to the failure criterion as follows:

$$g_p = I_1^3 - \left(27 + \eta_2 \cdot \left(\frac{p_a}{I_1} \right)^m \right) \cdot I_3 \quad (2.17)$$

where, η_2 is a constant for given values of f_p and σ_3 .

The plastic expansive strains occurred on the curved conical yield surface are thus calculated from a non-associative flow rule assumption, whereas the plastic collapse strains occurred on the cap-type yield surface are calculated from the associated flow rule assumption.

In order to calculate the plastic collapse strains with the associated flow rule, a work hardening relationship is determined from the isotropic compression test. The total plastic work, W_c , accumulated due to the collapse strain is expressed in terms of f_c , that is:

$$W_c = F_c(f_c) \text{ (during isotropic compaction)} \quad (2.18)$$

The plastic work due to isotropic compaction can be calculated as:

$$W_c = \int \sigma_{ij} \cdot d\varepsilon_{ij}^{col} \quad (2.19)$$

In the same manner, to calculate the plastic expansive strains using a non-associated flow rule isotropic hardening relationships are determined from triaxial tests. The plastic work is expressed as a function of f_p , that is

$$W_p = F_p(f_p) \text{ (during shear conditions)} \quad (2.20)$$

At each stage of the triaxial compression tests the plastic work due to plastic expansive strains can be calculated as $W_p = \int \sigma_y \cdot d\varepsilon_y^{\text{exp}}$ (2.21)

From the work-hardening relationships of the cap yield surface and the conical yield surface, the corresponding plastic strains are obtained utilizing the flow rules.

For low strain rates, Zhang et al. (1986b) showed that the elastoplastic model developed by Lade (1977) for cohesionless sands adequately described stress-strain behavior for granular grains (wheat en masse).

2.3.5 Advantages and Shortcomings of the Existing Models

Perfect plastic models (von Mises, Drucker-Prager, etc.) cannot predict compaction/dilation prior to the failure of particulate materials. Hence, the cap type of hardening surfaces was introduced. The most important advantages and disadvantages of the Cam-clay, Cap and Lade models are summarized in Table 2.2.

Thus, in order to improve the current methods for designing bulk storage and handling facilities it is necessary to use a model, that is capable of describing in a more realistic and simple way the behavior of particulate systems under compaction. Zhang et al. (1986a, 1988) used the triaxial test to determine elastoplastic constitutive parameters for wheat in masse under monotonic and cyclic conditions. Using the triaxial test apparatus Zhang et al. (1986a), Li et al. (1990) and Zhang et al. (1989) determined the effect of the physical properties (initial bulk properties and moisture content) and axial

strain rate on the elastoplastic load response. Yet there is little published information regarding triaxial test results on powders (Tripodi et al. 1994b).

In this dissertation, Chapter 3 presents a review of testing devices used to characterize or determine the behavior of particle systems.

Table 2.2: Disadvantages and advantages of Cam-clay, Cap and Lade models

	<i>Cam-clay</i>	<i>Cap model</i>	<i>Lade</i>
<i>Disadvantages</i>	(1) failure is defined by a critical void ratio and not by a yield curve, (2) predicts zero dilatancy at failure, (3) assumes associated flow, hardening parameter depends on plastic volumetric strains.	(1) trial and error method to fit test data, (2) isotropic in form, circular trace in deviatoric plane, (3) relatively complicated, (4) assumes associated flow, (5) hardening parameter depends on plastic volumetric strains.	(1) not suitable for materials with significant anisotropic strength.
<i>Advantages</i>	(1) simple	(1) applicable to several materials, (2) control of plastic dilation	(1) simple, (2) curved meridian, (3) wider range of pressure than other criteria, (4) includes all invariants.

In Chapter 4 and 5, Mohr-Coulomb, Drucker-Prager and Lade models are calibrated using silica powder and Polyethylene pellets stress-strain experimental data. The practical application of such inelastic material models is done through the implementation of numerical methods to integrate the specific initial and boundary value problems. Chapters 6 and 7 present two different numerical algorithms called Closest Point Projection (Ortiz et al. 1983) and Convex Cutting Plane (Ortiz and Simo 1986) in order to simulate silica powder and Polyethylene pellets experimental data. The numerical results predicted by Drucker-Prager and Lade models are compared against the experimental results. In that manner, the capabilities of the models will be evaluated. The best model that describes the behavior of the systems will be determined.

CHAPTER 3 SHEAR CELL TESTERS

3.1 Introduction

Knowledge of the material properties of bulk solids is required for the design of bins and other bulk handling equipment in order to avoid flow problems such as arching in hoppers and segregation. Good flowability is generally defined as gravity flow of bulk solids that does not require any assistance. Any product that is classified as having poor flowability exhibits discharge problems or consolidation during storage or handling.

After storage, the intention is generally to make the powder flow or yield again. With cohesionless materials there is no difficulty and the shearing of the materials is easily performed because the flow of the material is caused by small stresses. With cohesive materials, the initiation of flow is more difficult. To fully determine the mechanical behavior of bulk solids, experiments where all possible stress or strain cases are induced on the material specimen are required. This is an extremely difficult task, thus, in practice simplified tests are utilized. In such tests, only some stress or strain state components are varied. In the following sections, different shear testers, procedures and the advantages and disadvantages of each tester are presented.

3.2 Direct Shear Testers

The most common method used to assess flow properties of bulk solids is shear testing. Generally, the bulk solid is assumed to obey a rigid-hardening/softening plastic behavior. The yield locus thus defines the stress conditions (shear stress and principal

stresses) for which flow occurs. The analysis of test results is done using the Mohr-circle diagram, which is a graphical representation of the stresses at any point in the granular mass (see Figure 3.1).

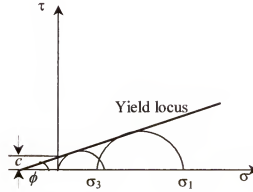


Figure 3.1: Mohr- circles and yield locus.

Usually, it is assumed that the material obeys a Mohr-Coulomb type yield locus, i.e., the envelope of the Mohr-circles is a straight line. If the major and minor principal stresses are denoted by σ_1 and σ_3 , c represents the cohesion of the material, ϕ the internal angle of friction, τ shear stress and σ normal stress acting on the failure plane, the Mohr-Coulomb yield locus is given by:

$$\tau = c + \sigma \cdot \tan \phi \quad (3.1)$$

For coarse, cohesionless particles the parameter c is taken zero, and the yield locus becomes:

$$\tau = \sigma \cdot \tan \phi \quad (3.2)$$

In reality, for most cohesive powders the envelope of the Mohr circles is a curve in the (σ, τ) plane (see Figure 3.2 b).

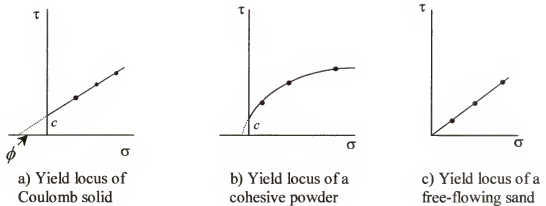


Figure 3.2: Schematic diagrams of the yield loci of different bulk solids.

3.2.1 The Jenike Shear Tester

Jenike (1961, 1964) was the first to apply the concepts of plasticity to hopper design. Based on the observation that powder flow in a hopper during discharge is generally very slow, he assumed that the flow is quasi-static. Specifically, he considered that during continuous discharge, small zones only a few particle diameters wide are in fact sliding along each other and rolling over each other, the bulk of the material being thus continuously deformed without changing its volume. The main hypothesis of Jenike's theory is that the bulk material experiences steady-state deformation and that it is appropriate to model this behavior with a rigid perfect plastic model. Jenike also designed a shear tester in which the relevant properties associated with steady state deformation could be measured. In the following, the test protocol and data reduction procedure are briefly presented.

3.2.2 Test Protocol and Data Reduction

The main part of the Jenike shear tester (Jenike 1961, 1964) is the shear cell (Figure 3.3). It consists of a base A, a ring B resting on top of the base and a lid C. The

base and ring are filled with a sample of bulk solid and pre-consolidated manually. A vertical force N , is applied to the lid. A horizontal shearing force S , is applied on a bracket attached to the lid. Division of N and S by the cross sectional area of the shear cell leads to the normal stress (σ) and the shear stress (τ). Measurement following manual pre-consolidation has to be carried out in two steps:

- the sample is first consolidated (*steady-state shear*)
- *shear to failure*.

To obtain *steady-state shear*, the bulk solid sample is subjected to a determined normal stress (σ_s) and subsequently sheared. Together, with the shear stress, the bulk density and the strength of the sample increase until a constant density and constant shear stress (τ_s) are reached. This condition is called "stationary flow", which is the flow with no change in stresses and bulk density.

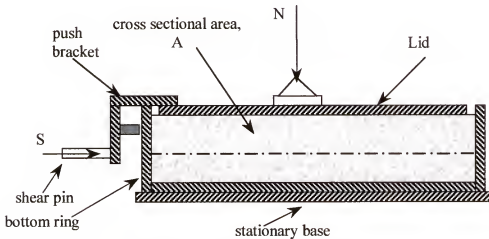


Figure 3.3: Jenike shear cell.

After the "stationary flow" shear preparation, the sample load is brought to zero.

The values of normal and shear stresses (σ_s , τ_s) at the stationary flow are established from

a $\sigma - \tau$ diagram. Next, the test sample is subjected to a smaller normal stress ($\sigma_p < \sigma_s$) and *sheared to failure*. At a specific shear stress level, the sample begins to yield, which corresponds to an expanding volume and lowering of the shear stress. The maximum value of the shear stress identifies the point where the yielding begins. The corresponding pair of σ and τ values (σ_p, τ_p) is a point of the flow boundary, called the *yield locus*.

Figure 3.4 shows the shear cell device; a controlled loading device and a recorder.

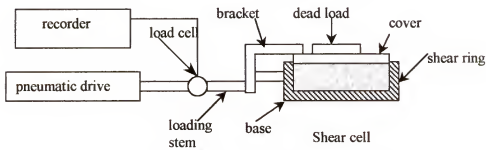


Figure 3.4: Jenike shear apparatus for determination of flow properties of granular material.

This process is repeated several times. Figure 3.5 illustrates how the points of steady state shear from a τ -time plot correspond to points on the yield locus in the τ - σ plot. The yield points correspond to flow. This yield locus, usually called the effective yield locus, is used to determine the rigid perfect plastic model parameters such as, cohesion and angle of internal friction.

Limitations of the Jenike shear tester are:

- It is mainly applicable to Coulomb type powders for which the yield locus can be approximated by a straight line (Makino and Kuramitsu 1986).

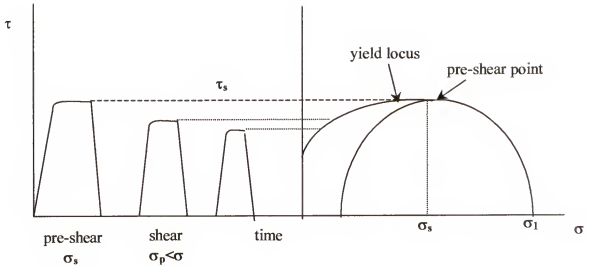


Figure 3.5: Plots of yield loci and shear stresses.

- For many systems, a shear plane cannot be identified and instead, a shear zone, which is lens shaped, forms (see Figure 3.6). Hence, the stress distribution is not uniform along the horizontal plane, and the shear stress calculated from the measured force is inaccurate. The area during shearing is not constant. This generates errors in the calculation of normal and shear stresses.



Figure 3.6: Shear zone shape in a Jenike shear tester.

- Strains occur in a narrow zone, restricted by the limited displacement allowed by the design of the tester.
- In order to identify the flow properties, the sample (bulk solid) has to reach steady state condition. Since the tester design limits the amount of displacement, the most appropriate use of the Jenike shear cell is for materials that do not require a large shear displacement to reach steady-state condition.
- The manual pre-consolidation technique depends on the skill of the operator, hence the test results are not operator independent.

Advantages of the Jenike shear tester are:

- Relatively, simple to use.

- Results are easy to interpret.
- Can be used with a wide variety of materials.
- Wall friction coefficients can be measured by reconfiguring the apparatus.

3.2.3 Other Testing Devices

In the Shultze shear cell (Carr and Walker 1967; Bagster et al. 1974), the measurement procedure is similar to that used for the Jenike shear cell. The bulk solid is first pre-sheared, and then sheared with the use of the annular ring. It has most of the same limitations as the Jenike shear cell with the exception that in the Shultze shear cell, the measurements of shear stresses are more influenced by wall effects than the measurements in a Jenike shear cell (Wilms and Schwedes 1985). The main advantage of this tester is that it allows infinite strain displacement (see Figure 3.7).

The rotational Split Level shear tester (Peschl 1989) rotates the powder over itself producing a torque, from which the shear stress is calculated (see Figure 3.8). The Peschl tester has similar advantages and disadvantages to Schultze's tester except that in the Peschl, the powder in the center of the tester is stationary.

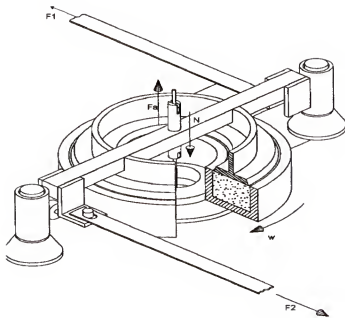


Figure 3.7: Schultze shear cell

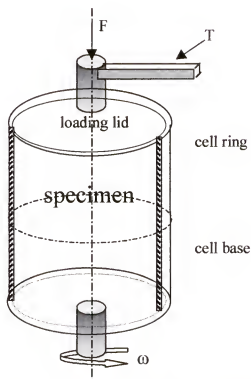


Figure 3.8: Schematic drawing of a Peschl shear cell (Peschl 1989).

3.3 Indirect Shear Testers

Indirect shear testers allow the powder to form its own shear planes during the progress of the measurement.

3.3.1 Uniaxial Compression

Such cases include tableting and caking behavior. For loading conditions such as those that occur in tableting or caking, the powder does not undergo steady-state deformation but transient deformation. Therefore, in order to simulate processes in which uniaxial compaction is dominant other equipment is required.

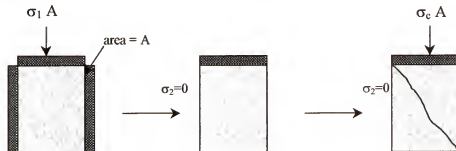


Figure 3.5: Uniaxial compression test.

Several uniaxial compression testers have been developed to determine the strength of a powder. Examples are the Gerritsen tester (Gerritsen 1986), the Postec uniaxial tester (Maltby 1993), the Johanson Hang-Up Indicizer (Johanson 1992) and the Bates/Ajax uniaxial direct shear tester. Generally, in uniaxial compression testers, the powder is subjected to uniaxial compaction, resulting in a powder compact, which is afterwards broken.

Figure 3.5 shows the protocol of uniaxial compression test. The powder is placed in a cylindrical container and covered with a lid. An axial stress $\sigma_1 = \sigma_u$ is applied at the top and the powder is consolidated (compressed axially by the piston moving from the

top downwards into the cylinder) to a desired level of stress, and then the stress is reduced by moving the lid upwards. After the cylinder is removed, the consolidated powder sample is left in an unconfined position that the specimen should be able to support itself due to consolidation.

An increasing stress is further applied at the top of the cylindrical specimen until the specimen fails. The stress value that causes the material failure is the unconfined yield strength.

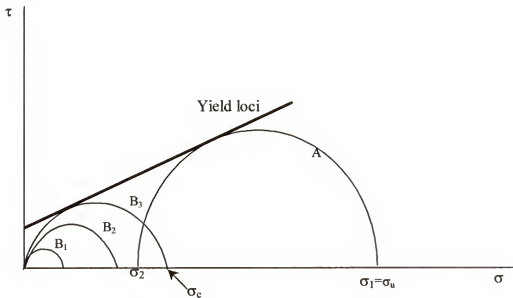


Figure 3.6: Measurements of the unconfined yield strength.

The results of this test can be represented on a shear τ , normal stress σ , plot as seen in Figure 3.6. The major principal stress (σ_1) is the vertical stress acting on top of the specimen, while the minor principal stress (σ_2) is the horizontal stress in the sample. Circle A represents the first stage of the test, where the sample is being compacted and both principal stresses are non-zero. The circles marked B_1 , B_2 , B_3 represent the last

stage of the test where the vertical stress is continuously increased and the horizontal stress is zero. In circle B₃ the horizontal stress (σ_2) is zero and the major principal stress is equal to σ_c , which corresponds to the failure of the specimen. This circle is tangential to the yield locus, which represents failure or flow of the bulk solid.

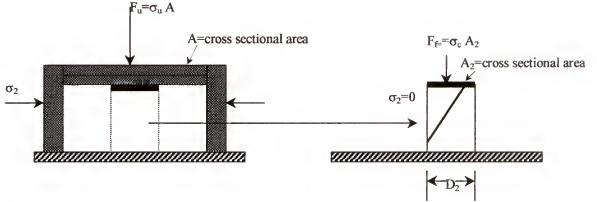


Figure 3.7: Gerritsen tester.

Figure 3.7 shows a schematic view of the Gerritsen tester. To avoid wall effects, the height to diameter ratio must be low (approximately 1). A force F_u is applied to compact the material and a cylindrical part of the sample is cut out using a knife. A force F_f is further applied to the top of the specimen and is continuously increased until the specimen fails. The unconfined yield strength is calculated using the formula:

$$\sigma_c = \frac{F_f}{\frac{\pi}{4} \cdot D_2^2} \quad (3.3)$$

where D_2 is the specimen diameter.

Cutting the sample from the compacted material reduces the strength of the material and produces a low value of σ_c . To improve the results, a polished stainless steel tube can be used to remove the sample.

Another commonly used tester, the Postec uniaxial tester, is shown in Figure 3.8. The height to diameter ratio of this tester is significantly larger than one.

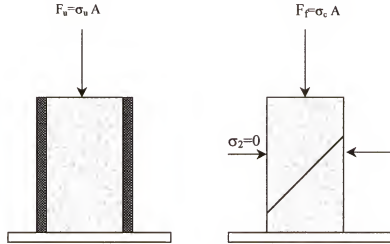


Figure 3.8: The Postec uniaxial tester.

Once more, the material is compacted and then sheared by applying an increasing axial force. A membrane and a wall surround the sample in the first stage and are removed in the second stage.

The test can be strain controlled by the use of a motor that gradually increases the displacement of the top lid. This tester produces more accurate results than any of the other uniaxial compression testers.

The Bates/Ajax uniaxial direct shear tester was described by Bell et al. (1995) and is schematically shown in Figure 3.8.a. As in the Gerritsen tester, the vertical stress is the major principal stress during axial compaction and therefore equation 3.3 applies.

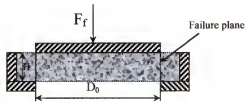


Figure 3.8.a: Schematic view of the Bates tester.

Bell et al. (1995) suggested that the force measured F_f is a measure of the unconfined yield strength σ_c :

$$\sigma_c = \frac{F_f + W_g}{\pi \cdot H \cdot D_0} \quad (3.4)$$

where W_g is the weight of the specimen and D_0 is the outlet diameter of the tester.

In the Johanson indicizer (Johanson 1992), a cylindrical test specimen of the bulk solid is compressed via a piston consisting of two concentric areas, as shown in Figure 3.9. The inner piston is intended to measure the consolidation pressure directly, which implies that the following formula applies:

$$\sigma_u = \frac{F_u}{\frac{\pi}{4} \cdot D^2} \quad (3.5)$$

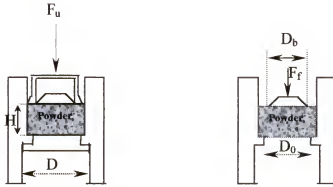


Figure 3.9: The Johanson indicizer.

After compression, the lower piston and the outer ring of the top lid is removed, then the powder is loaded with the inner piston until failure takes place. According to Johanson (1992) the unconfined yield strength, σ_c , can be directly measured and can be calculated using the formula:

$$\sigma_c \cong 2.2 \frac{F_f}{\pi \cdot H \cdot \left(\frac{D_b + D_0}{2} \right)} \quad (3.6)$$

During the measurement of the bulk solid's strength, the vertical stress decreases downwards toward zero and the specimen is subjected along its height to a variable stress. Consequently, the bulk solid's strength measured with Johanson indicizer is an average value. In addition to this, the only unconfined powder surface in the tester is located at the bottom of the sample. Therefore, this is a single area where indeed the sample is unconfined. Note that using the Johanson indicizer, which is intended to simulate uniaxial compaction, several quantitative indices that relate directly to powder handling and process equipment parameters can be determined. These indices are:

- The arching index (AI), which relates the unconfined yield strength of the material with the hopper outlet.
- The ratholing index (RI), which is utilized to calculate the critical rathole diameter and determine the size of the flow channel required to eliminate hang-ups on funnel flow.
- The flow rate index (FRI), which is used to determine powder flow rate from hoppers, the need for air injection, fluidization and flow rate limits.
- The hopper Index (HI), which is used to determine the conical half angle required to cause mass flow.
- The chute Index (CI), which is employed to determine slide angles to prevent build up on chutes.

In conclusion, the limitations of uniaxial compression testers are:

- The stresses at consolidation are not fully known due to wall friction effects.
- Stress distribution is not uniform.
- Measurements are influenced by the consolidation procedure.
- The strength value of the bulk solid is an average value.

- Practical experience is required for consistent results.

Advantages of uniaxial compression testers lie in the fact that they are easy to use and the test duration is relatively short. These testers are intended to simulate uniaxial compaction and predict quantitative indices that relate directly to powder handling and process equipment parameters. Such testers are generally used for equipment selection or quality control.

3.3.2 Biaxial Compression Tester

The design of a biaxial tester is such that there is no deformation in the z-direction hence an in plane strain is achieved. The sample is attached to two plates at the top and the bottom edges. The movement of these plates provides the stress σ_1 while σ_3 is applied (Figure 3.10). The increasing stress σ_1 causes the sample to deform and fail along a slip plane. In a biaxial tester, a cubical sample is bounded using four edges

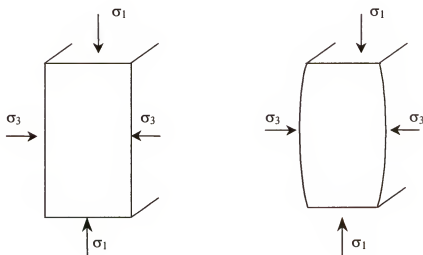


Figure 3.10: Biaxial test

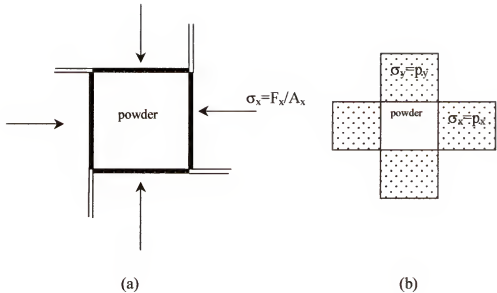


Figure 3.10.a, Figure 3.10.b: Types of biaxial tests.

These four boundaries are independently controlled, enabling strain controlled tests to be conducted. The walls of these testers are made of rigid plates that are surrounded by rubber membranes and lubricated to reduce the effects of shear stress (Figure 3.10.a). Biaxial tests can also be performed under stress control. This is achieved by constructing the edges of flexible walls of cubical balloons that are filled with pressurized air (Figure 3.10.b). If the edges of the walls are kept straight, it is possible to conduct strain controlled tests with flexible walls (Enstad and Maltby 1992).

Limitations of biaxial testers are:

- Stresses in the third direction cannot be controlled.
- More difficult to use than direct shear tester.

Advantages of biaxial tester are:

- Shear planes are spontaneously created as a result of applied stresses.

- Experimental results provide physical measurements suitable for use in constitutive models.
- Choice of strain control or stress control.

3.3.3 Triaxial Compression Tester

The triaxial tester is very common in the field of soil mechanics. It is used to test the strength of soils, but can be used to analyze other particulate solids. In a true triaxial test, as the name suggests, the three principal stresses are varied independently of each other allowing independent deformation in all three directions. However, in the commonly used triaxial test (von Karman 1911), the specimen is cylindrical which causes $\sigma_2 = \sigma_3$ as seen in Figure 3.11.

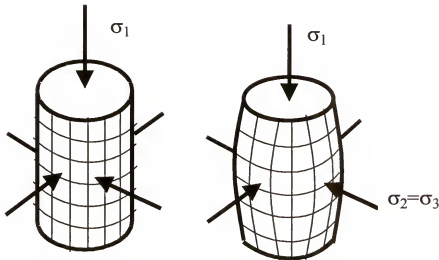


Figure 3.11: Triaxial compression.

This test is much easier and economical to conduct than a true triaxial test. The specimen is surrounded by a rubber membrane under an overall surrounding pressure is

applied by pressurizing the fluid around the specimen and/or by applying vacuum. This pressure is kept constant and an increasing axial stress is applied using an axial loading device. Nevertheless, different loading paths can be followed by changing confining pressures or by unloading/reloading steps. Likewise, varying axial loading rates can be used. Since the majority of the results in this study were obtained from triaxial testing, a more detailed description of the test is included in the description of the experimental set-up.

The main limitation, as for biaxial testers, is that the principal stresses cannot be varied independently.

Advantages of the triaxial tester are:

- The way of conducting experiments in a triaxial tester ensures that no shear strains or shear stresses can develop. All measured normal stresses and strains must therefore be principal stresses or principal strains. This means that the experimental results can be fully described in the principal stress or strain space.
- Provides data on the evolution of the deformation up to failure for a variety of loading paths. The experimental results are sufficient to generate 3-D constitutive models of material behavior.
- The experiments can be strain rate controlled or stress rate controlled.
- There is no limit to the specimen deformation.

The shear planes are spontaneously formed as a result of the applied stresses.

Triaxial compression tests are used in this study in order to measure the deformability and strength characteristics of particulate systems (silica powder and PE pellets).

CHAPTER 4 EXPERIMENTAL STUDY OF THE QUASI-STATIC DEFORMATION OF DRY SILICA POWDER

4.1 Introduction

The results presented in this section were obtained from an investigation of the factors controlling the compression behavior of dry silica powder under various loading conditions. The silica powder under study was monosized with a mean particle size of $63\mu\text{m}$. Although this system is fairly well characterized in terms of surface chemistry, information is still limited from a mechanical behavior point of view.

To simulate triaxial compaction, triaxial compression tests were performed. These tests allow the measurement of both the deformability and strength characteristics.

Measurements of the volume changes of the sample as a function of the applied stress were used to determine the evolution of the bulk density and yield behavior of the system studied. The measurements are presented as a series of stress-strain curves obtained at different confining pressures and a fixed strain rate. The organization of this chapter is as follows: First, triaxial compression test protocol is described, then analysis of the data obtained for silica powder and calibration of Mohr-Coulomb, Drucker-Prager and Lade models are presented.

4.2 Methodology and Experimental Set up

4.2.1 Background

In an ideal triaxial test, all three major principal stresses are independently controlled. However, independent control leads to mechanical difficulties that limit the conduction of such tests to special applications. The commonly used triaxial test refers to the axisymmetric compression test. This test has been used since the beginning of the last century to test the deformation and strength of soils. The soil sample is pre-compacted, saturated with water, and compressed both hydrostatically and deviatorically. The water discharged from the sample is used to measure the volume change and hence the density change. In recent years, the test has been used to test other bulk solids such as grains, powders, polymeric pellets, etc. In this work, the testing procedure was modified in order to test dry powders at low stresses. Knowledge of the behavior in this regime is essential for storage and handling applications.

4.2.2 Testing Procedure

A typical test was conducted as follows:

(I) Sample preparation:

- The cylindrical surface of the mold was covered by a latex membrane of 0.30 mm in thickness sealed by rubber O-rings to a pedestal at the bottom, and to a cap at the top.
- The material was poured into a cylindrical mold and then uniformly tapped.
- At this time, 91.4 mm of mercury of vacuum pressure was applied to the specimen to pre-consolidate it. The dimensions of the specimen after vacuum were 70 mm in diameter and 220 mm in height.
- The assemblage was then placed in the triaxial compression cell, which has a maximum capacity of 3400 kPa. The cell was filled with water, and then placed on the load cell of the Instron testing machine.

(II) Test steps:

Any test consisted of 2 stages: (1) hydrostatic and (2) deviatoric. In the hydrostatic part of the test, the specimen was subjected to an all-around pressure that was gradually increased up to a predetermined level, say σ_3 . Once the desired confining pressure σ_3 was reached, the lateral pressure was kept constant while an axial load was applied (deviatoric part) to the sample through the loading piston. A schematic drawing of the experimental set up is shown in Figure 4.1.

The quantities measured during the hydrostatic part of the test were:

- the applied pressure,
- the change in the volume of the sample which was determined by the change in the volume of water existing in the cell measured using a strength gage device (Abdel-Hadi et al. 2000).

The quantities measured during the deviatoric part of the test were:

- the axial force,
- the change in length of the sample and
- the change in the volume of the sample.

The accuracies in the Instron displacement measurements, load cell force measurements and volume change measurements are $\pm 0.001\text{mm}$, $\pm 0.001\text{N}$ and $\pm 0.0001\text{ cm}^3$ respectively. From the change in length of the sample, the magnitude of the axial

strain: $\epsilon_1 = \frac{l_0 - l}{l_0}$ was determined, where l_0 is the initial length of the sample and l is the

current length. The volumetric strain is defined as: $\epsilon_v = \frac{V_0 - V}{V_0}$, V_0 and V being the

initial and current volume, respectively. Here and throughout the text compressive stresses and strains are positive.

The tests were conducted in a thermostatically controlled air-conditioned laboratory with minimal ambient changes. The recorded temperatures and relative humidity were approximately 25°C and 45% respectively.

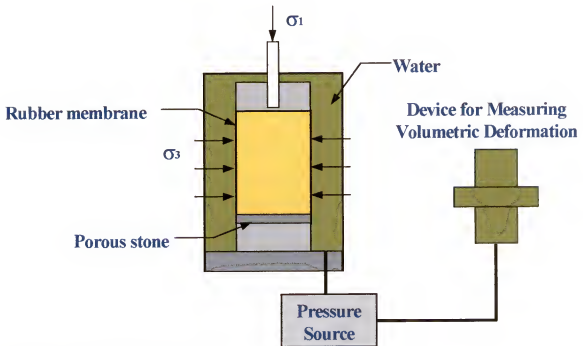


Figure 4.1: Experimental set up

To investigate the mechanical properties of a system under compression an experimental program was performed that included:

- hydrostatic tests up to 350 kPa.
- monotonic tests under lateral confining pressure σ_3 ranging from 27 kPa to 350 kPa.
- cyclic triaxial compression tests consisting of several loading-creep-unloading and reloading cycles under the same confining pressures.

A photograph of the Instron machine where the triaxial cell was placed to perform the tests is shown in Figure 4.2.



Figure 4.2: Instron Machine (model 5566) and the triaxial compression cell (model HW 10751).

4.2.3 System under Study

The first system tested was silica powder (silicon dioxide, floated powder). The geometrical configuration and surface structure of typical silica powder are shown in a SEM (scanning electron microscope) micro-graph (Figure 4.3). In general, the particles

were spherical in shape and monodisperse. The mean particle size was 63 μm . The particle density was about 2.3 g/cm^3 and the initial bulk density was about 1.3 g/cm^3 .



Figure 4.3: Silica powder micro-graph

4.3 Results of Monotonic Deviatoric Tests on Silica Powder

To identify and characterize the compaction properties of silica powder, a series of monotonic triaxial compression tests were performed at $\sigma_3 = 27$ kPa, 40.6 kPa, 70.6 kPa, 93.6 kPa and 350 kPa. Also, to better monitor and characterize the irreversibility of the material behavior cyclic tests were performed at the same confining pressures.

Because the cylindrical specimen in the triaxial cell is surrounded by a thin flexible membrane that is subjected to a uniform cell fluid pressure, the radial boundary of the specimen is free of shear stresses. Thus, the vertical and horizontal planes in the triaxial specimen are considered to be principal planes. In the hydrostatic part of the test

$\sigma_1 = \sigma_2 = \sigma_3 =$ cell pressure. During the deviatoric part of the test, $\sigma_2 = \sigma_3 =$ cell pressure, while the axial stress coincides with σ_1 .

As an example, the stress-strain curves (i.e. axial and volumetric strain vs. the stress difference $\sigma_1 - \sigma_3$) obtained under a confining pressure $\sigma_3 = 93$ kPa are shown in Figure 4.4. The initial density of the sample was $\rho_i = 1.33$ g/cm³. The stress versus axial strain curve presents 3 regions: (1) quasi-linear elastic, (2) concave towards the strain axis, (3) plateau. In the first part (up to 200 kPa), the behavior is considered to be elastic (the irreversible strains are small in comparison to the elastic, recoverable strains). Note that the Young's modulus, E , and the Bulk modulus, K , vary with the stress (see Table 4.1). In the second region, the plastic deformation undergone by the material is significant and the value of the yield limit continuously increases up to failure at $\sigma_d = \sigma_1 - \sigma_3 = 320$ kPa. The existence of a plateau shows that the material has viscous (viscoplastic) properties, that is, it deforms even under constant stress. The same type of behavior is observed in the tests at lower confining pressures ($\sigma_3 = 27$ kPa, 40 kPa, 76 kPa). A slip-stick phenomenon is observed (sudden reduction in material strength) at the beginning of the tests under low confining pressure.

The stress-volumetric strain curve, indicates that, under confinement, the material further compacts, then dilates (see Figure 4.5).

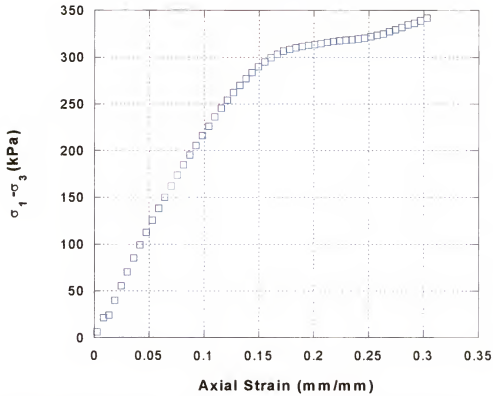


Figure 4.4: Deviatoric stress vs. axial strain at 93 kPa of confining pressure.

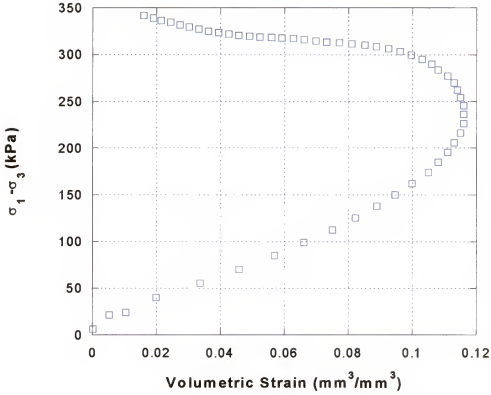


Figure 4.5: Deviatoric stress vs. volumetric strain at 93 kPa of confining pressure.

The existence of those two regimes of volumetric behavior was observed in all tests. Figure 4.6 shows the volumetric profiles obtained in all tests. It is clearly seen in Figure 4.6 that the stress value for which the curve $\sigma_1 - \sigma_3$ versus ε_v changes sign depends on the confining pressure.

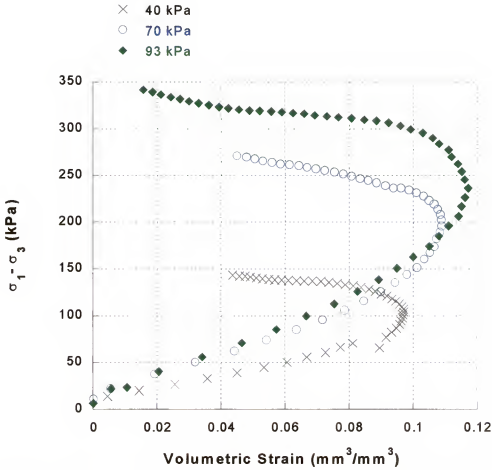


Figure 4.6: Volumetric strain profiles at confining pressures of 93 kPa, 40 kPa, and 70 kPa

These critical points define the boundary between the compressible and dilatant regimes. Note also, that the strength of the material is an increasing function of the applied confining pressure (see also Table 4.1). The stress-strain curves obtained from monotonic triaxial tests are shown in Appendix A. Figure 4.7 and Figure 4.8 show the deformed specimen at the end of the deviatoric test at 70 kPa of confining pressure.

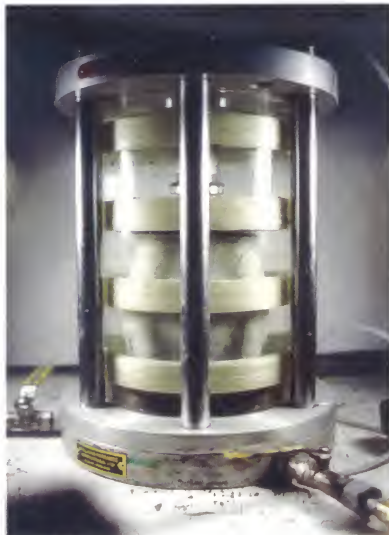


Figure 4.7: Triaxial compression cell with deformed specimen.



Figure 4.8: Specimen after a deviatoric test.

The bulging of the specimen, which can be observed in Figure 4.7 and Figure 4.8, is due to dilatancy (volume expansion) that occurs in the last part of the deviatoric test (see Figure 4.6). The powder expands because of the interlocking of the particles: deformation can proceed only if some particles are able to ride up or rotate over other particles. This phenomenon can be visualized with the aid of Figure 4.9, which shows two layers of particles, one on top of the other. If a shear stress is applied to the upper layer, then each particle has to rise (increasing the volume occupied by the material) for the sample to undergo any deformation.



Figure 4.9: Layers of particles dilating as they are sheared.

Figure 4.10 shows the specimen at the end of the hydrostatic test up to 350 kPa of confining pressure. The observed change in the shape of the specimen under hydrostatic conditions is primarily due to end effects (rigidity of the end caps and friction). However, the deformation in the middle section of the specimen could be considered to be homogeneous.

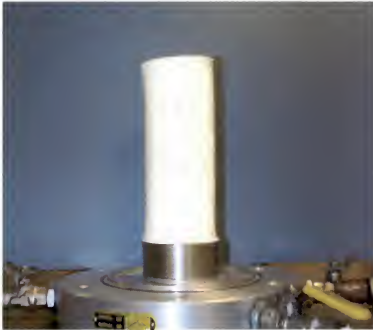


Figure 4.10: Specimen after hydrostatic test.

Table 4.1: Strength of the material and dilatancy threshold as a function of the confining pressure obtained in monotonic tests.

σ_3 , kPa (Confining pressure)	$\sigma_{failure}$, kPa (Compressive strength)	$\sigma_{dilatancy}$, kPa (Stress difference corresponding to the dilatancy threshold)
40	140	110
70	260	200
93	340	250

4.4 Results of Cyclic Deviatoric Tests

To better characterize the influence of the loading history on the material response, cyclic tests were performed under different confining pressures in the range 27 kPa-350 kPa. Figure 4.11 shows the results obtained from a test under 27 kPa confining pressure. The test consisted of five loading- unloading and reloading cycles. Before passing from loading to unloading, the load was held constant for 20 minutes in order to permit the sample to reach by creep a quasi-stable state. Then, unloading and further reloading were performed. From the slopes of σ_1 - σ_3 versus axial strain, the Young's modulus, E was determined.

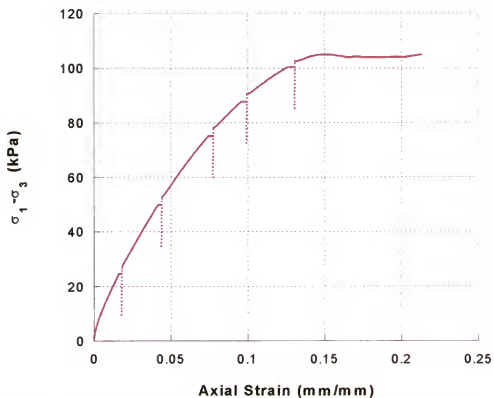


Figure 4.11: Deviatoric stress vs. axial strain at 27 kPa confining pressure

A dependence of Young's modulus E , on the mean stress ($I_1 = \sigma_1 + 2 \cdot \sigma_3$) was observed. The bulk modulus, K was evaluated from the unloading slopes of $\sigma_1 - \sigma_3$ vs. volumetric strain curve (Figure 4.12).

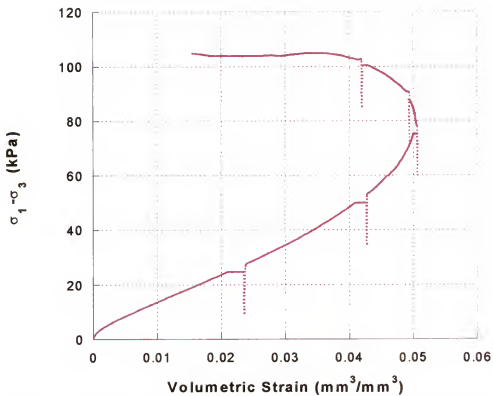


Figure 4.12: Deviatoric stress vs. volumetric strain at 27 kPa confining pressure

Note also a change in the creep direction at the transition from the compaction regime to the dilatancy regime. This effect can be clearly seen in the blow-up of the stress-volumetric strain curve shown in Figure 4.13.

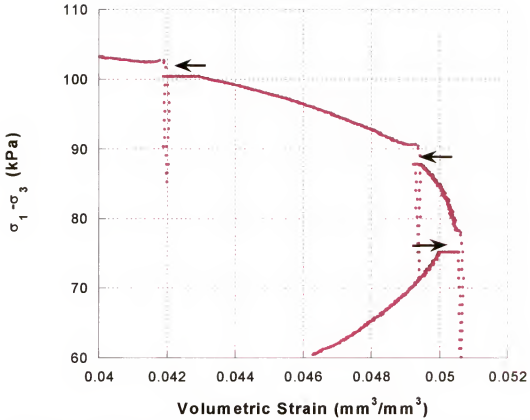


Figure 4.13: Change in creep direction (note arrow directions) at the transition from compressibility to dilatancy (lateral confining pressure of 27 kPa)

The values of the elastic moduli, determined from data obtained in the cyclic test at 27 kPa confining pressure, are given in Table 4.2. The same general trends were observed in all the cyclic tests. The stress-strain curves as well as the values of the elastic constants obtained in all the cyclic tests are presented in Appendix A.

Table 4.2: Elastic constants as determined from data obtained in a cyclic triaxial compression test under a confining pressure of 27 kPa.

Cycle Number	E (kPa)	K (kPa)
1	44420	35265
2	56988	59916
3	71676	121479
4	67380	73252
5	76004	130227

4.5 Modeling the Behavior in the Elastic Regime

In the elastic range, the behavior is approximated by Hooke's law:

$$d\sigma_{ij} = \lambda \cdot (tr\varepsilon) \cdot \delta_{ij} + 2 \cdot \mu \cdot \varepsilon_{ij}, \quad i, j = 1 \cdots 3 \quad (4.1)$$

where σ_{ij} represents the stress, ε_{ij} the strain, δ_{ij} Kronecker delta, μ and λ are the Lamé coefficients. The expressions of the Lamé coefficients in terms of E and K are:

$$\mu = G = \frac{3 \cdot K \cdot E}{9 \cdot K - E} \quad (4.2)$$

$$\lambda = K - \frac{2}{3} \cdot G = \frac{3 \cdot K \cdot (3 \cdot K - E)}{9 \cdot K - E} \quad (4.3)$$

A triaxial test can be used to estimate the Young's modulus E and the bulk modulus K directly from the slope of the unloading part of the deviatoric stress vs. axial strain curves and the deviatoric stress vs. volumetric strain curves *i.e*

$$E = \frac{d\sigma_1}{d\varepsilon_1}, \quad (4.4)$$

$$K = \frac{d\sigma_1}{3 \cdot d\varepsilon_v}, \quad (4.5)$$

where σ_1 is the axial stress, ε_1 is the axial strain and ε_v is the volumetric strain. The values of E and K obtained from the unloading slopes in a test at $\sigma_3 = 70$ kPa are given in Table 4.3.

Table 4.3: Elastic constants as obtained in a cyclic test at 70 kPa of confining pressure.

Cycle number	E (kPa)	K (kPa)
1	72528	46836
2	84673	65539
3	96064	82180
4	100422	52546
5	104629	155840
6	106597	265716

The average E values corresponding to each cyclic test are given in Table 4.3.

This observed variation of the Young's modulus with the confining pressure was approximated using the power law proposed by Duncan and Chang (1970):

$$E = K_{ur} \cdot p_a \cdot \left(\frac{\sigma_3}{p_a} \right)^{n_{ur}} \quad (4.6)$$

where p_a is the atmospheric pressure, A and n are dimensionless constants. For silica system, K_{ur} and n_{ur} were determined from fitting the experimental data with equation 4.6 being $K_{ur} = 796.91$ and $n_{ur} = 0.78080$. Figure 4.14 shows a comparison between the data (symbols) and the theoretical predictions obtained with equation (4.6)

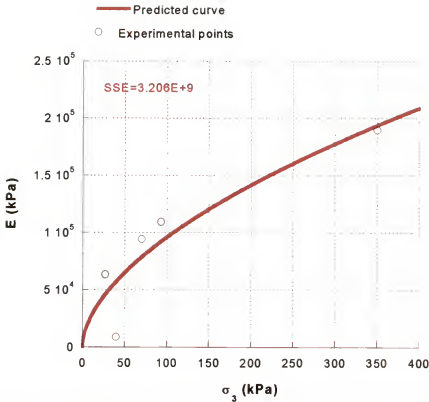


Figure 4.14: Experimental variation of E (average values) with confining pressure compared to Duncan and Chang power law.

Lade and Duncan (1975) applied equation (4.6) to approximate the E values for Sacramento sand. He reported K_{ur} values of 1680 and n_{ur} of 0.57 for a Poisson ratio (ν) of 0.2.

Note that according to equation (4.6) under unconfined conditions ($\sigma_3 = 0$), the E value is zero. This is physically unacceptable. To better characterize the stress dependency of the elastic moduli, relationships in terms of the stress invariant should be examined. For triaxial compression conditions: $\sigma_2 = \sigma_3$ (cylindrical symmetry), the first stress invariant I_1 is:

$$I_1 = \sigma_1 + 2 \cdot \sigma_3 \quad (4.7)$$

The experimental values of E obtained from all the tests (i.e. the estimates obtained from the slopes of all unloading cycles) versus the mean stress I_1 are plotted in Figure 4.15. A decaying exponential function of I_1 (equation 4.8) fits the data well

$$E = E_{\infty} + \gamma \cdot p_a \cdot e^{-\delta \left(\frac{I_1}{p_a} \right)} \quad (4.8)$$

where E_{∞} is an asymptotic value corresponding to very high pressures, p_a is the atmospheric pressure ($1.012 \cdot 10^2$ kPa), γ and δ are material constants.

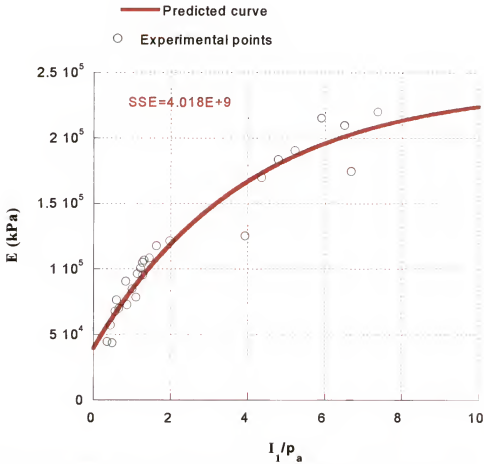


Figure 4.15: Experimental variation of E with confining pressure compared to exponential variation of E (equation 4.3).

For silica powder, it was found that $E_{\infty} = 2.25 \cdot 10^5$ kPa, $\gamma = -1.78 \cdot 10^3$ and $\delta = 0.252$. Similarly, the variation of the bulk modulus K (Figure 4.16) with the mean stress was approximated by:

$$K = K_{\infty} + \psi \cdot e^{-\beta \frac{I_1}{p_a}} \quad (4.9)$$

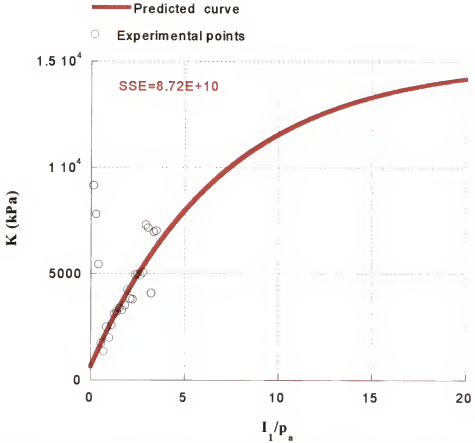


Figure 4.16: Experimental variation of K (average values) with confining pressure compared to exponential variation of K (equation 4.9).

The numerical values of the parameters involved in equation (4.9) are:

$$K_{\infty} = 1.48 \cdot 10^4 \text{ kPa}, \quad \psi = -1.38 \cdot 10^2 \text{ and } \beta = 0.415.$$

4.6 Modeling the Observed Irreversibility in Behavior using Elastic/Perfect Plastic Models

First, the data were interpreted in terms of the Mohr-Coulomb criterion (see equation (2.1), section 2.1). In this model it is assumed that the material is perfectly plastic, i.e., the yield locus is fixed in the stress space.

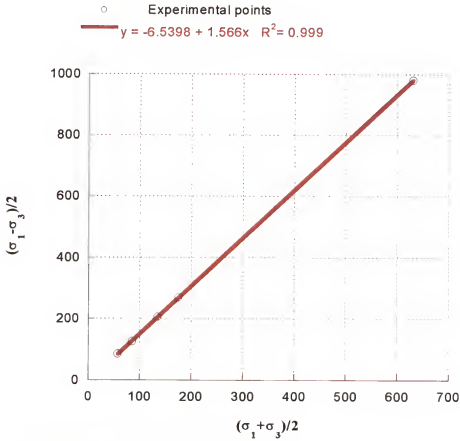


Figure 4.17: Mohr-Coulomb yield surface

The yield surface coincides with the failure surface:

$$\frac{\sigma_1 - \sigma_3}{2} = \frac{\sigma_1 + \sigma_3}{2} \cdot \sin \phi + c \cos \phi \quad (4.10)$$

where σ_1 and σ_3 are the major and minor principal stresses, respectively; c is the cohesion, and ϕ is the angle of internal friction. The cohesion and the angle of internal friction were estimated from compression data. Figure 4.17 shows a comparison between model and data. It was found that $c = 0.56$ kPa and $\phi = 33^\circ$.

The Drucker-Prager criterion (see equation 2.4, section 2.2.1.2) was also used to interpret the data. The advantages of using Drucker-Prager over Mohr- Coulomb are: (1) it is expressed in terms of stress invariants and thus can be applied to describe failure surface under any loading conditions, and (2) it has been proven to accurately describe the strength characteristics of granular media.

For axisymmetric triaxial loading conditions the criterion is expressed as:

$$\frac{\sigma_1 - \sigma_3}{\sqrt{3}} = \alpha_{DP} \cdot (\sigma_1 + 2\sigma_3) + k_{DP} \quad (4.11)$$

$\alpha_{DP} = 0.3197$ and $k_{DP} = 1.340$ kPa. Comparison between model predictions and data is shown in Figure 4.18.

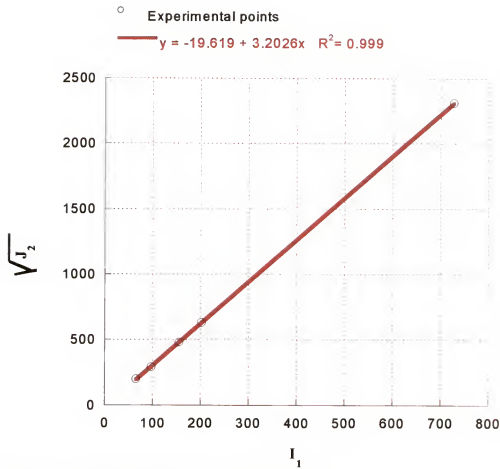


Figure 4.18: Drucker-Prager yield surface for silica.

4.7 Two-Surface Elastic/Plastic Model, Lade (1977)

The elastoplastic theory developed by Lade (1977) was validated for the stress-strain behavior of cohesionless sand under cyclic loading (Lade 1977; Lade and Booyanyachut 1982). In this theory the total strain increment $d\epsilon$ due to a stress increment $d\sigma$, is divided in three components:

- A) an elastic strain component $d\epsilon^{el}$
- B) a plastic collapse strain increment component $d\epsilon^{col}$, and
- C) a plastic expansive strain increment component $d\epsilon^{exp}$. These strain components are calculated separately and then added together:

$$d\epsilon_{ij} = d\epsilon_{ij}^{el} + d\epsilon_{ij}^{col} + d\epsilon_{ij}^{exp} \quad i, j = 1 \dots 3 \quad (4.12)$$

The elastic strain is computed using a non-linear Hooke's law. The plastic collapse strain is given by a plastic stress-strain theory involving a cap-type yield surface and the plastic expansive strains by a stress-strain theory, which involves a conical yield surface with apex at the origin of the stress space. Both elastic (recoverable) and plastic (irrecoverable) deformations occur from the beginning of loading of a cohesionless soil. The stress-strain relationship is non-linear, and a decrease in strength follows failure (softening behavior). The volumetric strain is initially compressive and this behavior may be followed by expansion or continued compression. The plastic strains are initially smaller than the elastic strains, but at higher values of stress the plastic strains dominate the elastic strains. The basic assumptions of this model are:

- small deformations
- isotropic hardening and softening,
- two yield surfaces corresponding to each mechanism of plastic deformation.

4.7.1 Determination of the Plastic Collapse Strain Increment

It is assumed that under hydrostatic conditions, the material is compressible only; and the irreversibility of its behavior is due to pore collapse. The collapse behavior is modeled by the yield function:

$$f_c = F(W) \quad (4.13)$$

where W is the irreversible stress work $W = \int \sigma_y d\epsilon_{ij}^{irreversible}$ and $f_c = I_1^2 + 2 \cdot I_2^2$,

with $I_1 = tr \underline{\sigma}$, $I_2 = \frac{1}{2} tr \underline{\sigma}^2 - \frac{1}{2} (tr \underline{\sigma})^2$.

For hydrostatic conditions ($\sigma_1 = \sigma_2 = \sigma_3$): $I_1 = 3\sigma_3$ and $I_2 = -3\sigma_3^2$ so:

$$f_c = (3\sigma_3)^2 + 2(-3\sigma_3^2) = 3\sigma_3^2 \quad (4.14)$$

As the value of f_c increases beyond its current value, the material hardens and collapse strains are produced. For hydrostatic conditions:

$$dW = \sigma_3 \cdot d\varepsilon_v^c, \quad (4.15)$$

where σ_3 is the applied pressure and $d\varepsilon_v^c$ is the plastic volumetric strain increment. For a given system, the plastic collapse work-hardening function $F(W)$ should be specified. Lade (1977) proposed the following expression for the collapse yield function of a cohesionless soil:

$$W = U \cdot p_a \left(\frac{f_c}{p_a^2} \right)^{\frac{1}{d}}, \quad (4.16)$$

or

$$f_c = \left(\frac{W}{U \cdot p_a} \right)^d p_a^2, \quad (4.17)$$

where U and d are material constants and p_a stands for the atmospheric pressure.

To determine the numerical values of these parameters for silica, data from a hydrostatic compression test up to 350 kPa are used. The results of this test are shown in Figure 4.19.

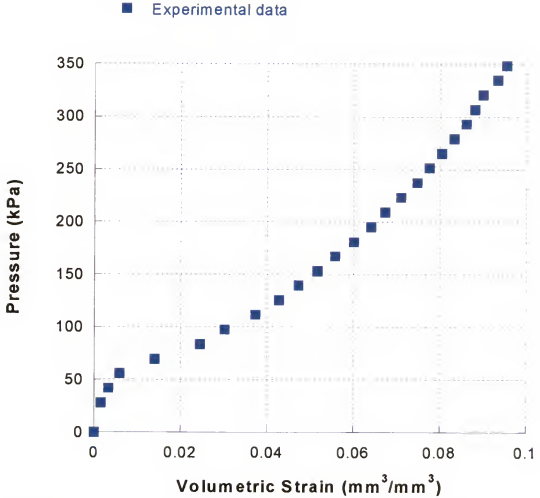


Figure 4.19: Pressure vs. volumetric strain curve obtained in hydrostatic test.

The variation of the irreversible work with the applied pressure was calculated first considering a power law variation for the elastic parameters (equation 4.6). That is, at a given level of stress, the elastic strain was computed using the stress value and the elastic parameters, then the irreversible strain was computed as a difference between the total strain and the elastic strain. The irreversible strain is used then together with equation (4.15) to compute the irreversible work, W . Similarly f_c is computed plugging the stress value in equation (4.14).

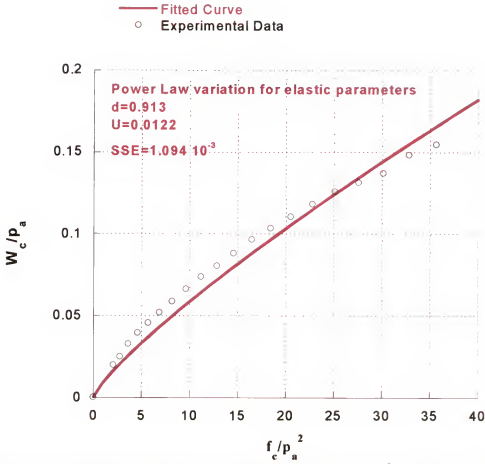


Figure 4.20: Collapse stress work/atmospheric pressure vs. f_c/p_a^2 , using power law variation for K in the computation of the elastic behavior. Fitted curve results: $d=0.913$, $U=0.0122$.

Thus, an experimental curve for $\frac{W}{p_a}$ versus $\frac{f_c}{p_a^2}$ is plotted (see Figure 4.20). The

parameters U and d were obtained by approximating the experimental curve with the expression (4.17), approximation that uses a built-in iterative procedure in MATHCAD together with a guess value. In the case of power law for K (bulk modulus), U and d were 0.0122 and 0.913 respectively with a sum of squares error (SSE) of $1.094 \cdot 10^{-3}$ (see Figure 4.20).

Considering then an exponential law variation (equation 4.9), the above procedure was repeated. For the exponential variation of K , U and d were obtained to be 0.0122 and 0.913 respectively (same constants as when the power law for K was considered), and the sum of square errors (SSE) was $1.026 \cdot 10^{-3}$ (see Figure 4.21).

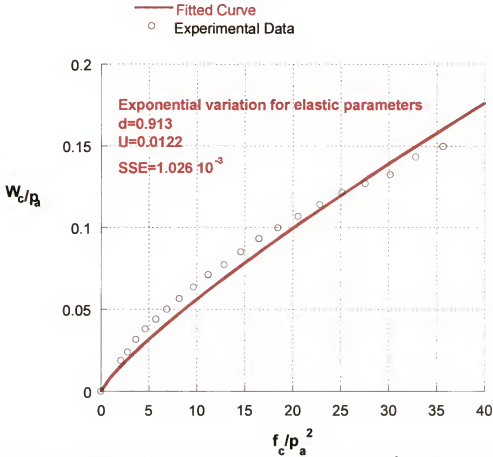


Figure 4.21: Collapse stress work/atmospheric pressure vs. f_c/p_a^2 , using exponential law variation for K in the computation of the elastic behavior. Fitted curve results: $d=0.913$, $U=0.0122$.

Since the parameters U and d play an important role in the determination of the hydrostatic plastic response, their sensitivity to initial guesses for the iterative fitting procedure was studied. Starting from guess values of $d=1$, $U=0.0122$ and $d=1$,

$U=0.0121$, the initial guesses were returned as best values, giving a SSE of $1.873 \cdot 10^{-3}$ and $1.877 \cdot 10^{-3}$, respectively (see Figures 4.22 and 4.23). As all fitting results were close to each other and equally good, to decide which d and U apply better to Lade model a numerical simulation (true test of the model) is necessary. In Chapter 6 several numerical simulations were performed concluding that the simulation performed with $d=1$ and $U=0.0122$ showed the best agreement with the experimental data. As substituting $d=1$ in Equation 4.17 simplifies the dependence of f_c to W to a linear expression, this demonstrated that a linear collapse yield function is more adequate than a power function to describe the hydrostatic mechanical response of silica powder using the Lade model.

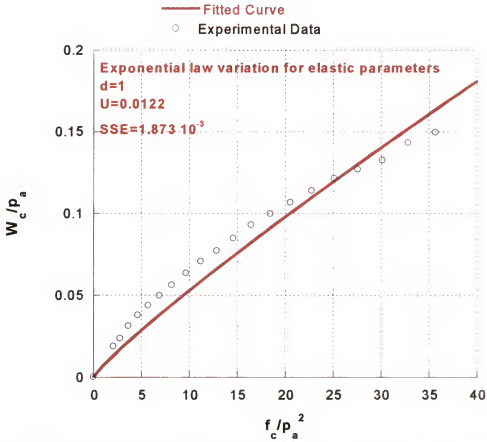


Figure 4.22: Collapse stress work/atmospheric pressure vs. f_c/p_a^2 , using exponential law variation for K in the computation of the elastic behavior. Fitted curve results: $d=1$, $U=0.0122$.

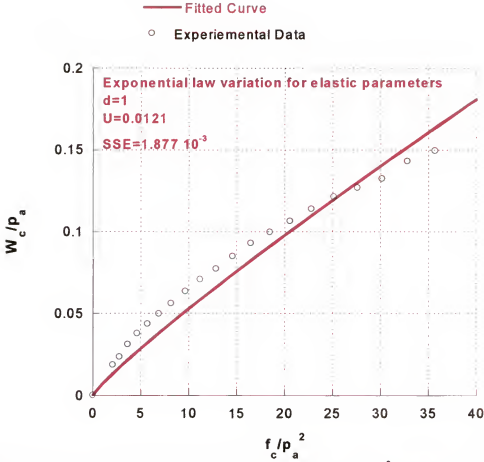


Figure 4.23: Collapse stress work/atmospheric pressure vs. f_c/p_a^2 , using exponential law variation for K in the computation of the elastic behavior. Fitted curve results: $d=1$, $U=0.0121$.

4.7.2 Flow Rule for Hydrostatic Conditions

Isotropic compression of an isotropic material results in equal linear strains in the three principal directions. Thus, for this condition the strain increment vector should be pointed in the direction outward from the origin and coincide with the hydrostatic axis. For this condition to be fulfilled the plastic potential function g_c , should coincide with yield function, f_c (Mendelson, 1968).

$$d\epsilon_y^c = d\lambda_c \cdot \left(\frac{\partial g_c}{\partial \sigma_y} \right) \quad (4.18)$$

where $d\lambda_c$ is a differential positive multiplier, which is calculated using the consistency

$$\text{condition: } \frac{\partial f_c}{\partial \sigma_y} \dot{\sigma}_y + \frac{\partial f_c}{\partial W} \dot{W} = 0$$

Using the work hardening law from (4.17) gives:

$$d\lambda_c = \frac{-6\sigma_3 d\sigma_3}{3\sigma_3 \cdot 2\sigma_3 \left[\frac{1}{d} \left(\frac{W}{Up_a} \right)^{\frac{1}{d}-1} \frac{p_a}{U} \right]} \quad (4.19)$$

(See Appendix B for details in the computation of λ_c)

Hence,

$$\dot{\epsilon}_v^c = \frac{-6\dot{\sigma}_3 k d}{3^{1-d} \sigma_3^{2(1-d)} p_a^{1-\frac{2(1-d)}{d}}} \quad (4.20)$$

4.7.3 Determination of the Plastic Expansive Strain Increment

The expansive behavior is governed by the following yield function:

$$f_p = \left(\frac{I_1^3}{I_3} - 27 \right) \cdot \left(\frac{I_1}{p_a} \right)^m \quad (4.21)$$

where I_3 is the third invariant of the stress tensor, m and η_1 are material parameters. The

failure condition is given by: $f_p = \eta_1$. Note that m is the slope of $\log \left[\left(\frac{I_1^3}{I_3} \right) - 27 \right]$ vs. \log

I_1 / p_a curve at failure while η_1 represents the intercept of the curve. For silica, $m=0.088$

and $\eta_1=10^{1.82}$ (see Figure 4.24).

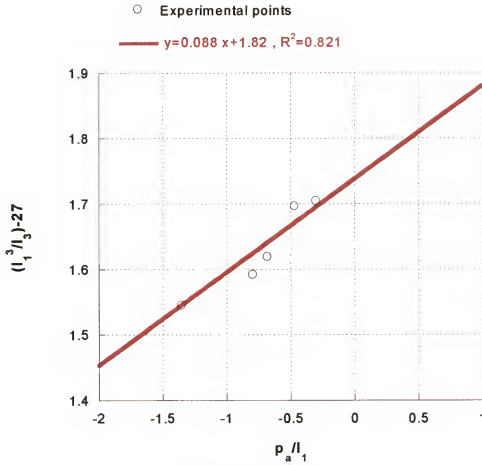


Figure 4.24: Experimental $\log \left[\left(\frac{I_1^3}{I_3} \right) - 27 \right]$ vs. $\log I_1 / p_a$ at failure.

4.7.4 Flow Rule for Deviatoric Conditions

In plasticity theory, it is often assumed that the plastic potential and the yield function coincide. Although this assumption is valid for isotropic conditions, experimental data suggest that in order to accurately model the expansive plastic behavior a non-associated flow rule should be considered. Based on experimental observations, Lade (1977) proposed the following expression of the plastic potential for expansive strains:

$$g_p = I_1^3 - \left(27 + \eta_2 \left(\frac{p_a}{I_1} \right)^m \right) I_3 \quad (4.22)$$

For given values of f_p and σ_3 , η_2 is a constant. The plastic potential describes a series of surfaces, which are normal to the plastic strain increment directions.

The relationship between stress and expansive plastic strain is derived according to the following expression

$$d\varepsilon_{ij}^p = d\lambda_p \cdot \left(\frac{\partial g_p}{\partial \sigma_{ij}} \right) \quad (4.23)$$

where,

$$\frac{\partial g_p}{\partial \sigma_{ij}} = 3I_1^2 \frac{\partial I_1}{\partial \sigma_{ij}} - 27 \frac{\partial I_3}{\partial \sigma_{ij}} + I_3 \left(\eta_2 p_a^m m I_1^{m-1} \frac{\partial I_1}{\partial \sigma_{ij}} \right) - \eta_2 \left(\frac{p_a}{I_1} \right)^m \frac{\partial I_3}{\partial \sigma_{ij}} \quad (4.24)$$

The value of the differential positive multiplier $d\lambda$ determines the magnitude of the plastic strain increment while the value of η_2 determines the directions of the strain increments. The differential positive multiplier $d\lambda_p$ is obtained using the consistency

condition in conjunction with the work hardening law, $W_p = \int \sigma_{ij} \cdot d\varepsilon_{ij}^p$

$$f_p = F(W_p) \quad (4.25)$$

where f_p is the yield function:

$$f_p = \left(\frac{I_1^3}{I_3} - 27 \right) \left(\frac{I_1}{p_a} \right)^m \quad (4.26)$$

and the work-hardening function $F(W_p)$ is specified as:

$$F(W_p) = H \cdot e^{-BW_p} \left(\frac{W_p}{p_a} \right)^{\frac{1}{z}} \quad (4.27)$$

(see Lade (1977))

where: H , B and z are material constants. Hence, the consistency condition is given by

$$\frac{\partial F}{\partial W^p} dW^p = \frac{\partial f_p}{\partial \sigma_{ij}} d\sigma_{ij} \quad (4.28)$$

$$\text{where: } \frac{\partial F}{\partial W^p} = f_p(-B) + \frac{1}{z \cdot W^p} \quad (4.29)$$

$$dW^p = \frac{df_p}{f_p \left(\frac{1}{z \cdot W^p} - B \right)} \quad (4.30)$$

So,

$$d\lambda = \frac{\partial f_p}{\partial \sigma_{ij}} \left[\frac{1}{3g_p + m\eta_2 \left(\frac{p_a}{I_1} \right)^m I_3} \right] \left[\frac{1}{f_p(-B) + \frac{1}{z \cdot W^p}} \right] d\sigma_{ij} \quad (4.31)$$

Using the flow rule (4.23), η_2 can be expressed as:

$$\eta_2 = \frac{3 \cdot (1 + \nu^p) \cdot I_1^2 - 27 \cdot \sigma_3 \cdot (\sigma_1 + \nu^p \cdot \sigma_3)}{\left(\frac{p_a}{I_1} \right)^m \cdot \left[\sigma_3 \cdot (\sigma_1 + \nu^p \cdot \sigma_3) - \frac{m \cdot (1 + \nu^p) \cdot I_1^2}{f_p \cdot (p_a / I_1)^m + 27} \right]} \quad (4.32)$$

$$\text{where } \nu^p = -\frac{\Delta \varepsilon_3^p}{\Delta \varepsilon_1^p}$$

In order to determine ν^p from the triaxial compression tests, the plastic increments were calculated by subtracting the elastic and the plastic collapse strains from the total strains according to equation (4.12). Values of η_2 were calculated from equation (4.32) and plotted vs. $f_p g$ given by equation (4.25).

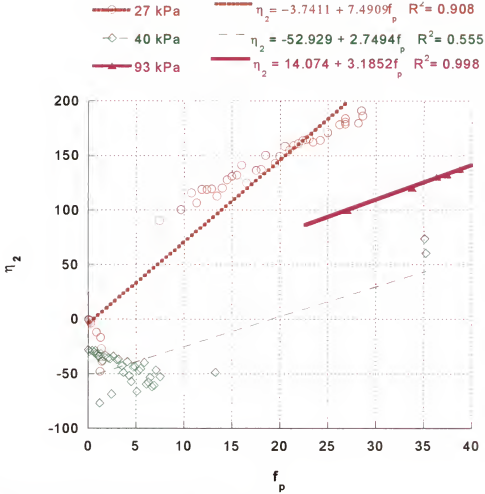


Figure 4.25: Variation of η_2 with f_p and σ_3 .

As Figure 4.25 illustrates, η_2 is linearly related to f_p for constant values of σ_3 .

The variation of η_2 is modeled as:

$$\eta_2 = T \cdot f_p + r \cdot \left(\frac{\sigma_3}{p_a} \right)^{\frac{1}{2}} + t \quad (4.33)$$

From the plot of η_2 vs. f_p , different straight lines are obtained for each confining pressure. In equation (4.33) T represents the average value of the slope of the straight lines and the last two terms (which contain r and t) model the variation of the intercept of

the straight lines. Hence, by plotting the intercepts vs. $(\sigma_3/p_a)^{0.5}$ the parameters r and t could be computed. For silica $r = 77.241$ and $t = -68.34$ (see Figure 4.26).

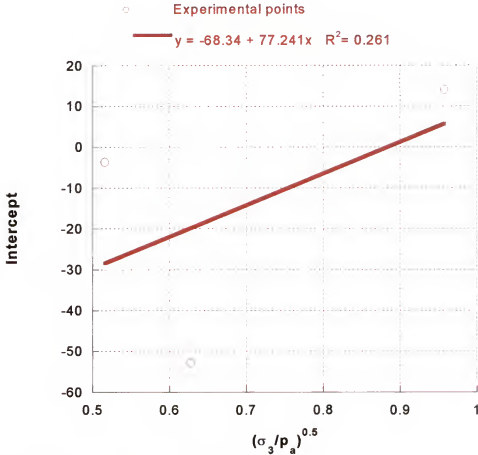


Figure 4.26: Variation of the intercepts with σ_3

Negative values of η_2 correspond to plastic volumetric strains, which are compressive, and positive values of η_2 correspond to plastic expansive strains.

The experimental data show that the values of η_2 were much smaller than f_p . This indicates that the plastic potential surface and the yield surface did not coincide, so the normality criterion cannot be applied for silica and the yield function cannot coincide with the plastic potential.

4.7.5 Work Hardening Law

In order to estimate the parameters that determine the relationship between W_p and f_p (equation 4.27), the value of W_p at the peak stress (level of stress at failure) is needed, to distinguish the parts that f_p (yield function) is increasing. The values of H , B and z in equation (4.27) can be determined according the expressions 4.34, 4.35 and 4.36.

$$H = \eta_1 \left(\frac{e \cdot p_a}{W_{ppeak}} \right)^{\frac{1}{z}} \quad (4.34)$$

$$B = \frac{1}{z \cdot W_{ppeak}} \quad (4.35)$$

$$z = \frac{\log \frac{W_{ppeak}}{W_{p60}} - \left(1 - \frac{W_{p60}}{W_{ppeak}} \right) \cdot \log e}{\log \frac{\eta_1}{f_{p60}}} \quad (4.36)$$

where $f_p = \eta_1$, $W_p = W_{ppeak}$ for each confining pressure and (W_{ppeak}, η_1) and (W_{p60}, f_{p60}) are two sets of corresponding values at a determined confining pressure.

The variation of W_{ppeak} with the confining pressure can be approximated as:

$$W_{ppeak} = P \cdot p_a \cdot \left(\frac{\sigma_3}{p_a} \right)^L \quad (4.37)$$

where P and L are constants and p_a is atmospheric pressure. It was found $L = 0.4$ and $P = -1.02$ (see Figure 4.27).

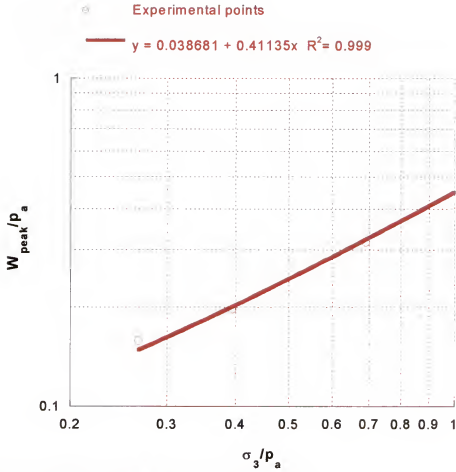


Figure 4.27: Variation of W_{peak} with confining pressure.

Figure 4.28 shows the variation of z with confining pressure, which could be expressed as:

$$z = \kappa + \xi \cdot \frac{\sigma_3}{p_a} \quad (4.38)$$

where κ and ξ are the intercept and the slope of the straight line. For silica $\kappa = 0.384$ and $\xi = -0.04$

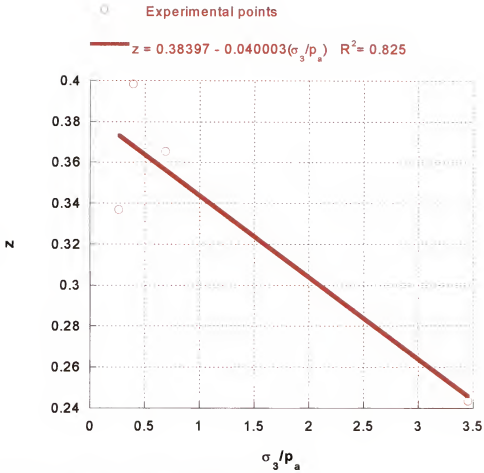


Figure 4.28: Variation of z with confining pressure.

4.8 Summary of the Parameters involved in Lade Model (1977) and the Corresponding Numerical Values for Silica Powder

A summary of parameters of the Lade model for silica powder is presented in Table 4.4. The parameter values will be used as input in the numerical simulations (see Chapter 6). These simulations will allow us to test the predictive capabilities of the model.

Table 4.4: Parameters of Lade model (1977) for silica powder.

Parameters, (Lade 1977)	Silica powder values	Regime
K_{ur}	796.91	<i>Elastic</i>
n_{ur}	0.78080	
Collapse modulus, U	0.0122	<i>Plastic Collapse</i>
Collapse exponent, d	0.913	
Yield const. η_1	63	<i>Plastic Expansive</i>
Yield exponent, m	0.088	
r	77.24	
T	4.46	
t	-68.34	
κ	0.384	
ξ	-0.04	
P	-1.02	
L	0.4	

In Figure 4.29 (a), the spherical and the conical yield surfaces of silica powder are plotted in the triaxial plane, that is, $(\sigma_1 \sqrt{2} \cdot \sigma_3)$ plane. In Figure 4.29 (b), the conical yield surface of silica is shown in the octahedral plane

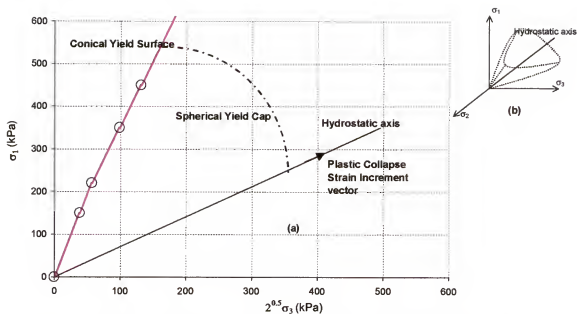


Figure 4.29: (a) Silica yield surfaces in a triaxial plane; (b) representation of the silica conical yield surface in the octahedral plane.

CHAPTER 5

STUDY OF THE QUASI-STATIC DEFORMATION OF DRY POLYMER PELLETS

5.1 Introduction

An investigation into the factors controlling the compaction properties of a commercial polymer system (polyethylene pellets) under various loading conditions was carried out. To this end, triaxial compression tests were performed. Measurements of the volume changes of the sample as a function of the applied shearing stress were used to determine the evolution of the bulk density and compaction behavior. The experimental set up and procedures used were the same as for dry silica powder

The test results are presented as a series of stress-strain curves obtained at different confining pressures and a fixed strain rate. In the following, the results obtained from these tests, data analysis and calibration of Mohr-Coulomb, Drucker-Prager and Lade models are presented.

5.2 Experimental Program

5.2.1 System under Study

The material under study was Polyethylene (PE) in pellet form. The composition of the pellets was Polyethylene > 99% and Talc < 0.1%-1.0%. Their appearance was translucent, white and soft. In general, the pellets were uniform and cylindrical in shape (4 millimeters in height by 3 millimeters in diameter). The particle density was 0.91 g/cm³. The initial bulk density of Polyethylene (PE) pellets varied from 0.59-0.63 g/cm³.

5.2.2 Methodology

The bulk properties were investigated by means of triaxial compression tests under dry conditions. The experimental program included:

- hydrostatic tests up to 350 kPa.
- monotonic tests under lateral confining pressure σ_3 of 14.7 kPa and 35 kPa
- cyclic triaxial compression tests consisting of several loading-creep-unloading and reloading cycles under the same confining pressures.

5.3 Results of Monotonic Deviatoric Tests

To identify and characterize the compaction properties of the PE pellets, a series of monotonic triaxial compression tests were performed at $\sigma_3 = 14.7$ kPa and 35 kPa at a constant displacement rate of 0.1 mm/min. Also, to better monitor and characterize the irreversibility of the material behavior, cyclic tests were performed at the same confining pressures.

Figure 5.1 shows a triaxial test being performed on PE pellets and Figure 5.2 shows a PE specimen during a deviatoric test.

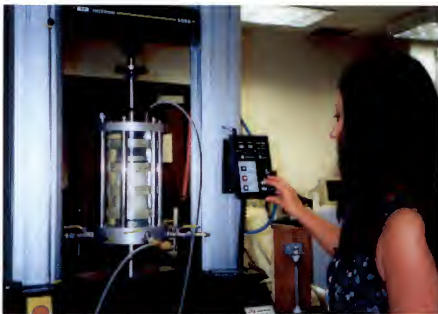


Figure 5.1: Triaxial test on PE pellets in progress.

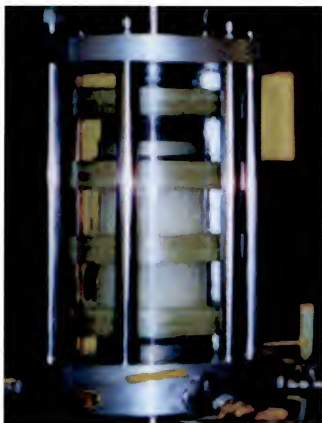


Figure 5.2: PE specimen in triaxial test apparatus

Figure 5.3 shows the stress-strain curve obtained from a test carried out at a confining pressure of 14.7 kPa. The axial strain curve shows that the material underwent elastic deformation up to 75 % of its strength, followed by irreversible deformation and failure. The stress-volumetric strain curve (Figure 5.4) shows two distinct regimes of behavior: first, the pellets compacted (compaction regime) and then expanded (dilation regime).

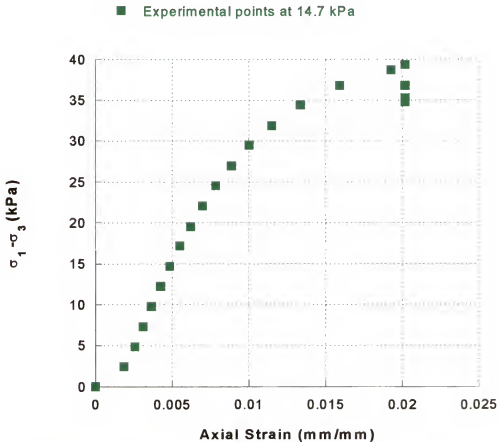


Figure 5.3: Deviatoric stress vs. axial strain at 14.7 kPa of confining pressure.

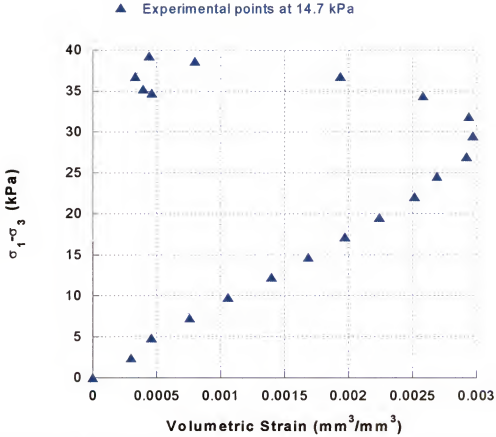


Figure 5.4: Deviatoric stress vs. volumetric strain at 14.7 kPa of confining pressure

The existence of those two regimes of volumetric behavior was observed in both tests. Figure 5.4 shows that the stress value for which the curve deviatoric stress ($\sigma_1 - \sigma_3$) vs. volumetric strain (ϵ_v), changes sign depends on the confining pressure.

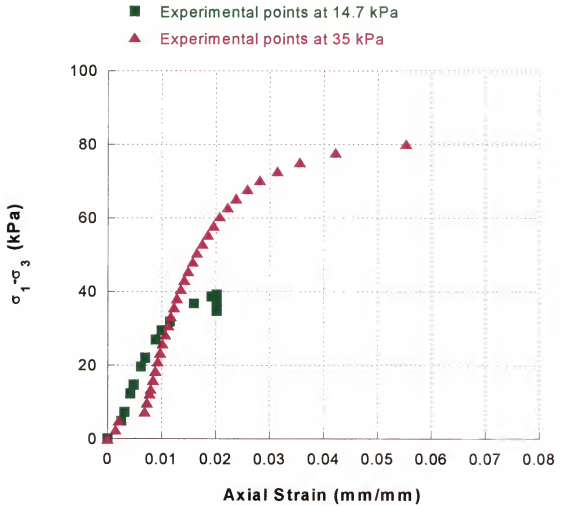


Figure 5.5: Axial strain profiles at confining pressures of 14.7 kPa, and 35 kPa.

These critical points define the boundary between the compressible and dilatant regimes. Figure 5.5 shows the effect of the confining pressure on the strength of the material. In Table 5.1 it can be observed that the strength of the material was an increasing function of the applied confining pressure.

Table 5.1: Strength of the material and dilatancy threshold as a function of the confining pressure obtained in monotonic tests.

σ_3 , kPa (Confining pressure)	$\sigma_{failure}$, kPa (Compressive strength)	$\sigma_{dilatancy}$, kPa (Stress difference corresponding to the dilatancy threshold)
14.7	39	30
35	87	66

5.4 Results of Cyclic Deviatoric Tests

To better characterize the influence of stress on the elastic response of the material, cyclic tests were performed under confining pressures of 14.7 kPa and 35 kPa. Figure 5.6 shows the results obtained in a test under 35 kPa confining pressure. The test consisted of four loading- unloading and reloading cycles. Before changing from loading to unloading, the load was held constant for 20 minutes in order to permit the sample to reach a quasi-stable state. Then, unloading and further reloadings were performed. The Young's modulus (E) was determined from the slopes of deviatoric stress versus axial strain.

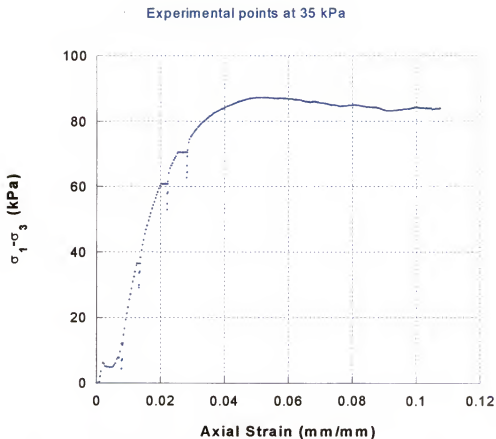


Figure 5.6: Deviatoric stress vs. axial strain at 35 kPa confining pressure

A dependence of E on the on the mean stress ($I_1 = \sigma_1 + 2 \cdot \sigma_3$) was observed. The bulk modulus, K was evaluated from the unloading slopes of deviatoric stress ($\sigma_1 - \sigma_3$) vs. volumetric strain (ε_V) curve (Figure 5.7).

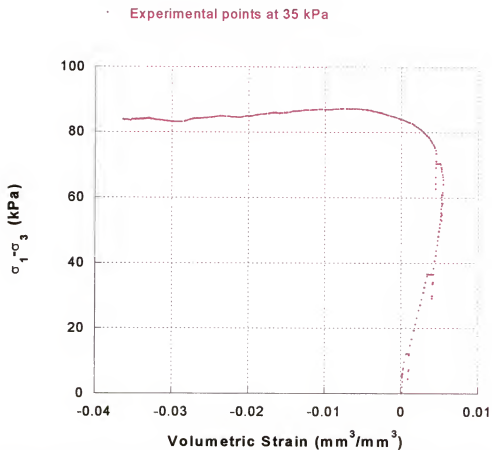


Figure 5.7: Deviatoric stress vs. volumetric strain at 35 kPa confining pressure.

Note also a change in the creep direction at the transition from the compressive regime to the dilatancy regime. This effect can be clearly seen in the blow-up of the stress-volumetric strain curve shown in Figure 5.8.

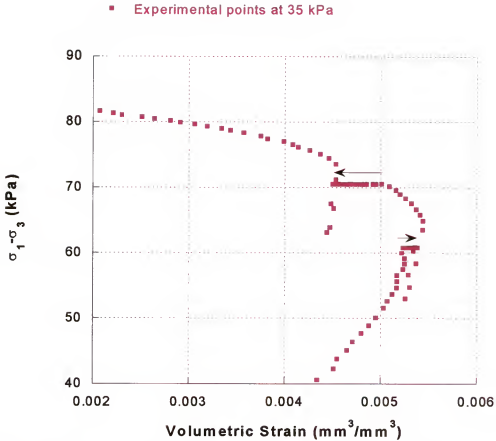


Figure 5.8: Change in creep direction (arrow directions) at the transition from compressibility to dilatancy (lateral confining pressure of 35 kPa).

5.5 Modeling the Behavior in the Elastic Regime

In the elastic range, the behavior was approximated by Hooke's law (see equation 4.1).

As for silica, the Young's modulus E and the Bulk modulus K were estimated directly from the slope of the unloading deviatoric stress vs. ϵ_1 curves and deviatoric stress vs. volumetric curves, respectively. The values of E and K obtained from the unloading slopes in a test at $\sigma_3 = 35$ kPa are given in Table 5.2

Table 5.2: Elastic constants as obtained in a cyclic triaxial compression test under a confining pressure of 35 kPa.

Cycle	E (kPa)	K(kPa)
1	23988	17400
2	22996	17700
3	29647	14800
4	31981	22000

In Figure 5.10 the experimental values of E obtained from the slopes of all unloading cycles are plotted versus the first stress invariant I_1 . A decaying exponential function of I_1 introduced in section 4.6 (eqs. 4.3) was fitted (see Figure 5.7).

$$E = E_{\infty} + \gamma \cdot p_a \cdot e^{-\delta \left(\frac{I_1}{p_a} \right)} \quad (5.4)$$

It was found that for the PE pellets: $E_{\infty} = 2.5 \cdot 10^4$ kPa $\gamma = -9.75 \cdot 10^3$ and $\delta = 0.0095$. But, it can be seen, the fitting curve (see Figure 5.9) does not represent the real tendency of the PE pellets. Since, the range of pressure of interest in applications is very low and for low pressures E does not show a clear dependence on pressure, it was decided to take $E = 27555$ kPa, the mean arithmetic value from all tests.

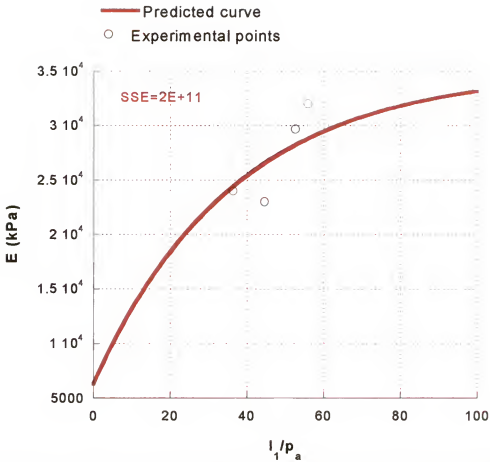


Figure 5.9: Comparison of Young's modulus E , between the theoretical predictions (using equation 5.4) and data (circles).

5.6 Modeling the Observed Irreversibility in Behavior using Elastic/Perfect Plastic Models

First, the data were interpreted in terms of the Mohr-Coulomb criterion. In this model it was assumed that the material was perfectly plastic, i.e. the yield locus was fixed in the stress space and that the yield surface (see Chapter 4, equation 4.10) coincided with the failure surface. Figure 5.10 shows a comparison between the model and observed data.

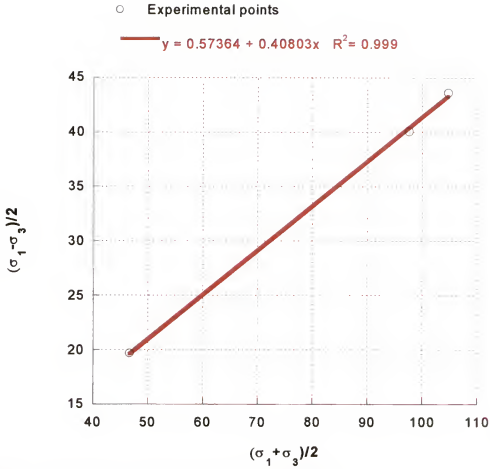


Figure 5.10: Mohr-Coulomb yield surface for PE pellets

The cohesion and the angle of internal friction were estimated from compression data. It was found that (cohesion) $c = 0.62$ kPa and (angle of internal friction) $\phi = 23^\circ$.

The Drucker Prager criterion (equation 4.11) was also used to interpret the data. The advantages of using Drucker-Prager over Mohr-Coulomb were discussed in Chapter 4, section 4.6. The parameters were found to be: $\alpha_{DP} = 0.59$ and $k_{DP} = 5.76$. A comparison between model predictions and data is shown in Figure 5.11.

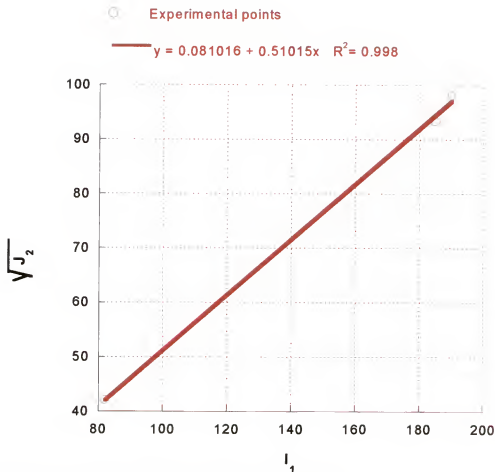


Figure 5.11: Drucker-Prager yield surface for PE pellets.

5.7 Two-Surface Elastic/Plastic Model, Lade (1977)

The same elastoplastic theory developed by Lade (1977) used for silica earlier in this dissertation (see section 4.7) was used for PE pellets.

5.7.1 Determination of the Plastic Collapse Strain Increment

In Figure 5.12 are shown the results of a hydrostatic compression test up to 350 kPa. The behavior of PE pellets during isotropic compression is purely elastic and there is no plastic deformation; therefore, the variation of the irreversible work with the applied pressure is zero.

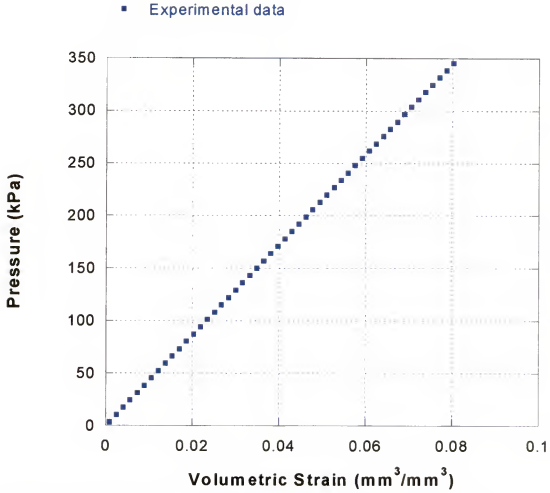


Figure 5.12: Pressure vs. volumetric strain curve obtained in hydrostatic test.

5.7.2 Determination of the Plastic Expansive Strain Increment

The same approach taken for silica in section 4.7.2 was taken here for PE pellets.

The expansive behavior is governed by the following yield function

$$f_p = \left(\frac{I_1^3}{I_3} - 27 \right) \cdot \left(\frac{I_1}{p_a} \right)^m \quad (5.5)$$

while the failure condition is given by: $f_p = \eta_1$

where I_3 is the third invariant of the stress tensor, m and η_1 are material parameters.

To estimate these parameters, $\log \left[\left(\frac{I_1^3}{I_3} \right) - 27 \right]$ vs. $\log I_1 / p_a$ was plotted at failure

(see Figure 5.13). Note that m is the slope of that curve while η_1 represents the intercept.

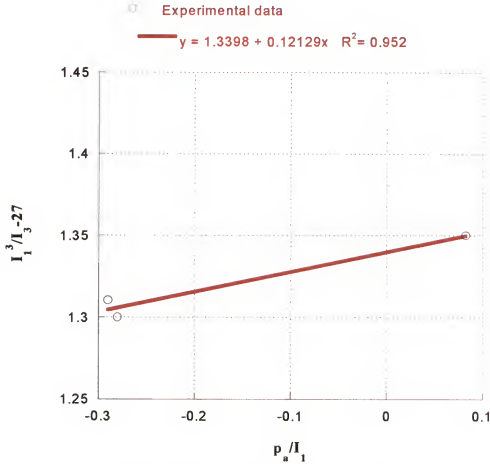


Figure 5.13: Experimental $\log \left[\left(\frac{I_1^3}{I_3} \right) - 27 \right]$ vs. $\log I_1 / p_a$ at failure.

Values of $m = 0.12$ and $\eta_1 = 10^{1.33}$ were computed by fitting the experimental data with equation (5.5) in Figure 5.13.

5.7.3 Flow Rule for Deviatoric Conditions

The evaluation of the model parameters for deviatoric conditions for PE pellets was done in the same manner as for silica powder (see Chapter 4, section 4.7.3).

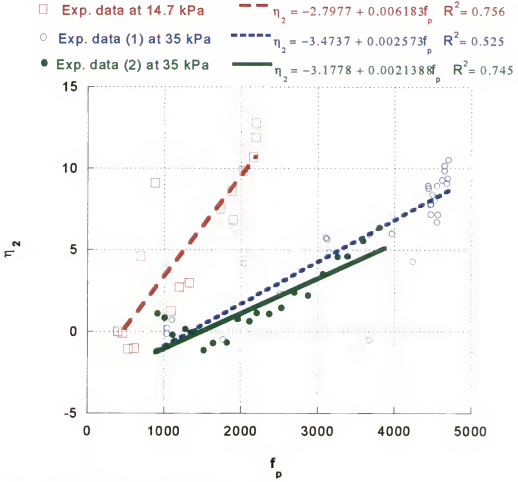


Figure 5.14 : Variation of η_2 with f_p and σ_3 .

The variation of η_2 with f_p (equations 4.32 and 4.26) was evaluated by plotting η_2 vs. f_p . (see Figure 5.14). As shown in Figure 5.14, η_2 is linearly related to f_p for constant values of σ_3 . The variation of η_2 is modeled as:

$$\eta_2 = T \cdot f_p + r \cdot \left(\frac{\sigma_3}{p_a} \right)^{\frac{1}{2}} + t \quad (5.6)$$

From the plot of η_2 vs. f_p , different straight lines were obtained for each confining pressure. In equation (5.6), T represents the average value of the slope of the straight lines and the last two terms (which contain r and t) model the variation of the intercept of the straight lines. Then by solving the equations at confining pressures of 14.7 kPa and 35 kPa, $r = -3.265$ and $t = -1.554$ were computed.

Negative values of η_2 correspond to plastic volumetric strains, which are compressive, and positive values of η_2 correspond to plastic expansive strains. Note that in Figure 5.14, PE pellets compressed slightly at small stress levels while expansive strains were produced at higher stresses. Also, the diagram indicates that compression is most pronounced for higher confining pressures.

The experimental data show that the values of η_2 are much smaller than f_p . This indicates that the plastic potential surface and the yield surface did not coincide, so the normality criterion could not be applied for PE pellets and the yield criterion could not replace the plastic potential. If η_2 were equal to f_p at all stress levels, the plastic potential would be identical to the yield function and the normality criterion would apply to the PE material.

5.7.4 Work Hardening Law

The same hardening law used for silica powder was used for PE pellets (see Chapter 4, section 4.7.5). The plastic work at each stage of the triaxial compression tests was calculated from:

$$W_p = \int \sigma_y \cdot d\epsilon_{ij}^p \quad (5.7)$$

To determine the hardening parameters present in the function that relates W_p with f_p (eq.4.27), the equations 4.34, 4.35 and 4.36 were utilized.

The variation of W_{peak} with the confining pressure was evaluated as:

$$W_{peak} = P \cdot p_a \cdot \left(\frac{\sigma_3}{p_a} \right)^L$$

where P and L are constants determined in Figure 5.15 and p_a is atmospheric pressure. It was found that $L=0.12$ and $P=0.977$

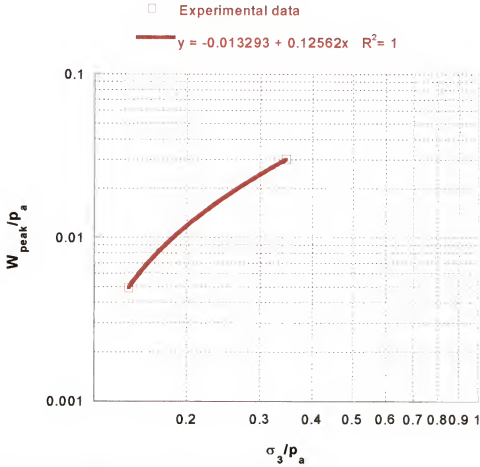


Figure 5.15: Variation of W_{peak} with confining pressure

The variation of z with confining pressure shown in Figure 5.16 can be expressed as:

$$z = \kappa + \zeta \cdot \frac{\sigma_3}{p_a} \quad (5.5)$$

where κ and ξ are the intercept and the slope of the straight line. For PE pellets $\kappa=0.14047$ and $\xi=-0.4447$.

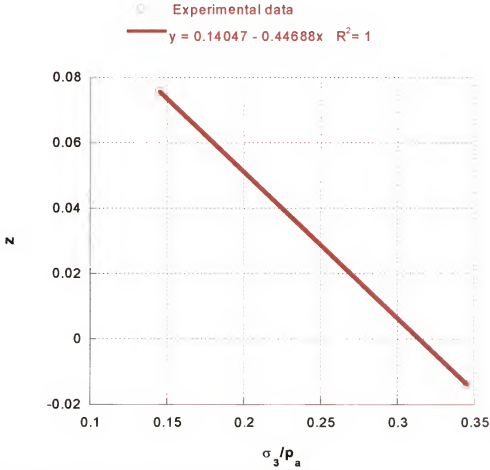


Figure 5.16: Variation of z with confining pressure

5.8 Summary of the Parameters involved in Lade Model (1977) and the Corresponding Numerical Values for PE Pellets

In Table 5.3 a summary of parameters of Lade model for PE pellets is presented.

Table 5.3: Parameters of Lade model (1977) for PE pellets.

Parameters, (Lade, 1977)	PE pellets values	Regime
E	27555 kPa	<i>Elastic</i>
K	17975 kPa	
Collapse modulus, U	0	<i>Plastic Collapse</i>
Collapse exponent, d	0	
Yield const. η_1	21.37	<i>Plastic Expansive</i>
Yield exponent, m	0.12	
r	-3.265	
T	0.033	
t	-1.554	
κ	0.14047	
ξ	-0.4467	
P	0.977	
L	0.125	

The spherical and the conical yield surfaces for PE in the triaxial plane, i.e. σ_1 vs.

$\sqrt{2} \cdot \sigma_3$ are presented in Figure 5.17.

The parameters listed in table 5.3 will be used in the numerical simulations (see Chapter 6). The predictive capabilities of Lade model will be tested by comparing simulation results against experimental data.

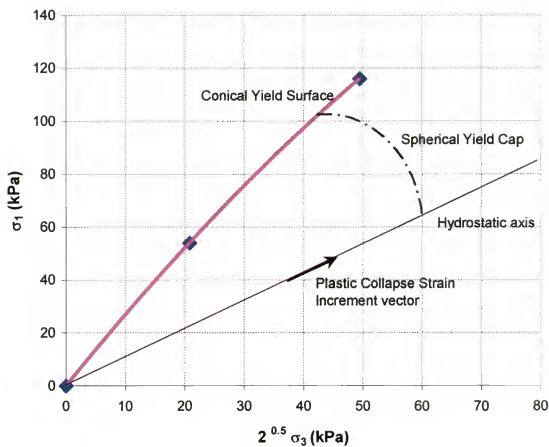


Figure 5.17: Yield surfaces for PE pellets in triaxial plane

CHAPTER 6 NUMERICAL SIMULATION

6.1 Introduction

In the powder technology literature it is often claimed that the behavior of powders and pellets can be correctly described using elastic/perfect plastic models. One of the objectives of this dissertation is to evaluate the validity and applicability of a widely used elastic plastic model, Lade (1977), to a representative powder system, silica and to a representative industrially important system in form of pellets. To this end, in this chapter, theoretical predictions obtained using both Drucker-Prager and Lade models will be compared to experimental data. The simulation results showed that a good agreement with data was obtained only if the hardening of these systems was accounted for. Only the Lade model reproduced the observed behavior. The outline of this chapter is as follows. An overview of the state of the art in integration of elastic plastic models is presented in **Section 6.1**. Two robust and computationally inexpensive methods (1) the *closest point projection (CPP) algorithm* proposed by Ortiz and Pinsky (1983) and (2) *the convex cutting plane (CCP) algorithm* proposed by Ortiz and Simo (1986) are then applied to the integration of both Drucker-Prager and Lade (1977) models. After a detailed description of these algorithms, simulations of hydrostatic tests are presented in **Sections 6.3** and **6.4**. Comparisons between the two algorithms show the superiority in simplicity and robustness of the CCP algorithm. **Section 6.5** further presents the application of the CCP algorithm to the integration of Lade model for deviatoric loading

as well as a comparison between the obtained simulation results and data for both silica and PE pellets. It is shown that Lade model integrated with the CCP algorithm provides a good description of the behavior of both silica and PE pellets. Further discussion and concluding remarks are given in **Section 6.6**.

6.2 Numerical Considerations

Progress in material modeling has led to more accurate and also more complex materials models, but to make practical use of them, numerical methods must be employed to integrate the material model and thus describe the material behavior for specific initial and boundary conditions. Indeed, in a first phase it is necessary to check the validity of the model, that is, its ability to reproduce the behavior of the material as observed in experimental tests. However, the greatest value of a material model is its *predictive capability*, that its ability to predict the material behavior in a given real situation, i.e. for a given shape of the material body, prescribed initial values of strains and stresses, given boundary conditions. While mathematical theory can guarantee the existence and uniqueness of a solution for a certain initial and boundary value problem, as well as the existence of instabilities, in most cases it is impossible to obtain to a closed-form solution. Instead an approximation of the solutions is obtained by numerical methods.

The advantages of developing/using a material model to predict the mechanical behavior of a given material are obvious. First of all, the need to test a material each time that the loading or boundary conditions change is avoided. Lengthy and expensive experimental testing is reduced to a minimum, which is given by the number of tests necessary for the determination of the specific material constants. Using the determined values of the material constants, computer simulations can be used to integrate the model

equations for new loadings or different boundary conditions, thus providing the information concerning the material behavior necessary for design of equipment or handling. Secondly, numerical simulations could be used to obtain information concerning the material response for stress/strain conditions, which cannot be attained experimentally. Numerical simulations allow testing the applicability of a given material model to a given material for given stress, strain, and strain rate conditions and hence deciding which mathematical formulation reproduces best the observed behavior.

Several algorithms, with differing accuracy and stability properties, have been developed for solving the non-linear problems associated to complex material models. An overview of the state of art in integration of constitutive elastic-plastic equations can be found in Wallin and Ristinmaa (2001). The authors divided the procedures for integration of inelastic constitutive equations in two groups based on implicit or explicit solutions. In the first group, the yield criterion is directly enforced (i.e. the consistency condition has to be fulfilled) and the increment of total strain (for time-independent models) is usually approximated in one step. This method is an *implicit method* since the resulting equations become implicit in the unknown variables. The increment of the plastic strains and the increment of the internal variables are expressed as integrals, which are approximated using some integration rule such as the generalized trapezoidal rule or midpoint rule (Zienkiewics and Taylor 1991) among other proposed methods (Runesson et al. 1999 and Papadopoulos and Taylor 1994). This treatment leaves the increment of plastic multiplier undetermined. However, forcing the yield condition to be fulfilled at some point during the step in the total strain increment determines this unknown. Often, this approach is also referred to as *return methods* since the increment of the plastic

multiplier is adjusted such that the stress point is returned to the yield surface. The name *direct method* is also used for the integration methods belonging to this group (*implicit method*) since in order to determine the plastic multiplier the consistency condition is used in a direct manner.

The second group of procedures for integration of the inelastic constitutive equations is usually known as *explicit methods*. In such methods, the strain increment is divided into a number of sub-steps (Zienkiewics and Taylor 1991; Nyssen 1981; Sloan 1987). After the step-wise calculation is performed, usually with a forward Euler method, a final correction is then carried out such that the yield condition is fulfilled at the end of the increment. The term *indirect methods* is also used for this method (*explicit method*) since the yield condition is used in an indirect manner, that is, the rate form of the yield condition is used to control the rate of the plastic increment. In most computational situations, the direct method and especially the fully implicit form known as the *closest point projection (CPP) method* or backward Euler has become the canonical method for integrating the constitutive equations. The reason for this can be traced back to the radial return algorithm of Wilkins (1964) and Krieg and Key (1976) for a von Mises material, which showed simplicity despite the complexity of the starting equations. Moreover, the approach also turned out to provide a very accurate approximation (Krieg and Krieg 1977) and also to be stable (Ortiz and Popov 1986). Thus, the direct method has been applied to most of the classical material models.

One of the key features, which makes the direct method so attractive, is that after approximating the integrals and enforcing the yield condition, a reduced set of equations is obtained. In some simple cases, such as linear hardening of a von Mises material,

these equations can be solved explicitly. When the constitutive models become more complex, this simplicity is lost. The solution cannot be obtained explicitly, but the set of the algebraic equations can always, in principle, be solved by some iterative scheme (Ortiz and Popov 1986; Simo and Hughes 1998; Runesson et al. 1999).

In conclusion, the literature review strongly suggests the choice of implicit methods. In the remaining of this chapter, two such methods: (1) the *closest point projection (CPP) algorithm* proposed by Ortiz and Pinsky (1983) and (2) the *convex cutting plane (CCP) algorithm* proposed by Ortiz and Simo (1986) and their application to the integration of Drucker-Prager and Lade (1977) models are presented.

6.3 The Closest Point Projection Algorithm and its Application to the Integration of Drucker-Prager Model

When applied to classic plasticity models, the closest point projection (CPP) algorithm leads to systems of nonlinear equations whose solution requires evaluation of the gradients of the plastic flow direction, the normal to the yield surface, the plastic moduli and the elasticity tensor. The final stress is obtained by “returning” the trial stresses to the yield surface through scaling. The return-mapping algorithm characterizes the solution as the closest point projection of the trial state onto the yield surface. Essentially, it involves a Newton iteration for the solution of the nonlinear equation resulting from a backward Euler integration of the flow rule and hardening law. It is an implicit procedure and computationally attractive because the algorithm can be linearized in closed form.

The procedure involves: 1) a routine called load cycle that uses as input the strain history in the form of an initial strain and a succession of strain increments and 2) an iteration sub-routine that calculates the final stress for given strain and stress and a given

strain increment. The assumptions and steps of the CPP algorithm are summarized in sub-section 6.3.1, while the integration of the iteration subroutine in the load cycle is described in sub-section 6.3.2, followed in 6.3.3 by comments on the numerical implementation. The simulation results for silica powder and polymer pellets are presented in 6.3.4 and 6.3.5, respectively, and the section is closed by conclusions in 6.3.6.

6.3.1 Description of the Closest Point Projection Iteration for Drucker-Prager Model

The CPP algorithm applied to Drucker-Prager model follows.

Assumed known:

- elastic material parameters at initial state: K (bulk modulus) and G (shear modulus);
- yield function of Drucker-Prager form (equation 2.3): $f(J_2, I_1) = \sqrt{J_2} - \alpha_{DP} \cdot I_1 - k_{DP}$,
where J_2 is the second invariant of the stress deviator, I_1 is the trace of the stress tensor and α_{DP} , k_{DP} are material constants;
- initial stress, σ_n ;
- the initial total strain ε_n and the plastic strain, ε_n^p and
- final strain ε_{n+1} .

Find:

- final stress σ_{n+1} and
- final plastic strain, ε_{n+1}^p

Steps:

1. Initialize the iteration step $k=0$, the plastic strain, $\varepsilon_{n+1}^{p(0)} = \varepsilon_n^p$, $\Delta\lambda_{n+1}^{p(0)} = 0$.

2. Compute C , the matrix of elastic moduli, possibly depending on the initial stress σ_n through its invariants.

3. Compute the trial elastic stress $\sigma_{n+1}^{(k)} = C : (\varepsilon_{n+1} - \varepsilon_{n+1}^p)$.

4. Compute $[I_1 I_2 I_3]$ the invariants of the stress tensor $\sigma_{n+1}^{(k)}$ and $[J_1 J_2 J_3]$ invariants of its deviatoric stress $\sigma'_{n+1}^{(k)}$.

5. Compute present value of the yield function

$$f_{n+1}^{(k)} = f(\sigma_{n+1}^{(k)}) := \sqrt{|J_2|} - g(I_1, \alpha_{DP}, k_{DP}).$$

6. Evaluate the flow rule law residuals, as: $R_{n+1}^{(k)} = \{-\varepsilon_{n+1}^{p(k)} + \varepsilon_n^p\} + \Delta\lambda_{n+1}^{(k)} \left\{ \frac{\partial f_{n+1}^{(k)}}{\partial \sigma} \right\}$

The expressions of the derivatives of the yield functions f are given in Appendix E.

7. Is $(f_{n+1}^{(k)} \leq \text{tol}_1 \text{ and } \|R_{n+1}^{(k)}\| \leq \text{tol}_2)$ true?

Here matrix norm $\| \cdot \|$ is defined as $\|A\|^2 := \text{tr}(A^T A)$.

8. If yes, the final new stresses are the elastic stresses. END.

9. If not, plastic correction is needed, as follows:

10. Compute the consistent tangent moduli as: $[A_{n+1}^{(k)}]^{-1} = \left[C^{-1} + \Delta\lambda_{n+1}^{(k)} \frac{\partial^2 f_{n+1}^{(k)}}{\partial \sigma^2} \right]$

The expressions of the second derivatives of the yield function with respect to the stress are given in Appendix D.

11. Obtain increments of the consistency parameter

$$\Delta^2 \lambda_{n+1}^{(k)} = \frac{f_{n+1}^{(k)} - R_{n+1}^{(k)} : A_{n+1}^{(k)} : \frac{\partial f_{n+1}^{(k)}}{\partial \sigma}}{\frac{\partial f_{n+1}^{(k)}}{\partial \sigma} : A_{n+1}^{(k)} : \frac{\partial f_{n+1}^{(k)}}{\partial \sigma}}$$

and

$$\Delta \lambda_{n+1}^{(k)} = A_{n+1}^{(k)} : \left[-R_{n+1}^{(k)} - \Delta^2 \lambda_{n+1}^{(k)} \frac{\partial f_{n+1}^{(k)}}{\partial \sigma} \right]$$

Here $a:A: b: = \text{tr}(a^T A b)$.

10. Calculate the incremental plastic strains:

$$\Delta \sigma_{n+1}^{(k)} = \left[C^{-1} + \Delta \lambda_{n+1}^{(k)} \frac{\partial^2 f_{n+1}^{(k)}}{\partial \sigma^2} \right]^{-1} : \left[-R_{n+1}^{(k)} - \Delta^2 \lambda_{n+1}^{(k)} \frac{\partial f_{n+1}^{(k)}}{\partial \sigma} \right]$$

$$\Delta \varepsilon_{n+1}^{p(k)} = -C^{-1} : \Delta \sigma_{n+1}^{(k)}$$

11. Update the state variables and consistency parameter:

$$\varepsilon_{n+1}^{p(k+1)} = \varepsilon_{n+1}^{p(k)} + \Delta \varepsilon_{n+1}^{p(k)}$$

$$\Delta \lambda_{n+1}^{(k+1)} = \Delta \lambda_{n+1}^{(k)} + \Delta^2 \lambda_{n+1}^{(k)}$$

12. Set $k=k+1$ and Return to step 3.

6.3.2 Integration of a Iteration in the Load Cycle

Assumed known:

- Elastic material parameters at initial state: K (bulk modulus) and G (shear modulus)
- Yield function $f(J_2, I_1) = \sqrt{J_2} - g(I_1)$, where J_2 is the second invariant of the stress deviator and I_1 is the trace of the stress tensor.
- Initial stress σ_1
- Total strain history

Find:

- Stress history
- Plastic strain history (once this one is known, the elastic strain at each step would be computed as the difference between the total and the plastic strain).

Procedure:

For $n=1$: number of steps in strain history-1, repeat

$$[\sigma_{n+1}, \epsilon_{n+1}^p] = \text{closest_point_projection}(\sigma_n, \epsilon_{n+1}, \epsilon_n, \epsilon_n^p)$$

that is find the new state of stress and the new plastic strain as a function of the old stress, new total strain, old total strain and old plastic strain.

6.3.3 Comments on the Implementation of General Closest Point Projection Algorithm for Drucker-Prager

MATLAB version 6.1 (MATrix LABoratory developed by The Mathworks, Inc., 2002) routines were developed in order to simulate the behavior of silica powder and PE pellets. MATLAB was chosen because of its unique features such as user-friendly interface, extensibility and external interfaces with C and Fortran. Comments on the implementation of the CPP algorithm are given bellow.

(1) Concerning the iteration procedure presented in section 6.3.1:

In the numerical implementation, C , the matrix of elastic moduli, is considered to be constant during each load step and between load steps. However, the option of updating C from one load step to the next is also possible. Consequently, a counter of iterations for the steps 3-9, (see Section 6.3.1) from $k=1$ to k_{max} (maximum limit) was added. If k_{max} is attained, even if the yield condition or the plastic flow condition is not satisfied, the last computed stress and plastic strain are reported as the final stress σ_{n+1} and the final plastic strain, ϵ_{n+1}^p . All the simulation results presented are obtained for $k_{max}=150$.

In order to be able to invert the consistent tangent matrix A_{n+1} using MATLAB's built-in functions (see Section 6.3.1, Step 10), the condensed notation for a symmetric second order and fourth order tensor were used. In those notations: a six component

vector is associated to a second order 3×3 symmetric matrix, whereas to a fourth order $3 \times 3 \times 3 \times 3$ symmetric matrix is associated a second order 6×6 symmetric matrix. The corresponding components of these tensors are identified using the convention: $11 \leftrightarrow 1$, $22 \leftrightarrow 2$, $33 \leftrightarrow 3$, $23 \leftrightarrow 4$, $31 \leftrightarrow 5$, $12 \leftrightarrow 6$.

The algorithm calls for computation of first and second derivative of the yield function with respect to the stress. Simo and Hughes (1986) noted that the computation of those derivatives might be difficult for complicated expressions of the yield function. However, the derivatives are relatively easy to compute for the Drucker-Prager yield function, so a closed-form of these derivatives was used in the numerical implementation. The expression of these derivatives is given in Appendix E.

(2) Concerning the Load Cycle procedure implementation presented in Section 6.3.2:

Errors in plastic strain due to incomplete convergence in the correction part of the CPP algorithm accumulate from one load step to the next. The stress value at step n , σ_n , is not explicitly used in computation of the stress value at step $n+1$ (the value might appear implicitly if the elastic coefficients depend on the state of stress). However, the computation of σ_{n+1} uses explicitly ε_{n+1}^p which depends on ε_n^p (thus on σ_n as well).

Neither the CPP iteration, nor the load cycle accounts for the boundary conditions (as the one in a triaxial test with lateral confining pressure). The implementation of the boundary conditions is described in the next section.

Boundary Conditions Implementation:

After each iteration of [step 3](#), a correction for the lateral stress components $\sigma_{n+1}(2) = \sigma_{n+1}(3) = \text{confining stress value}$ is added. This is equivalent to computing the

stresses in a matrix space where the lateral stresses are fixed and equal to the confining pressure.

6.3.4 Comparison between Drucker-Prager Predictions under Deviatoric Stress Conditions and Data on Silica Powder and PE Pellets

The simulations were strain driven. The strain history was given as input and stresses were computed using the Drucker-Prager model and CPP algorithm for integration. The following example presents a comparison between theoretical predictions of the response of silica powder subjected to triaxial compression and the confining pressures of 70.6 and 93.6 kPa, respectively. Although, the elastic moduli are stress dependent (see Chapter 4), in the numerical integration scheme (sections 6.3.2 and 6.3.3), the elastic moduli were considered to be constant. Hence, in the simulation of a given test, the average values of isotropic elastic moduli obtained in that test were used. Average values of the elastic constants as determined in the test at 70.6 kPa of confining pressure are: bulk modulus, $K=46\ 836$ kPa and Poisson ratio, $\nu=0.24$. While the average values of the elastic constants at 93.6 kPa used in the simulations being $K=111\ 443.43$ kPa and $\nu=0.31$.

The initial stress value considered in the simulation was the same as in the real experiment:

- For the experiment at 70.6 kPa: [70.6 70.6 70.6 0 0 0] (measured in kPa)
- For the experiment at 93.6 kPa: [93.6 93.6 93.6 0 0 0] (measured in kPa)

Figure 6.1 and Figure 6.2 show the simulation results for two different confining pressures in comparison with experimental data. The initial plastic strain was computed as the initial total strain minus the initial elastic strain and it was non-zero. For non-zero

initial plastic strain, the simulated axial stress started at 70.6 kPa and 93.6 kPa for the respective experiments.

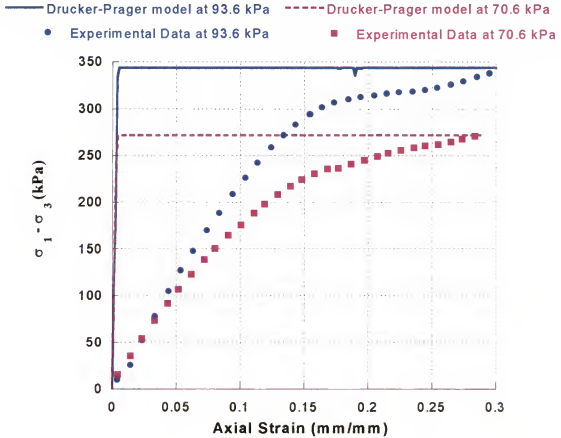


Figure 6.1: Comparison between Drucker-Prager simulation and experimental deviatoric stress versus axial strain at 70.6 kPa and 93.6 kPa confining pressures for silica powder. Elastic moduli values are $E=46\,836$ kPa at 70.6 kPa confining pressure and $E=111\,443$ kPa at 93.6 kPa confining pressure.

The material constants α_{DP} and k_{DP} involved in the expression of the yield condition (see equation 2.3) were determined by imposing that the experimental failure points corresponding to the confining pressures of 70.6 kPa and 93.6 kPa satisfy exactly the yield condition. The obtained numerical values are: $\alpha_{DP}=0.3197$; $k_{DP}=1.340$

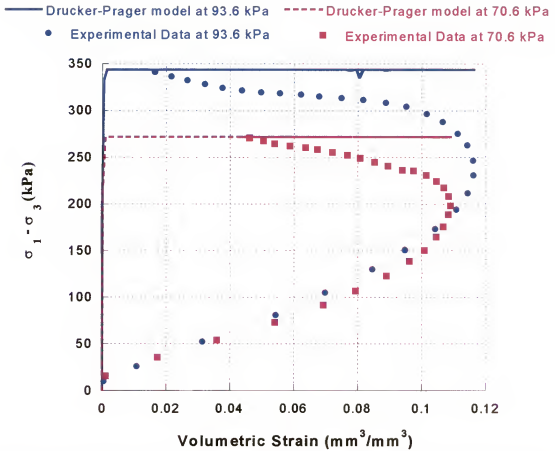


Figure 6.2: Comparison between Drucker-Prager predictions and experimental stress vs. volumetric strain at 70.6 kPa and 93.6 kPa confining pressures for silica powder. The simulations correspond to constant values of the bulk modulus: $K=46\,836$ kPa at 70.6 kPa confining pressure and $K=111\,443.43$ kPa at 93.6 kPa of confining pressure.

From Figure 6.1 it can be concluded that the Drucker-Prager model accurately described the influence of the confining pressure on failure, but overestimated the stresses prior to failure. Also, the model captured the effect of the confining pressure on strength. The higher the confining pressure, the higher the deviatoric stress level was at failure. However, the Drucker-Prager model could not predict the experimentally observed behavior prior to failure (see Figures 6.1 and 6.2). For example, the change in

the volumetric behavior (from compaction to dilation) could not be reproduced in perfect-plastic models because in such models the yield surface and the failure surface coincide.

The Drucker-Prager model was further applied to the polymeric pellets. For this system the values of the parameters are: $\alpha_{DP}=0.59$ and $k_{DP}=5.76$ (see Chapter 5).

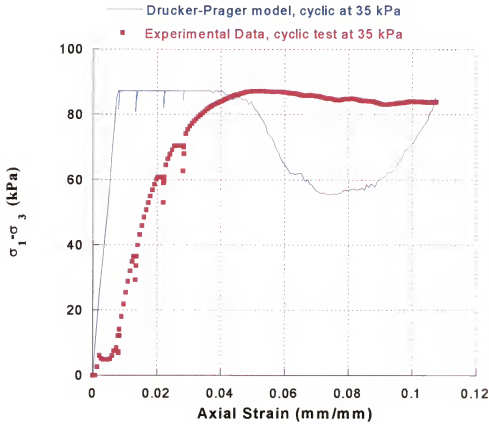


Figure 6.3: Comparison between Drucker-Prager predictions and experimental deviatoric stress vs. axial strain at 35 kPa of confining pressure for PE pellets. In the numerical simulations the elastic moduli were taken constant: $E=27555$ kPa.

Figures 6.3 and 6.4 show a comparison between model predictions and data at 35 kPa confining pressure.

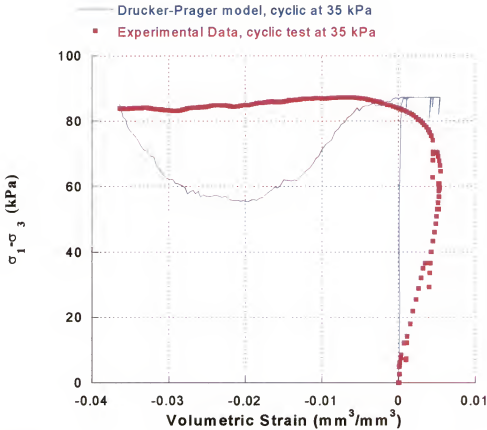


Figure 6.4: Comparison between Drucker-Prager model predictions and experimental deviatoric stress vs. volumetric strain at 35 kPa of confining pressure for PE pellets. In the numerical simulations: $E=27555$ kPa.

As was the case for silica powder, the theoretical predictions for PE pellets overestimate the experimental stresses. The maximum difference between the theoretical and experimental stresses was observed at the beginning of the strain history. The theoretical stresses are approximately 10 times the experimental ones for silica powder and about 8 times for PE pellets. Furthermore, compaction and dilation regimes could not be reproduced (see Figure 6.4). The effects of the confining pressure on strength were well reproduced by the model (see Figure 6.5).

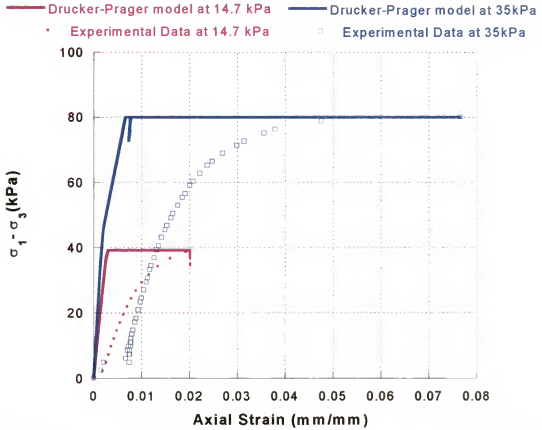


Figure 6.5: Comparison between Drucker-Prager simulation and experimental deviatoric stress vs. axial strain; for PE pellets. Effect on the confining pressure. Constant elastic moduli: $E=27555$ kPa.

6.3.5 Conclusions Concerning the Predictive Capabilities of Drucker-Prager Model

The Drucker-Prager model cannot reproduce irreversible deformation under hydrostatic conditions. Under deviatoric conditions, the stresses predicted by the model are much higher than the experimentally observed ones. Compaction and dilatation regimes cannot be differentiated using the Drucker-Prager model. The compressibility observed is simply elastic compressibility (see Figure 6.3). It is clear that the model describes only elastic behavior and failure (see Figures 6.3 and 6.4). Moreover, during unloading-reloading cycles where the material only exhibits elastic behavior, the model reproduces this feature correctly. There is a pronounced effect of confining pressure on

the stress path and failure as can be seen in Figure 6.5. The model correctly predicts the increase in strength due to an increase in confining pressure.

6.4 Closest Point Projection Algorithm and Convex Cutting Plane Algorithm Applied to Isotropic Hardening Models

To obtain the predictions of the Lade (1977) model for hydrostatic compression conditions, two isotropic hardening strain-driven algorithms namely *closest point projection* (CPP) algorithm and *convex cutting plane* (CCP), were implemented. Because the Lade (1977) model involves work hardening, a modification of the original CPP procedure (see Simo and Hughes 1998) was used. For silica powder, the Lade model predictions did not agree with data. Suspecting that this total lack of agreement between theory and data could be due to numerical errors, a second algorithm, called *convex cutting plane* (CCP) was implemented. The simulation results for silica powder using this algorithm were more satisfactory, so the CCP algorithm was used for simulation of the PE pellets data as well. The conclusion is that: the CCP algorithm is more appropriate for implementing Lade (1977) model than the CPP algorithm. The common characteristics and specific differences between the CPP and CCP algorithms are presented below.

D) Closest Point Projection Algorithm and Convex Cutting Plane Algorithm common characteristics

Assumed known:

- Elastic material parameters at initial state: K (bulk modulus) and G (shear modulus)
- Initial stress σ_n
- Initial total strain ε_n and plastic strain, ε_n^p
- Initial plastic work, Ψ_n

- Final total strain ε_{n+1}
- Yield function for isotropic compression (Lade 1977) (equation 3)

$$f(I_2, I_1, w_c) = I_1^2 + 2 \cdot I_2 - w_c, \text{ where}$$

- I_2 is the second invariant of the stress tensor
- I_1 is the trace of the stress tensor
- w_c is the hardening parameter.

Find:

- final stress σ_{n+1}
- final plastic strain, ε_{n+1}^p
- final plastic work Ψ_{n+1}
- final hardening parameter $w_{c(n+1)}$

Remarks:

For the implementation of the CPP and the CCP algorithm, $w_{c(n)}$, the hardening parameter at any strain step n , is chosen to be: $w_{c(n)} = p_a^2 \cdot \left(\frac{\Psi_n}{U \cdot p_a} \right)^{1/d}$, where Ψ_n is the total plastic work required to produce collapse strains at step n , U and d are experimentally determined constants, fixed for a given loading and p_a is the atmospheric pressure. Table 6.1 shows the differences and common steps in the development of the CPP and CCP algorithms.

Table 6.1 Differences and common steps in the CPP and the CCP algorithms

Closest Point Projection	Convex Cutting Plane
i) Initiate $k=0$, $\varepsilon_n^p = \varepsilon_{n+1}^p$, $\Psi_n^{(0)} = \Psi_{n+1}^{(0)} = \Psi_n^p$, $\Delta \lambda_{n+1}^{(0)} = 0$	Initiate $k=0$, $\varepsilon_{n+1}^p = \varepsilon_n^p$, $w_{n+1}^p = w_n^p$, $\Delta \lambda_{n+1}^{(0)} = 0$
ii) Compute C , the matrix of elastic moduli.	ii) Same
iii) Compute the trial elastic stress	iii) Same
iv) Compute the hardening parameter $w_{C(n+1)}^{(k)}$	iv) Same
v) Evaluate the flow rule law residuals, $\left(R_{n+1}^{(k)}\right)^T$.	v) None
vi) Is $(f_{n+1}^{(k)} \leq TOL_1$ and $\ R_{n+1}^{(k)}\ \leq TOL_2)$ true? If yes, END. Else	vi) Is $f_{n+1}^{(k)} \leq TOL$; Yes, END. Else
vii) Compute the plastic moduli, D	vii) Same
viii) Compute the consistent tangent moduli as: $\left[A_{n+1}^{(k)}\right]^{-1}$.	viii) Compute the value of the hardening moduli
ix) Obtain $\Delta^2 \lambda_{n+1}^{(k)}$ as $\Delta^2 \lambda_{n+1}^{(k)} (R_{n+1}^{(k)}, A_{n+1}, \partial \partial \sigma f_{n+1})$	ix) Obtain $\Delta^2 \lambda_{n+1}^{(k)}$ as $\Delta^2 \lambda_{n+1}^{(k)} (C_{n+1}^{-1}, \partial \sigma f_{n+1}, h_{n+1})$
x) Update ε_{n+1}^p , $\Delta \lambda_{n+1}^{(k+1)}$, $\Psi_{n+1}^{(k+1)}$ and go to step ii).	x) Update ε_{n+1}^p , $\Delta \lambda_{n+1}^{(k+1)}$, $w_{n+1}^{(k+1)}$ and go to step ii).

II) Closest Point Projection: Specific Characteristics

- It is an application of the Newton's method to the system of equations formed by the flow rule, the hardening law and the complementarity condition.
- It is an implicit procedure that involves solving a 6x6 system of equations.
- Normality is enforced at the final (unknown) iterate.
- It needs the gradients of the flow rule and hardening law, which for complicated plasticity models might be laborious to compute.

Steps:

1. Initialize the iteration counter step $k=0$.
2. Initialize the plastic strain $\mathcal{E}_{n+1}^{p(0)} := \mathcal{E}_n^p$, the plastic work $\Psi_{n+1}^{(0)} := \Psi_n$ and plastic consistency parameter $\Delta\lambda_{n+1}^{(0)} := 0$.
3. Compute \mathbf{C} , the matrix of elastic moduli, possibly depending on the initial stress σ_n through its invariants. Note that in the numerical implementation used, \mathbf{C} is considered constant during each load step. \mathbf{C} is updated between load steps, considering a power law variation for K .
4. While $k < k_{max}$ repeat steps 5-18.
5. Compute the trial elastic stress $\sigma_{n+1}^{(k)} = \mathbf{C} : (\mathcal{E}_{n+1} - \mathcal{E}_{n+1}^{p(k)})$.
6. Compute $[I_1^{(k)} I_2^{(k)} I_3^{(k)}]$ the invariants of the trial elastic stress tensor $\sigma_{n+1}^{(k)}$.
7. Compute the hardening parameter $w_{c(n+1)}^{(k)}$ as

$$w_{c(n+1)}^{(k)} = p_a^2 \cdot \left(\frac{\Psi_{n+1}^{(k)} - \Psi_n}{U \cdot p_a} \right)^{1/d}$$

8. Check the yield condition

$$f_{n+1}^{(k)} = f(\sigma_{n+1}^{(k)}, w_{c(n+1)}^{(k)}) := I_1^{2(k)} + 2 \cdot I_2^{(k)} - w_{c(n+1)}^{(k)} \leq \text{TOL}_1 ?$$

The condition verifies that $\sigma_{n+1}^{(k)}$ is on or under the yield surface of hardening parameter $w_{c(n+1)}^{(k)}$ and TOL_I is a tolerance, accounting for rounding errors.

9. Evaluate the flow rule law residuals as:

$$\left(R_{n+1}^{(k)}\right)^T = \left\{ \begin{array}{c} -\varepsilon_{n+1}^p{}^{(k)} + \varepsilon_n^p \\ -\Psi_{n+1}^p{}^{(k)} + \Psi_n^p \end{array} \right\} + \Delta\lambda_{n+1}^{(k)} \left\{ \begin{array}{c} \frac{\partial f_{n+1}}{\partial \sigma} \\ \frac{\partial f_{n+1}}{\partial w_c} \end{array} \right\}^{(k)}.$$

(See Appendix E for the computation of the derivatives).

10. Is $(f_{n+1}^{(k)} \leq TOL_1 \text{ and } \|R_{n+1}\|^{(k)} \leq TOL_2)$ true?

Here $\|A\|^2 = \text{tr}(A^T A)$, where A^T denotes the transposed of vector or matrix A.

11. If YES, the final new stress is the elastic trial stresses. END AND EXIT.

12. If NOT, plastic correction is needed, as follows:

13. Compute the plastic moduli, D as

$$D_{n+1}^{(k)} = \frac{\partial w_{c(n+1)}^{(k)}}{\partial \Psi_{n+1}^{(k)}} = \frac{1}{d} \cdot \left(\frac{1}{U}\right)^{\frac{1}{d}} \left(\frac{\Psi_{n+1}^{(k)} - \Psi_n}{p_a}\right)^{\frac{1}{d}-1}$$

14. Compute the consistent tangent moduli as:

$$\left[A_{n+1}^{(k)}\right]^{-1} = \begin{bmatrix} C^{-1} + \Delta\lambda_{n+1} \partial^2_{\sigma\sigma} f_{n+1} & \Delta\lambda_{n+1} \partial^2_{\sigma w_c} f_{n+1} \\ \Delta\lambda_{n+1} \partial^2_{w_c \sigma} f_{n+1} & D_{n+1}^{-1} + \Delta\lambda_{n+1} \partial^2_{w_c w_c} f_{n+1} \end{bmatrix}^{(k)}$$

(See Appendix E for the expressions of the derivatives)

15. Obtain increments to consistency parameter

$$\Delta^2 \lambda_{n+1}^{(k)} = \frac{f_{n+1}^{(k)} - \left[\frac{\partial f_{n+1}}{\partial w_c} \frac{\partial f_{n+1}}{\partial w_c} \right] A_{n+1}^{(k)} R_{n+1}^{(k)}}{\left[\frac{\partial f_{n+1}}{\partial \sigma} \frac{\partial f_{n+1}}{\partial w_c} \right] A_{n+1}^{(k)} \left[\frac{\partial f_{n+1}}{\partial \sigma} \frac{\partial f_{n+1}}{\partial w_c} \right]^T}$$

16. Compute the incremental plastic strains and internal variables

$$\begin{Bmatrix} \Delta \varepsilon_{n+1}^{p(k)} \\ \Delta \Psi_{n+1}^{(k)} \end{Bmatrix} = \begin{bmatrix} C^{-1} & 0 \\ 0 & D_{n+1}^{-1} \end{bmatrix}^{(k)} A_{n+1}^{(k)} \left[R_{n+1}^{(k)} + \Delta^2 \lambda_{n+1}^{(k)} \begin{Bmatrix} \frac{\partial f_{n+1}}{\partial \sigma} \\ \frac{\partial f_{n+1}}{\partial w_c} \end{Bmatrix}^{(k)} \right]$$

A simplified form is used for the product of the first 2 matrices (called in program 'product_tangent_moduli'), due to the block form of both the first term of the product and of A_{n+1} .

17. Update plastic strain, consistency parameter and state variables:

$$\begin{aligned} \varepsilon_{n+1}^{p(k+1)} &= \varepsilon_{n+1}^{p(k)} + \Delta \varepsilon_{n+1}^{p(k)} \\ \Delta \lambda_{n+1}^{(k+1)} &= \Delta \lambda_{n+1}^{(k)} + \Delta^2 \lambda_{n+1}^{(k)} \\ \Psi_{n+1}^{(k+1)} &= \Psi_{n+1}^{(k)} + \Delta \Psi_{n+1}^{(k)} \end{aligned}$$

18. Update iteration counter $k=k+1$ and return to step 4.

III) Convex Cutting-Plane: Specific Characteristics

- It is an explicit procedure that involves only functional evaluations.
- Normality is enforced at the initial (known) iterate.
- Does not need the gradients of the flow rule and hardening law.

Steps:

1. Initialize the iteration counter step $k=0$.
2. Initialize the plastic strain $\varepsilon_{n+1}^{p(0)} := \varepsilon_n^p$, the plastic work $\Psi_{n+1}^{(0)} := \Psi_n$ and plastic consistency parameter $\Delta \lambda_{n+1}^{(0)} := 0$.
3. Compute C , the matrix of elastic moduli, possibly depending on the initial stress σ_n through its invariants. C is considered constant during each load step and it is updated between load steps, considering a power law variation for K .

4. While $k < k_{max}$ repeat steps 5-17.

5. Compute the trial elastic stress $\sigma_{n+1}^{(k)} = C : (\varepsilon_{n+1} - \varepsilon_{n+1}^p{}^{(k)})$.

6. Compute $[I_1^{(k)} I_2^{(k)} I_3^{(k)}]$ the invariants of the trial elastic stress tensor $\sigma_{n+1}^{(k)}$.

7. Compute the hardening parameter $w_{c(n+1)}^{(k)}$ as:

$$w_{c(n+1)}^{(k)} = p_a^2 \cdot \left(\frac{\Psi_{n+1}^{(k)} - \Psi_n}{U \cdot p_a} \right)^{1/d}.$$

8. Compute the plastic moduli, $D_{n+1}^{(k)}$ as

$$D_{n+1}^{(k)} = \frac{\partial w_{c(n+1)}^{(k)}}{\partial \Psi_{n+1}^{(k)}} = \frac{1}{d} \cdot \left(\frac{1}{U} \right)^{\frac{1}{d}} \left(\frac{\Psi_{n+1}^{(k)} - \Psi_n}{p_a} \right)^{\frac{1}{d}-1}.$$

9. Compute the value of the hardening moduli

$$h_{n+1}^{(k)} = h(\sigma_{n+1}^{(k)}, w_c^{(k)}) := D_{n+1}^{(k)} \frac{\partial f}{\partial w_c}(\sigma_{n+1}^{(k)}, w_c^{(k)}) = -D_{n+1}^{(k)} \frac{\partial f_{n+1}}{\partial w_c} = -D_{n+1}^{(k)}.$$

10. Compute the yield condition $f_{n+1}^{(k)} = f(\sigma_{n+1}^{(k)}, w_{c(n+1)}^{(k)}) := I_1^{2(k)} + 2 \cdot I_2^{(k)} - w_{c(n+1)}^{(k)}$.

11. Is $f_{n+1}^{(k)} \leq TOL_f$ true?

The condition verifies that $\sigma_{n+1}^{(k)}$ is on or under the yield surface of hardening parameter $w_{c(n+1)}^{(k)}$ and TOL_f is a tolerance, accounting for rounding errors.

If YES, the final new stress is the elastic trial stresses. END AND EXIT.

If NOT, plastic correction is needed, as follows:

12. Obtain increments to plastic consistency parameter

$$\Delta^2 \lambda_{n+1}^{(k)} = \frac{f_{n+1}^{(k)}}{\left(\frac{\partial f_{n+1}^{(k)}}{\partial \sigma} \right)^T C_{n+1} \frac{\partial f_{n+1}^{(k)}}{\partial \sigma} + \frac{\partial f_{n+1}^{(k)}}{\partial w_c} h_{n+1}^{(k)}}$$

(See Appendix E for the expressions of the derivatives)

13. Update plastic strain, consistency parameter and state variable:

$$\varepsilon_{n+1}^p{}^{(k+1)} = \varepsilon_{n+1}^p{}^{(k)} + \Delta^2 \lambda_{n+1}^{(k)} \frac{\partial f_{n+1}^{(k)}}{\partial \sigma}$$

$$\Delta \lambda_{n+1}^{(k+1)} = \Delta \lambda_{n+1}^{(k)} + \Delta^2 \lambda_{n+1}^{(k)}$$

$$w_{c(n+1)}^{(k+1)} = w_{c(n+1)}^{(k)} - \Delta^2 \lambda_{n+1}^{(k)} h_{n+1}^{(k)}$$

14. Update iteration counter $k=k+1$ and return to step 4.

6.4.1 Theoretical Predictions using Lade Model for Silica Powder Subjected to Hydrostatic Compression

The *Closest Point Projection* (CPP) and the *Convex Cutting Plane* (CCP) algorithms were both implemented in MatLab. The comparison between the theoretical predictions using the CPP algorithm and data is shown in Figure 6.6. The material and hardening constants used as input are listed in Table 6.2. The plastic strains are grossly overestimated while the elastic strains are grossly underestimated, hence the predicted stresses are three orders of magnitude smaller than the experimental ones. Note that the elastic stresses are underestimated and the plastic stresses overestimated, hence not allowing the plastic corrector step to take place.

Table 6.2: Material and hardening constants for Lade's parameters of silica powder used in the hydrostatic numerical simulations.

	Fitting Parameters of silica for Lade model (power law for elastic parameters)	Fitting Parameters of silica for Lade Model (exponential law for elastic parameters) (equation 4.8)
Elastic Regime	$K_{ur}=796.91$ $n_{ur}=0.78080$ <i>Poisson Ratio</i> (ν)= 0.31	$K_{\infty} = 2.5 \cdot 10^5$ $\psi = -1.399 \cdot 10^5$ $\beta = 1.21 \cdot 10^{-3}$. <i>Poisson Ratio</i> (ν)= 0.31
Compressive Plastic Regime	$U=0.0122$, $d=0.913$ or $U=0.0122$, $d=1$ (See section 4.7.1 for discussion)	$U=0.0122$ $d=0.913$

The comparison between the theoretical predictions obtained using the CCP algorithm and the same values of the model parameters as input, and data is shown in Figure 6.7. Theoretical stresses are 3 orders of magnitude higher than the experimental ones.

Note that the simulation results using the CCP algorithm (Figure 6.8) show two regions.

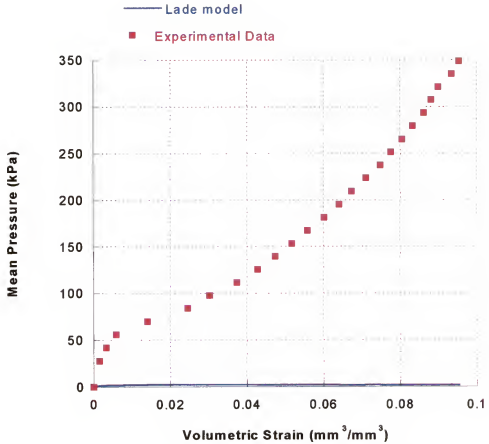


Figure 6.6: Comparison between simulated and experimental hydrostatic data. Simulation results were obtained using the *CPP* algorithm and power law variation for elastic parameters (Lade 1977) ($K_{ur}=796.91$, $n_{ur}=0.78080$, $U=0.0122$, $d=0.913$).

In the first region, which represents one third of the total strain history, the simulation results underestimated the magnitude of the values of experimental stresses (approximately four times). In the second region, the simulation results were overestimated. The maximum simulated stress was approximately 3.5 times the experimental stress. The change corresponds roughly to the value of the volumetric strain when the experimental curve changes from concave to convex.

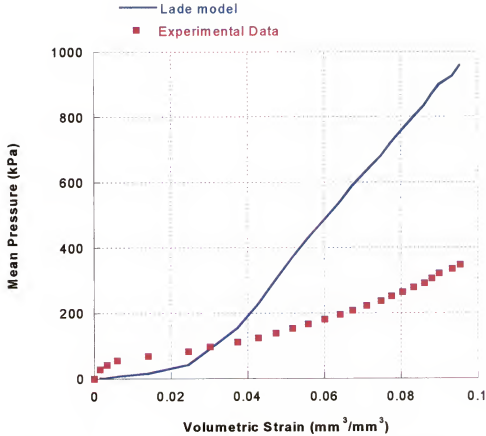


Figure 6.7: Comparison between simulation and experimental hydrostatic data. Simulation results were obtained using the *Cutting Plane* algorithm and power law variation for elastic parameters (Lade 1977) ($K_{ur}=796.91$, $n_{ur}=0.78080$, $U=0.0122$, $d=0.913$).

In conclusion, to reduce the numerical errors, the CCP algorithm should be used for integration of Lade model for hydrostatic conditions. One of the factors that could have affected the accuracy of simulation results using CPP is the fact that in the Lade model the hardening law is represented by a power function. An initial error in the computation of the flow rule gradient can deteriorate the convergence of the CPP algorithm, while the CCP algorithm avoids this computation and as such generates fewer errors.

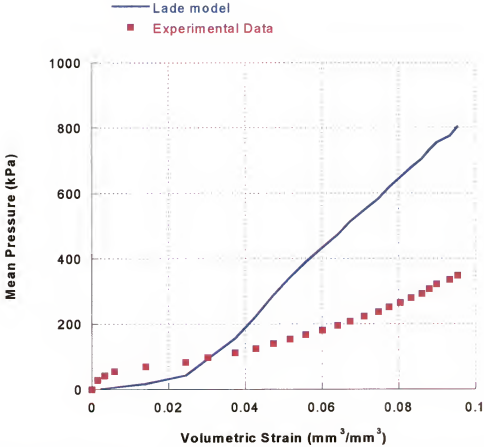


Figure 6.8: Mean stress vs. volumetric strain. Simulated data were obtained using the Cutting plane algorithm, silica's fit for elastic and hardening constants and exponential law variation for elastic parameters ($K_{\infty} = 2.5 \cdot 10^5$, $\psi = -1.399 \cdot 10^5$, $\beta = 1.21 \cdot 10^{-3}$, $U = 0.0122$, $d = 0.913$).

Note that at the beginning of the strain history, the theoretical curve is convex towards the stress axis, while the experimental one is convex. This difference can be attributed to errors in updating the elastic constants and as such, the simulations were repeated using an exponential law variation for the elastic constants (see equation 4.8). The accuracy of the simulations results presented in Figure 6.8 is improved, but is not yet satisfactory. The maximum discrepancy appears at the highest hydrostatic stress applied to the material where the plastic deformations are larger than the elastic ones. Since the hydrostatic plastic response, is characterized by the hardening law

$W = U \cdot p_a \left(\frac{f_c}{p_a} \right)^{\frac{1}{d}}$ (equation 4.16), d and U , the parameters involve in the formulation of

the law are extremely important for the correct formulation of the model. It was noted in section 4.7.1 that for small changes in d , U kept constant, which means that d has a stronger influence in the hardening law function than U . Therefore, a parametric study on d was performed (see Appendix E for details) concluding that $d=1$ and $U=0.0122$ showed a better approximation that $d=0.913$ and $U=0.0122$ (see also Figure 6.9). Further discussions of the results were based on the simulations obtained with $d=1$, $U=0.0122$.

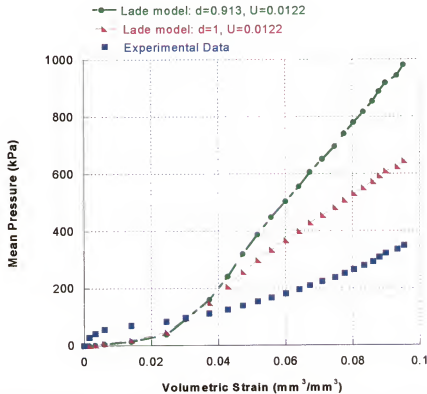


Figure 6.9: Mean stress vs. volumetric strain. Cutting plane algorithm. Silica's fit for elastic and hardening constants ($K_{\infty} = 2.5 \cdot 10^5$, $\psi = -1.399 \cdot 10^5$, $\beta = 1.21 \cdot 10^{-3}$, $U=0.0122$, $d=0.913$ and 1). Effects of hardening constant (d) on silica powder simulation.

6.4.2 Numerical Simulations Results of Hydrostatic Test on Polymer Pellets

Because for the silica powder, the convex cutting plane (CCP) algorithm gave better results than the closest point projection (CPP) one, it was also used to reproduce the polymer (PE pellets) behavior in hydrostatic compression. A constant value for the elastic parameter ($K=17975\text{kPa}$) was considered, as the fitting procedure described in section 5.5 concluded that a constant value is more adequate than an exponential function.

In Figure 6.10 can be observed that the polymer system shows elastic behavior during the isotropic compression test, thus the simulation data (squares) predict exactly the experimental observations.

6.4.3 Conclusions for Hydrostatic Test on Silica Powder and PE Pellets

Two different algorithms were implemented to reproduce the behavior of silica powder. Also, a parametric study on elastic and hardening constants was done on silica powder. For silica powder, the best simulation results were obtained when the convex cutting plane (CCP) algorithm was used with an exponential type of law for K (bulk modulus) and hardening constant $d=1$.

Because the CCP algorithm showed a better approximation of the experimental results for silica than the CPP, the same algorithm was used for polymer pellets and very good accuracy was obtained. Comparing the two systems, the simulation results for silica are in less agreement with the experiments than the results for PE pellets.

Silica powder has a very low cohesion, hence it is very difficult to achieve closed packing density in the pre-compaction phase prior to the test. Hence, the initial non-linearity in the response (up to 0.01 strains), which corresponds to particle rearrangements.

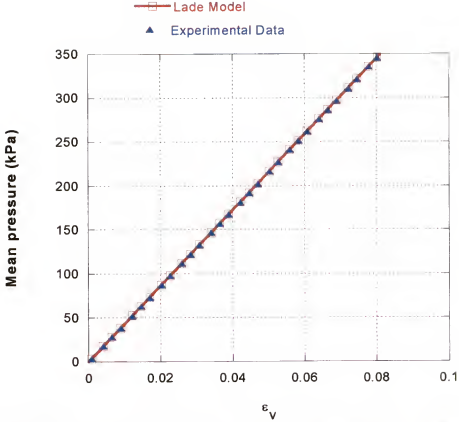


Figure 6.10: Mean stress vs. volumetric strain. Hydrostatic experiment on PE pellets. The simulation data were obtained using the CCP algorithm and constant elastic moduli.

For polymer pellets, good pre-compaction was achieved, hence the measurements reflect the compaction response of the system, which is purely elastic. To conclude, the CCP algorithm applied to the integration of Lade model (1977) for hydrostatic conditions is very robust and computationally efficient. In the following section, we check the ability of Lade model to reproduce the behavior of the two systems studied under deviatoric conditions.

6.5 Convex Cutting Plane Algorithm Applied to Deviatoric Hardening Lade Model

For deviatoric conditions, the yield function and the hardening parameter (Lade 1977) are:

- $f_n(I_3, I_1, w_n) = \left(\frac{I_1^3}{I_3} - 27 \right) \cdot \left(\frac{I_1}{p_a} \right)^m - w_n$, where I_3 is the third invariant of the stress tensor, I_1 is the trace of the stress tensor, m is a material parameter and w_n is the hardening parameter at strain step n .
- Hardening parameter, $w_n = H \cdot e^{-B \cdot \Psi_n} \cdot \left(\frac{\Psi_n}{p_a} \right)^{1/z}$, where Ψ_n is the total plastic work required to produce expansive strains at step n , H , B and z are experimentally determined constants which depend on the confining pressure, and p_a the atmospheric pressure. The variation of H , B and z with pressure is given by: $H = \eta_1 \cdot \left(\frac{e \cdot p_a}{W_{ppeak}} \right)^{\frac{1}{z}}$,
 $B = \frac{1}{z \cdot W_{ppeak}}$, $W_{ppeak} = P \cdot p_a \cdot \left(\frac{\sigma_3}{p_a} \right)^L$ and $z = \kappa + \xi \cdot \left(\frac{\sigma_3}{p_a} \right)$, where P , z , L , κ and ξ are material constants determined from experiments.

The procedure steps used in this section were the same as the ones used in section 6.4 for the convex cutting plane (CCP). However, since the expressions of the yield function and of hardening parameter are different under deviatoric test conditions than under hydrostatic test, steps: 7, 8, 9, 10 and 12 in section 6.4 were updated as follows:

- Hardening parameter, $w_{n+1}^{(k)}$

$$w_{n+1} = H \cdot e^{-B \cdot \Psi_n} \cdot \left(\frac{\Psi_{n+1} - \Psi_n}{p_a} \right)^{1/z}.$$

- Plastic moduli, $D_{n+1}^{(k)}$

$$D_{n+1}^{(k)} = H \cdot e^{-B \cdot \Psi_{n+1}} \cdot \left[-B \cdot \left(\frac{\Psi_{n+1}}{p_a} \right)^{\frac{1}{z}} + \frac{1}{z} \cdot \left(\frac{1}{p_a} \right)^{\frac{1}{z}} \cdot \Psi_{n+1}^{\frac{1}{z}-1} \right]$$

- Value of the hardening moduli, $h_{n+1}^{(k)}$

$$h_{n+1}^{(k)} = h(\sigma_{n+1}^{(k)}, w_{n+1}^{(k)}) := D_{n+1}^{(k)} \frac{\partial f}{\partial h}(\sigma_{n+1}^{(k)}, w_{n+1}^{(k)}) = D_{n+1}^{(k)} \frac{\partial f_{n+1}}{\partial w} = -D_{n+1}^{(k)}.$$

- Yield condition, $f_{n+1}^{(k)}$

$$f_{n+1}^{(k)} = f(\sigma_{n+1}^{(k)}, w_{n+1}^{(k)}) := \left(\frac{I_1^{(k)}}{I_3^{(k)}} - 27 \right) \cdot \frac{I_1^{(k)}}{p_a} - w_{n+1}^{(k)}$$

- Increments to plastic consistency parameter, $\Delta^2 \lambda_{n+1}^{(k)}$

$$\Delta^2 \lambda_{n+1}^{(k)} = \frac{f_{n+1}^{(k)}}{\left(\frac{\partial f_{n+1}^{(k)}}{\partial \sigma} \right)^T C \frac{\partial f_{n+1}^{(k)}}{\partial \sigma} + \frac{\partial f_{n+1}^{(k)}}{\partial w} h_{n+1}^{(k)}}$$

(see Appendix D for the computation of the derivatives $\frac{\partial f}{\partial \sigma}$ and $\frac{\partial f}{\partial w}$).

6.5.1 Numerical Simulation Results of Deviatoric Tests on Silica Powder

Experimental strain histories for two different systems, silica powder and PE pellets, were used as input. The material parameters and the numerical values used in the simulations are summarized in Table 6.3

Table 6.3: Plastic constants and hardening constants for silica powder and PE pellets to used as input in the deviatoric numerical simulations.

Silica Powder Plastic Parameters	PE Pellets Plastic Parameters
$\eta_1=52.48$	$\eta_1=21.4$
$L=0.4$	$L=1$
$P=-1.04$	$P=-1.02$
$\kappa=0.384$	$\kappa=0.14$
$\xi=-0.04$	$\xi=-0.44$

The algorithm was run considering the matrix of elastic coefficients dependent on the mean stress, i.e., $K = K_{\infty} + \psi \cdot e^{\frac{-\beta(\sigma_1 + 2\sigma_3)}{p_a}}$ with: $K_{\infty} = 2.5 \cdot 10^5$, $\psi = -1.399 \cdot 10^5$ and $\beta = 1.21 \cdot 10^{-3}$. The Poisson coefficient is $\nu = 0.31$. Figure 6.11 illustrates the simulation results in comparison with data. Note that the theory reproduces well the compressibility/dilatancy of the material (see Figure 6.12).

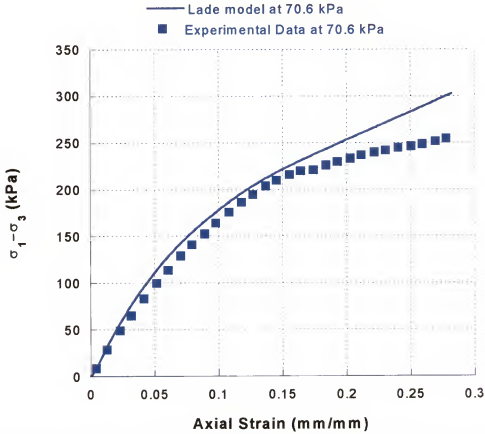


Figure 6.11: Simulated and experimental deviatoric stress vs. axial strain at 70.6 kPa for silica powder. Variable elastic parameters, $K = K_{\infty} + \psi \cdot e^{\frac{-\beta(\sigma_1 + 2\sigma_3)}{p_a}}$, $K_{\infty} = 2.5 \cdot 10^5$, $\psi = -1.399 \cdot 10^5$ and $\beta = 1.21 \cdot 10^{-3}$.

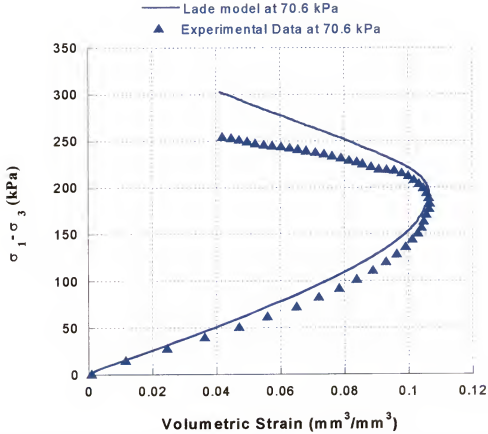


Figure 6.12: Simulated and experimental deviatoric stress vs. volumetric strain at 70.6 kPa for silica powder. Variable elastic parameter, $K = K_{\infty} + \psi \cdot e^{-\beta \frac{I_1}{p_{ref}}}$, $K_{\infty} = 2.5 \cdot 10^5$, $\psi = -1.399 \cdot 10^5$ and $\beta = 1.21 \cdot 10^{-3}$.

The measured and predicted stress-strain behavior for silica powder for two different confining pressures is illustrated in Figure 6.13. Note that the effect of confining pressure on the overall behavior is well reproduced. The maximum difference between measured and predicted deviatoric stresses was recorded at failure

The general trend of the experimental deviatoric stress-axial strain curve was well captured by the model.

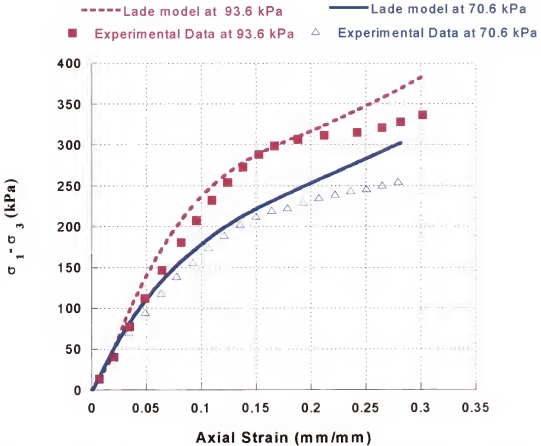


Figure 6.13: Simulated and experimental deviatoric stress vs. axial strain. Comparison on simulation results at 70.6 and 93.6 kPa of confining pressures for silica powder, exponential variation of the elastic parameters with the mean stress was considered.

Although the predicted stresses overestimate the experimental values with the error being higher in the dilation regime, and with a maximum error obtained at failure, the accuracy is within the experimental error. The same conclusions can be drawn by comparing the theoretical and experimental deviatoric stress- volumetric strain curve (see Figure 6.14). The model reproduces particularly well the change in deformation mechanism with increasing applied deviatoric stress. Note that the model captures the effect of confining pressure on the threshold value corresponding to the passage from

compressive to dilatation regime: the higher the confining pressure, the higher is the stress level at which this transition occurs.

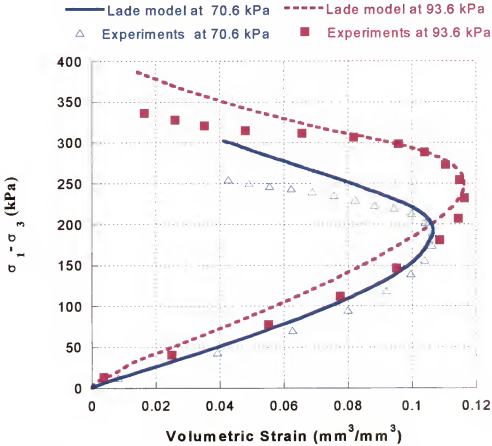


Figure 6.14: Simulated and experimental deviatoric stress vs. volumetric strain at 70.6 and 93.6 kPa of confining pressures for silica powder; an exponential variation of the elastic parameters with mean stress was considered in the simulations.

In order to illustrate the predictive capabilities of the model as well as to evaluate the stability of the simulation algorithm, numerical simulations were also run at confining pressures for which experimental data were not available. At a given confining pressure, the simulations were stopped when the theoretical stress level at failure was reached.

Figures 6.15 and 6.16 show the theoretical predictions corresponding to confining

pressures in the range 40 kPa to 200 kPa. It is clearly seen that the model can be successfully used to provide valuable information concerning the deformation and failure behavior.

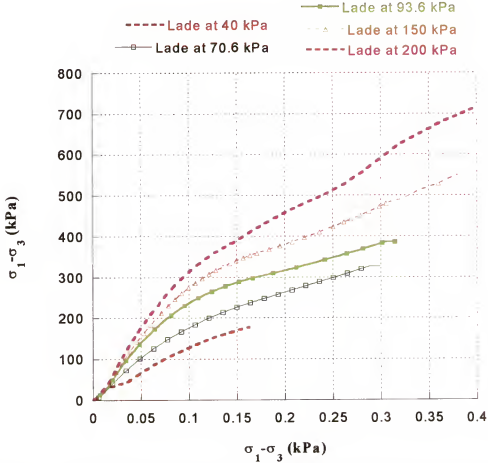


Figure 6.15: Simulated deviatoric stress vs. axial strain. Simulation results at 40, 70.6, 93.6, 150 and 200 kPa of confining pressure, using exponential variation for the elastic parameters.

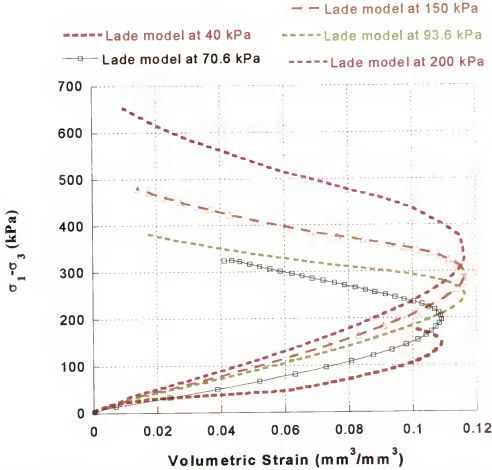


Figure 6.16: Deviatoric stress vs. volumetric strain. Simulation results at 40, 70.6, 93.6, 150 and 200 kPa of confining pressure, using exponential variation for the elastic parameters.

6.5.2 Numerical Simulation of the Behavior of PE Pellets under Deviatoric Test Conditions

The convex cutting plane (CCP) algorithm was implemented in order to reproduce the PE pellets deviatoric compaction behavior. For this system, the Bulk modulus is constant and has a value of $1.7 \cdot 10^4$ kPa (see Chapter 5). The numerical values of the parameters involved in the model are listed in Table 6.2.

Figures 6.17 and 6.18 show a very good agreement between the simulation results and the experimental data at 14.7 kPa of confining pressure.

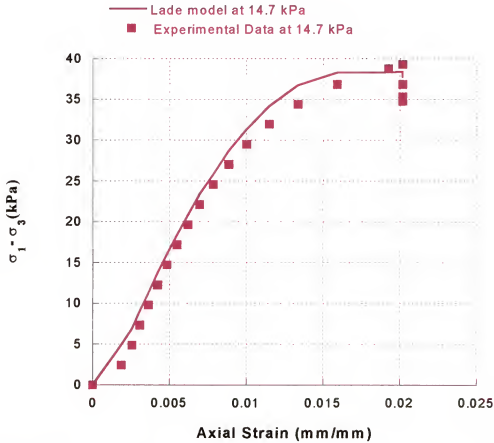


Figure 6.17: Simulated and experimental deviatoric stress vs. axial strain at 14.7 kPa of confining pressure. Simulation data obtained using the CCP algorithm and constant elastic moduli, $K=1.7 \cdot 10^4$ kPa.

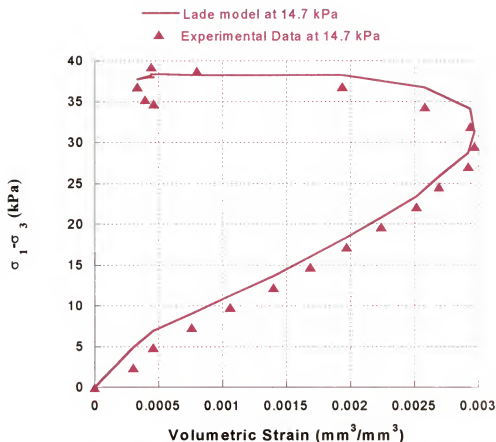


Figure 6.18: Simulated and experimental deviatoric stress vs. volumetric strain for PE pellets. at 14.7 kPa of confining pressure. Simulation data obtained using the CCP algorithm and constant elastic moduli, $K=1.7 \cdot 10^4$ kPa.

In Figures 6.19 and 6.20 are plotted the model predictions and data corresponding to 14.7 and 35 kPa. The effect of the confining pressure on the behavior of PE pellets is well described by the theory.

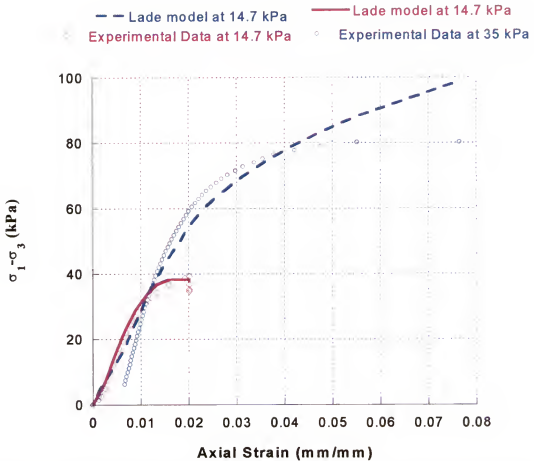


Figure 6.19: Simulated and experimental deviatoric stress vs. axial strain at 14.7 and 35 kPa of confining pressure for PE pellets. Effect of the confining pressure. Simulation data obtained using the CCP algorithm and constant elastic moduli, $K=1.7 \cdot 10^4$ kPa.

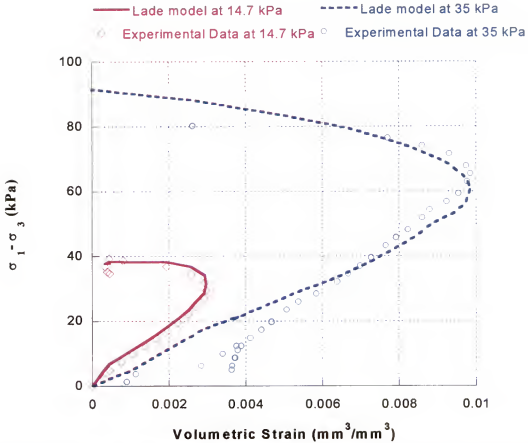


Figure 6.20: Simulated and experimental deviatoric stress vs. volumetric strain at 14.7 and 35 kPa of confining pressure for PE pellets. Simulation data obtained using the CCP algorithm and constant elastic moduli, $K=1.7 \cdot 10^4$ kPa.

Furthermore, in order to investigate the ability of the model to simulate the behavior of the system at high confining pressures, the simulations were also performed at 90, 150, and 200 kPa of confining pressures. Because measured strain history was not available for these confining pressures, the simulation was stopped when the theoretical failure stress corresponding to the given confining pressure was reached. Figure 6.21 shows that the model is able to predict the deformation and failure of the material.

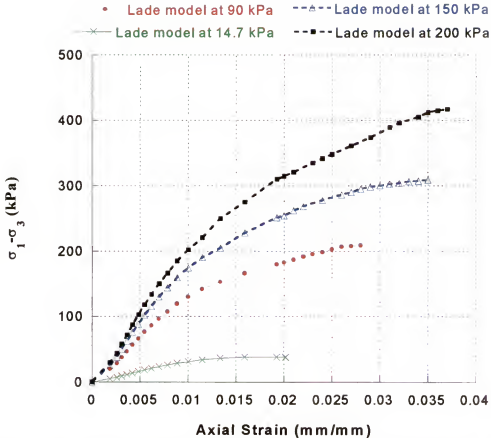


Figure 6.21: Simulated deviatoric stress vs. axial strain for PE pellets at 14.7, 90, 150 and 200 kPa of confining pressure. Simulation data obtained using the CCP algorithm and constant elastic moduli, $K=1.7 \cdot 10^4$ kPa.

6.5.3 Conclusions for Deviatoric Tests on Silica Powder and Polymer Pellets

The convex cutting plane (CCP) algorithm was used to integrate the model and the simulation results were compared to experimental data. For both systems, the simulation results were in good agreement with the experimental results, showing that the model is able to describe very well all the features of the behavior of these systems. Specifically, the model captures very well the observed increase in: (1) the level of the dilatancy and (2) the increase of the failure stress with applied confining pressure.

6.6 Conclusions

Predictive capabilities of Drucker-Prager model: Drucker-Prager model is an elastic perfect plastic model. Hence, such a model could not account for any change in deformation mechanisms. Use of this model for industrial applications, should be limited to situations in which only the elastic behavior and failure characteristics are of interest. Drucker-Prager model cannot be used to reproduce irreversible deformation under hydrostatic conditions.

Predictive Capabilities of Lade model: The model matched reasonably well the data for silica powder and PE pellets under hydrostatic conditions. The theoretical predictions for deviatoric stress conditions were also in very good agreement with the experimental results. The model accounts for the change in volumetric deformation mechanisms with the increase of the applied deviatoric stress. The model reproduces very well the observed transition from compaction to dilation. The increase in the value of the dilatancy threshold level with increasing confining pressure was particularly well described. The accuracy of the theoretical predictions is within the scatter of natural data. This model can be successfully used to predict the behavior of polymeric pellets and hence applied to practical simulations.

CHAPTER 7

CONCLUSIONS

Almost every industry handles powders/bulk solids, either as raw materials or as final products (chemicals, foods, ceramics, minerals, etc). However, the understanding of powder behavior as well as the amount of information on material properties is limited. Generally, the material properties are determined based on shear test measurements, yet in order to predict the bulk mechanical response during storage and transport, experimental data corresponding to a variety of deformation, loading conditions, and shear rates are needed. A simple, yet accurate test is the triaxial compression test. In the triaxial compression test measurements of both axial and volumetric strains undergone by the material can be done thus, allowing the characterization of the stress and strain under 3-D conditions.

The main goal of this dissertation was to investigate the mechanical behavior of silica powder using a triaxial tester and use or develop a constitutive model capable to predict the observed behavior. To achieve this goal, first a series of triaxial tests were conducted at different confining pressures for silica powder. To identify and characterize the properties of silica, first a series of monotonic triaxial compression tests were performed at confining pressures in the range 27 kPa to 350 kPa. In an effort to better monitor and characterize stress history effects on the irreversibility of the material behavior, cyclic tests at the same confining pressures were performed. The stress-strain response was strongly non-linear, even in the elastic regime. A progressive departure

from elastic behavior with increasing applied differential stress was observed. For all confining pressures, the experimental stress-volumetric strain curves showed both a compaction regime (volume decrease) and a dilatant regime (irreversible volume increase). Short-term creep and relaxation tests have also been performed, showing that the material exhibits time effects. Based on the experimental results, it can be concluded that the inviscid material behavior is elastic/plastic.

The current practice, in powder technology is to use elastic/perfect plastic models to predict the behavior of a given system. One of the objectives of this dissertation was to examine whether an elastic/perfectly plastic model could indeed predict the observed behavior. The Drucker-Prager model, a representative elastic/plastic model was applied to silica. The determination of the parameters of this model was done using the triaxial test data. Numerical integration of this model using the closest point projection (CPP) algorithm was done. The robustness of this algorithm was demonstrated. Comparisons between the Drucker-Prager model and experimental data show that the predictive capabilities of this model are limited to elastic compressibility and failure characteristics. Irrecoverable compressibility under hydrostatic pressure cannot be predicted with this theory. The simulation results show clearly that a good agreement with data can be obtained only if the effect of the accumulated plastic deformation on the behavior is taken into account.

A literature review of elastic-plastic models that incorporate hardening stress-strain theories was performed. The most widely used stress-strain theories are the Cambridge School theories (Cam-clay theories). However, such theories predict only volumetric compressibility, whereas laboratory tests on silica show that the volumetric

strain behavior gradually changes from compressive to expansive (or dilatant) with increasing deviatoric stress. Existing cap-type theories that could model dilatant behavior have poor predictive capabilities to describe irrecoverable strains, which occur during hydrostatic compression and thus cannot predict the existence of both regimes of volumetric deformation under deviatoric conditions. A general stress-strain theory, which could describe: (1) the change in deformation mechanism due to change in loading history; (2) the effect of all stress invariants on the overall behavior was developed by P.V. Lade (see Lade (1977)). It was thus decided to evaluate the capabilities of this theory to describe the behavior of silica. The parameters involved in the model were estimated from our test data. In the Lade model, the elastic strain increments, which are recoverable upon unloading, are calculated using a constant value of the Poisson's ratio and a power law variation of the Young's modulus E with the confining pressure, σ_3 . However, for silica powder, in any given confined test, this modulus was found to vary with the state of stress, *i.e.* for $\sigma_3 = \text{constant}$, E is not constant. To better reproduce this non-linearity of the elastic response, a decaying exponential variation law of E with the mean stress was proposed. MATLAB version 6.1 (MATrix LABoratory developed by The Mathworks, Inc., 2002) routines were developed in order to simulate the behavior of silica powder with both the Drucker-Prager and the Lade models. Two robust and computationally inexpensive methods, namely the *closest point projection (CPP)* algorithm proposed by Ortiz and Pinsky (1983) and the *convex cutting plane (CCP)* algorithm proposed by Ortiz and Simo (1986) were implemented. Comparisons between the two algorithms showed the superiority in simplicity and robustness of the CCP algorithm. For isotropic compression, the agreement between theoretical predictions

using Lade's theory and measurements was not satisfactory. Consequently, a parameter sensitivity study was performed. It was shown that by adopting a linear work-hardening law rather than the power law proposed in Lade's theory, the model predictions were improved. Still, the initial non-linearity in the pressure-volumetric curve as well as the change in concavity of the curve for strains higher than 0.02 could not be reproduced by the theory. However, it is believed that those effects have to do with sample preparation rather than with real material behavior. Indeed, silica has a very low cohesion, hence it is very difficult to achieve closed packing density in the pre-compaction phase prior to the test, which explains the initial non-linearity in the response (up to 0.01 strains). Under deviatoric conditions, comparisons between theoretical predictions and data showed that the model could accurately predict silica behavior in triaxial tests over a large range of confining pressures. The model describes particularly well the effect of confining pressure on the volumetric strains. The non-linearity, the stress-path dependency and the gradual change from compressible to dilatant behavior were correctly modeled. It was thus demonstrated that the theory is applicable to silica for general 3-D conditions.

Another objective of this dissertation was to examine whether the material characterization and data analysis used for silica could be applied to industrial systems. Hence, for commercially available polyethylene pellets the minimum number of tests that are necessary to determine Lade model parameters was established, the procedure to be used to determine these parameters was developed, and it was demonstrated how the developed MATLAB routines could be used to predict the material's response under triaxial loading conditions. Indeed, only one hydrostatic compression test and two monotonic and cyclic confined tests are sufficient to determine the main characteristics of

the deformation and failure behavior. Based on the test results it can be concluded that under hydrostatic conditions the stress-strain response is linear and elastic. Under deviatoric conditions the behavior is elasto-plastic. The main characteristics of this behavior are: non-linearity, influence of confining pressure on the overall deformation and strength, stress-path dependency and compressibility followed by shear-dilatancy effects. To model those characteristics both Drucker-Prager model and Lade model were used. The procedure for determination of the parameters of those models was given. Then, numerical simulations were performed using the MATLAB routines used to simulate the response. Comparison between Lade's theory predictions and experimental measurements were excellent. It was thus demonstrated that the approach taken is very useful in predicting the mechanical behavior of a range of industrial systems under general loading conditions. The numerical algorithms developed in this study can be applied to Finite Element codes when geometry and stress distribution profiles are included in the formulation of the stress-strain problem. This study produced a model that provides improved predictions of powder behavior when subjected to stress and additionally, the model can be applied to the bulk materials contained in handling and storage devices, such as hoppers and bins.

APPENDIX A TRIAXIAL EXPERIMENTAL DATA

This section presents examples of raw data from the Instron machine and data reduction from the performed triaxial tests in Excel format.

Table A1: Raw data for Silica powder at 93 kPa of confining pressure from the Instron machine

Time (sec)	Extension (mm)	Strain (mm)	Load (N)
0	0	-0.0078	0.71114
2.008	-0.0033	-0.0039	-4.2901
4.6	-0.0077	-0.0106	-9.2968
9.6	-0.016	-0.0338	-8.3502
14.6	-0.0243	-0.0412	-10.351
19.6	-0.0326	-0.0622	-12.276
24.6	-0.041	-0.0452	-14.499
29.6	-0.0494	-0.0813	-16.706
34.6	-0.0577	-0.0764	-18.125
39.6	-0.066	-0.1045	-19.538
44.6	-0.0743	-0.1329	-20.616
49.6	-0.0827	-0.1461	-21.732
54.6	-0.091	-0.1282	-22.365
59.6	-0.0993	-0.1378	-22.012
64.6	-0.1077	-0.1356	-22.433
69.6	-0.1161	-0.1669	-22.037
74.6	-0.1244	-0.1912	-22.133
79.6	-0.1327	-0.1786	-22.099
84.6	-0.141	-0.2003	-21.722
89.6	-0.1494	-0.1973	-22.814
94.6	-0.1577	-0.2184	-24.049
99.6	-0.166	-0.22	-25.115

Triaxial Data Reduction

Table A2: Cyclic test done on silica powder at 40 kPa.

Time sec	Ext.(mm)	Strain	Load (N)	vol.piston (cm ³)	true vol. (cm ³)	E _v	E ₁	$\sigma_1 - \sigma_3$ (kPa)
0	0	-0.0111	0.2611	0	0.01111	2.157E-05	0	-0.0727
5	-0.0083	-0.0528	-2.593	-0.0041	0.05692	0.000110	5.8E-05	0.72241
10	-0.0166	-0.0405	-4.1935	-0.0081	0.04867	9.44E-05	0.00012	1.1683
15	-0.025	-0.0453	-5.5523	-0.0123	0.0576	0.000112	0.00017	1.54688
20	-0.0334	-0.0332	-6.7145	-0.0164	0.04957	9.62E-05	0.00023	1.87066
25	-0.0417	-0.0508	-7.5716	-0.0204	0.07128	0.000138	0.00029	2.10944
30	-0.05	-0.0849	-8.477	-0.0245	0.10946	0.000212	0.00035	2.36169
35	-0.0584	-0.0676	-9.3358	-0.0286	0.09625	0.000187	0.00041	2.60095
40	-0.0667	-0.0455	-10.027	-0.0327	0.07825	0.000152	0.00047	2.79361
45	-0.075	-0.0618	-10.684	-0.0368	0.09863	0.000191	0.00052	2.97648
50	-0.0833	-0.0577	-11.252	-0.0409	0.09856	0.000194	0.00058	3.13492
55	-0.0917	-0.0453	-11.69	-0.045	0.09027	0.0001753	0.00064	3.25683
60	-0.1	-0.0627	-11.924	-0.0491	0.11177	0.0002170	0.0007	3.32211
65	-0.1083	-0.0559	-12.25	-0.0532	0.10902	0.0002117	0.00076	3.41298
70	-0.1166	-0.0405	-12.487	-0.0572	0.09774	0.0001897	0.00081	3.47891
75	-0.125	-0.0703	-12.741	-0.0613	0.13159	0.0002555	0.00087	3.54974
80	-0.1334	-0.0353	-12.919	-0.0654	0.10079	0.0001957	0.00093	3.59912
85	-0.1417	-0.0492	-12.937	-0.0695	0.11876	0.0002306	0.00099	3.60429
90	-0.15	-0.0304	-12.826	-0.0736	0.104	0.0002019	0.00105	3.57318
95	-0.1583	-0.0352	-12.689	-0.0777	0.11288	0.0002192	0.0011	3.53518
100	-0.1667	-0.0035	-12.721	-0.0818	0.08527	0.0001655	0.00116	3.544
105	-0.175	0.01317	-12.766	-0.0859	0.07271	0.0001412	0.00122	3.55646
110	-0.1834	-0.0111	-12.862	-0.09	0.10103	0.0001962	0.00128	3.58333
115	-0.1916	0.02603	-12.736	-0.094	0.068	0.0001320	0.00134	3.54837
120	-0.2	0.01513	-12.766	-0.0981	0.08301	0.0001612	0.00139	3.5567
125	-0.2084	0.00893	-12.738	-0.1022	0.0933	0.0001811	0.00145	3.54879
130	-0.2166	0.03197	-12.774	-0.1063	0.07432	0.0001443	0.00151	3.55884
135	-0.225	0.04442	-12.847	-0.1104	0.06598	0.0001281	0.00157	3.57925
140	-0.2333	0.05155	-12.743	-0.1145	0.06291	0.0001221	0.00163	3.55022
145	-0.2417	0.04504	-12.796	-0.1186	0.07354	0.0001427	0.00169	3.56483

Table A3: Cyclic test done on silica powder at 93 kPa.

Time sec	Ext. (mm)	Strain	Load (N)	vol.piston (cm ³)	true vol. (cm ³)	E _v	E ₁	σ_1 - σ_3 (kPa)
0	0	-0.0078	0.71114	0	0.00776	1.404E-05	0	-0.1872
2.008	-0.0033	-0.0039	-4.2901	-0.0016	0.00559	1.010E-05	2.3E-05	1.12947
4.6	-0.0077	-0.0106	-9.2968	-0.0038	0.01436	2.596E-05	5.3E-05	2.44762
9.6	-0.016	-0.0338	-8.3502	-0.0079	0.04168	7.536E-05	0.00011	2.19841
14.6	-0.0243	-0.0412	-10.351	-0.0119	0.05309	9.5989E-05	0.00017	2.7252
19.6	-0.0326	-0.0622	-12.276	-0.016	0.07823	0.00014146	0.00022	3.23205
24.6	-0.041	-0.0452	-14.499	-0.0201	0.06529	0.00011806	0.00028	3.81715
29.6	-0.0494	-0.0813	-16.706	-0.0242	0.10557	0.00019089	0.00034	4.39835
34.6	-0.0577	-0.0764	-18.125	-0.0283	0.10467	0.00018926	0.0004	4.77191
39.6	-0.066	-0.1045	-19.538	-0.0324	0.1369	0.00024753	0.00045	5.14394
44.6	-0.0743	-0.1329	-20.616	-0.0365	0.16935	0.00030621	0.00051	5.42761
49.6	-0.0827	-0.1461	-21.732	-0.0406	0.18666	0.00033750	0.00057	5.7215
54.6	-0.091	-0.1282	-22.365	-0.0447	0.1728	0.00031245	0.00063	5.88825
59.6	-0.0993	-0.1378	-22.012	-0.0487	0.18652	0.00033727	0.00068	5.79512
64.6	-0.1077	-0.1356	-22.433	-0.0528	0.18846	0.00034077	0.00074	5.90598
69.6	-0.1161	-0.1669	-22.037	-0.0569	0.22387	0.00040480	0.0008	5.80181
74.6	-0.1244	-0.1912	-22.133	-0.061	0.2522	0.00045601	0.00085	5.82715
79.6	-0.1327	-0.1786	-22.099	-0.0651	0.24366	0.00044059	0.00091	5.81801
84.6	-0.141	-0.2003	-21.722	-0.0692	0.26945	0.00048722	0.00097	5.71884
89.6	-0.1494	-0.1973	-22.814	-0.0733	0.27061	0.00048931	0.00103	6.0065
94.6	-0.1577	-0.2184	-24.049	-0.0774	0.29576	0.00053478	0.00108	6.33145
99.6	-0.166	-0.22	-25.115	-0.0814	0.30146	0.00054510	0.00114	6.61224
104.6	-0.1743	-0.2444	-25.734	-0.0855	0.32995	0.00059661	0.0012	6.77519
109.6	-0.1827	-0.2522	-27.056	-0.0896	0.34184	0.00061811	0.00126	7.12314
114.6	-0.191	-0.2691	-28.688	-0.0937	0.36277	0.00065595	0.00131	7.55288
119.6	-0.1993	-0.2906	-29.924	-0.0978	0.38842	0.00070233	0.00137	7.87826
124.6	-0.2077	-0.3132	-31.765	-0.1019	0.41512	0.00075061	0.00143	8.36297
129.6	-0.216	-0.3129	-30.881	-0.106	0.41882	0.00075731	0.00148	8.13028
134.6	-0.2244	-0.3342	-31.321	-0.1101	0.44427	0.00080331	0.00154	8.24605
139.6	-0.2327	-0.3634	-31.076	-0.1142	0.47757	0.00086354	0.0016	8.18168
144.6	-0.2411	-0.3666	-30.748	-0.1183	0.4849	0.00087679	0.00166	8.09514
149.6	-0.2493	-0.3574	-29.256	-0.1223	0.47971	0.0008674	0.00171	7.70242
154.6	-0.2577	-0.3597	-28.73	-0.1264	0.48614	0.0008790	0.00177	7.56393
159.6	-0.2661	-0.3493	-28.155	-0.1305	0.4798	0.0008675	0.00183	7.41257
164.6	-0.2743	-0.3894	-29.572	-0.1346	0.524	0.0009474	0.00189	7.78557
169.6	-0.2827	-0.3675	-30.48	-0.1387	0.50614	0.0009152	0.00194	8.02458
174.6	-0.291	-0.4078	-31.652	-0.1428	0.55057	0.0009955	0.002	8.33308
179.6	-0.2994	-0.3981	-33.861	-0.1469	0.545	0.0009854	0.00206	8.91488
184.6	-0.3076	-0.4454	-35.098	-0.1509	0.59636	0.0010783	0.00211	9.24056

Table A4: Cyclic test done on silica powder at 27 kPa.

Time sec	Ext. (mm)	Strain	Load (N)	Vpiston (cm ³)	True Volume (cm ³)	E _v	E ₁	$\sigma_1 - \sigma_3$ (KPa)
0	0	-0.043	1.76584	0	0.04301	7.230E-05	0	-0.4455
4.842	-0.0081	-0.0581	-3.2412	-0.004	0.06206	0.0001043	5.4E-05	0.81772
9.842	-0.0164	-0.1087	-5.0163	-0.0081	0.11674	0.0001962	0.00011	1.26558
14.842	-0.0248	-0.1596	-6.7564	-0.0122	0.17178	0.0002888	0.00017	1.70459
19.842	-0.033	-0.2004	-8.0011	-0.0162	0.21665	0.0003642	0.00022	2.01861
24.842	-0.0415	-0.2544	-9.0632	-0.0204	0.27473	0.0004618	0.00028	2.28658
29.842	-0.0498	-0.3012	-10.034	-0.0245	0.32567	0.0005475	0.00033	2.53153
34.842	-0.0581	-0.3629	-10.706	-0.0285	0.39141	0.0006580	0.00039	2.70095
39.842	-0.0664	-0.4132	-11.501	-0.0326	0.44575	0.0007493	0.00044	2.90169
44.842	-0.0747	-0.4663	-12.081	-0.0367	0.50294	0.0008455	0.0005	3.04794
49.842	-0.0831	-0.4955	-12.786	-0.0408	0.53631	0.0009015	0.00055	3.22576
54.842	-0.0914	-0.5541	-13.313	-0.0449	0.59897	0.0010069	0.00061	3.35883
59.842	-0.0997	-0.588	-13.942	-0.049	0.63696	0.0010708	0.00066	3.51737
64.842	-0.1081	-0.6171	-14.496	-0.0531	0.67022	0.0011267	0.00072	3.65713
69.842	-0.1165	-0.6509	-15.004	-0.0572	0.70802	0.0011902	0.00078	3.78529
74.842	-0.1248	-0.7098	-15.601	-0.0613	0.77105	0.0012962	0.00083	3.93606
79.842	-0.1331	-0.7615	-15.069	-0.0653	0.82687	0.0013907	0.00089	3.8017
84.842	-0.1414	-0.7801	-15.895	-0.0694	0.84947	0.0014280	0.00094	4.01021
89.842	-0.1498	-0.8235	-16.665	-0.0735	0.89704	0.0015080	0.001	4.20448
94.842	-0.1581	-0.866	-17.41	-0.0776	0.94357	0.0015862	0.00105	4.39239
99.842	-0.1664	-0.9154	-17.857	-0.0817	0.99705	0.0016761	0.00111	4.50511
104.842	-0.1747	-0.9662	-18.364	-0.0858	1.05199	0.0017683	0.00116	4.63309
109.842	-0.1831	-1.0414	-18.789	-0.0899	1.1313	0.0019018	0.00122	4.74031
114.842	-0.1915	-1.094	-19.246	-0.094	1.18801	0.0019971	0.00128	4.85558
119.842	-0.1997	-1.1301	-19.676	-0.098	1.22811	0.0020645	0.00133	4.96399
124.842	-0.2081	-1.1641	-20.191	-0.1021	1.26629	0.0021288	0.00139	5.09414
129.842	-0.2164	-1.2201	-20.616	-0.1062	1.32636	0.0022297	0.00144	5.20117
134.842	-0.2248	-1.244	-21.076	-0.1103	1.35438	0.0022768	0.0015	5.31741
139.842	-0.2331	-1.2791	-21.409	-0.1144	1.39358	0.0023427	0.00155	5.4013
144.842	-0.2415	-1.3365	-21.893	-0.1185	1.45501	0.0024460	0.00161	5.52332
149.842	-0.2497	-1.3605	-22.225	-0.1226	1.48311	0.0024932	0.00166	5.60708
154.842	-0.2581	-1.4169	-22.614	-0.1267	1.54359	0.0025949	0.00172	5.70537
159.842	-0.2664	-1.4553	-22.96	-0.1308	1.58611	0.0026664	0.00178	5.79253
164.842	-0.2747	-1.5086	-23.325	-0.1349	1.64341	0.0027627	0.00183	5.88464
169.842	-0.2831	-1.5352	-23.717	-0.1389	1.67417	0.0028144	0.00189	5.98359
174.842	-0.2914	-1.603	-24.046	-0.143	1.74602	0.0029352	0.00194	6.06669
179.842	-0.2998	-1.6257	-24.476	-0.1471	1.7728	0.0029802	0.002	6.17507
184.842	-0.3081	-1.6662	-24.843	-0.1512	1.81744	0.0030553	0.00205	6.26759
189.842	-0.3164	-1.7411	-25.363	-0.1553	1.8964	0.0031880	0.00211	6.39894
194.842	-0.3247	-1.7796	-25.747	-0.1594	1.93896	0.0032596	0.00216	6.49565
199.842	-0.3331	-1.8186	-26.111	-0.1635	1.98211	0.0033321	0.00222	6.58771

Table A5: Cyclic test done on silica powder at 70 kPa.

Time sec	Ext. (mm)	Strain	Load (N)	Vpiston (cm ³)	True Volume (cm ³)	E _v	E ₁	σ_1 - σ_3 (kPa)
0	0	-0.0118	0.4931	0	0.01175	1.99E-05	0	-0.1274
1.392	-0.0024	0.00099	-4.5071	-0.0012	0.00018	3.085E-07	1.6E-05	1.16448
2.652	-0.0044	-0.0223	-9.5071	-0.0022	0.02451	4.152E-05	2.9E-05	2.45632
7.652	-0.0128	-0.0007	-13.383	-0.0063	0.00699	1.184E-05	8.5E-05	3.4577
12.652	-0.0211	-0.0328	-12.849	-0.0103	0.04319	7.316E-05	0.00014	3.31977
17.652	-0.0295	0.00161	-13.581	-0.0145	0.01286	2.175E-05	0.0002	3.50886
22.652	-0.0378	-0.0249	-14.803	-0.0186	0.04342	7.357E-05	0.00025	3.82457
27.652	-0.0461	-0.0049	-16.061	-0.0226	0.02752	4.663E-05	0.00031	4.14958
32.652	-0.0544	-0.0254	-16.887	-0.0267	0.05207	8.823E-05	0.00036	4.36315
37.652	-0.0628	-0.0415	-17.892	-0.0308	0.07232	0.0001225	0.00042	4.6226
42.652	-0.0712	-0.0285	-19.805	-0.0349	0.06341	0.0001074	0.00047	5.11691
47.652	-0.0794	-0.0544	-22.363	-0.039	0.09345	0.0001583	0.00053	5.7779
52.652	-0.0878	-0.0431	-24.602	-0.0431	0.08618	0.0001460	0.00059	6.35631
57.652	-0.0961	-0.0716	-26.532	-0.0472	0.11873	0.0002011	0.00064	6.85492
62.652	-0.1045	-0.0566	-28.272	-0.0513	0.10789	0.0001827	0.0007	7.30444
67.652	-0.1128	-0.0328	-29.543	-0.0554	0.08817	0.0001493	0.00075	7.63284
72.652	-0.1212	-0.0423	-31.686	-0.0595	0.10175	0.000172	0.00081	8.18661
77.652	-0.1294	-0.0659	-33.709	-0.0635	0.12945	0.0002193	0.00086	8.70914
82.652	-0.1378	-0.07	-35.737	-0.0676	0.13763	0.0002331	0.00092	9.23329
87.652	-0.1461	-0.0579	-37.848	-0.0717	0.12964	0.0002196	0.00097	9.7786
92.652	-0.1544	-0.075	-39.811	-0.0758	0.15078	0.0002554	0.00103	10.2859
97.652	-0.1627	-0.062	-41.205	-0.0799	0.1419	0.0002404	0.00109	10.6461
102.652	-0.1711	-0.0818	-42.237	-0.084	0.16576	0.0002808	0.00114	10.9127
107.652	-0.1795	-0.0732	-43.358	-0.0881	0.16134	0.0002734	0.0012	11.2022
112.652	-0.1879	-0.1054	-45.302	-0.0922	0.19761	0.000335	0.00125	11.7045
117.652	-0.1961	-0.1022	-47.589	-0.0962	0.1984	0.0003361	0.00131	12.2954
122.652	-0.2044	-0.0823	-48.245	-0.1003	0.18262	0.0003094	0.00136	12.4648
127.652	-0.2128	-0.0919	-48.433	-0.1045	0.19635	0.0003327	0.00142	12.5134
132.652	-0.2212	-0.11	-50.444	-0.1086	0.21854	0.0003703	0.00148	13.0331
137.652	-0.2295	-0.1234	-51.37	-0.1127	0.23601	0.0003999	0.00153	13.2722
142.652	-0.2378	-0.1149	-52.927	-0.1167	0.23158	0.0003924	0.00159	13.6746
147.652	-0.2462	-0.1152	-53.608	-0.1208	0.23608	0.0003940	0.00164	13.8504
152.652	-0.2545	-0.1335	-55.554	-0.1249	0.25844	0.0004379	0.0017	14.3532
157.652	-0.2628	-0.1203	-56.983	-0.129	0.24927	0.0004223	0.00175	14.7225
162.652	-0.2711	-0.1449	-58.182	-0.1331	0.27802	0.0004710	0.00181	15.0323
167.652	-0.2795	-0.1638	-58.717	-0.1372	0.301	0.0005099	0.00186	15.1706
172.652	-0.2878	-0.1495	-59.539	-0.1413	0.29076	0.0004926	0.00192	15.383
177.652	-0.2961	-0.1619	-60.415	-0.1453	0.30727	0.0005206	0.00198	15.6092
182.652	-0.3045	-0.1573	-61.493	-0.1495	0.30681	0.0005198	0.00203	15.8876

Table A6: Cyclic test done on silica powder at 350 kPa

Time sec	Ext. (mm)	Strain	Load N	Vpiston (cm ³)	True Volume (cm ³)	E _v	E ₁	$\sigma_1 - \sigma_3$ (kPa)
0	0	-0.01175	0.493097	0	0.011751	0	0	0
1.392	-0.00238	0.000986	-4.50708	-0.00117	0.000182	3.0855E-07	1.59E-05	1.164478
2188.4	-2.80398	-6.05035	-627.902	-1.3764	7.426747	0.0125828	0.018704	162.2286
2313.45	-3.01229	-6.93746	-699.293	-1.47865	8.416116	0.0142591	0.020094	180.6738
2433.45	-3.21232	-7.77883	-765.616	-1.57684	9.355673	0.0158510	0.021428	197.8094
2653.45	-3.57901	-9.28221	-883.301	-1.75684	11.03905	0.0187031	0.023874	228.2151
2858.45	-3.92066	-10.6614	-990.139	-1.92455	12.58599	0.0213240	0.026153	255.8185
3647.70	-4.47899	-13.0964	-1162.95	-2.19862	15.29502	0.0259138	0.029878	300.4676
3892.70	-4.88739	-14.5117	-1282.87	-2.39909	16.91083	0.0286514	0.032602	331.4509
4137.70	-5.29573	-15.8439	-1400.74	-2.59954	18.44344	0.0312481	0.035326	361.9038
4979.04	-5.98701	-18.3004	-1579.9	-2.93887	21.23925	0.0359849	0.039937	408.1937
5222.41	-6.39268	-19.3675	-1713.65	-3.138	22.50549	0.0381303	0.042643	442.7497
5387.41	-6.66763	-20.1196	-1787.49	-3.27297	23.39252	0.0396331	0.044477	461.8264
5642.41	-7.09257	-21.1115	-1901.86	-3.48156	24.5931	0.0416672	0.047312	491.3773
5832.41	-7.40923	-21.8396	-1986.87	-3.637	25.47658	0.0431641	0.049424	513.3408
6580.37	-7.98655	-23.2101	-2146.4	-3.92039	27.1305	0.0459663	0.053275	554.5579
6855.37	-8.44487	-24.1369	-2261.86	-4.14537	28.28223	0.0479176	0.056333	584.3871
7065.37	-8.7949	-24.7711	-2349.76	-4.31719	29.08828	0.0492833	0.058668	607.0978
7325.37	-9.22817	-25.4593	-2458.31	-4.52987	29.98917	0.0508096	0.061558	635.1442
8124.23	-9.92965	-26.664	-2640.24	-4.87421	31.53816	0.0534340	0.066237	682.1486
8334.23	-10.2797	-27.0679	-2722.05	-5.04606	32.11393	0.054409	0.068572	703.2871
9210.97	-11.1381	-28.0569	-2931.44	-5.46741	33.52427	0.0567990	0.074298	757.3851
9380.97	-11.4215	-28.2273	-2993.54	-5.6065	33.83382	0.0573235	0.076188	773.4286
9585.97	-11.7632	-28.417	-3069.01	-5.77423	34.19127	0.0579291	0.078468	792.9293
10302.8	-12.3813	-29.0324	-3199.82	-6.07765	35.11008	0.0594858	0.082591	826.7244
10545.1	-12.7851	-29.0902	-3299.6	-6.27586	35.3661	0.0599196	0.085285	852.5045
12063.2	-14.2254	-29.506	-3574.73	-6.98287	36.48882	0.0618217	0.094892	923.5885
12265.7	-14.563	-29.3118	-3672.7	-7.1486	36.46042	0.0617736	0.097144	948.9017
12973.1	-15.2243	-29.3072	-3749.74	-7.47319	36.78035	0.0623157	0.101555	968.8055
12997.4	-15.2648	-29.2588	-3809.79	-7.49307	36.75191	0.0622675	0.101826	984.3217
13002.4	-15.273	-29.2294	-3813.4	-7.49714	36.7265	0.0622244	0.101881	985.2528
13182.4	-15.5731	-29.0636	-3867.64	-7.64442	36.708	0.0621931	0.103882	999.2669
13387.4	-15.9147	-28.8527	-3926.57	-7.8121	36.66482	0.0621199	0.106161	1014.494
13552.4	-16.1897	-28.7107	-3973.62	-7.94709	36.65783	0.0621081	0.107995	1026.648
14360.3	-17.0491	-28.2108	-4133.31	-8.36898	36.57974	0.0619758	0.113729	1067.907
14365.3	-17.0574	-28.1896	-4134.11	-8.37304	36.56265	0.0619468	0.113784	1068.113
14490.3	-17.2658	-27.997	-4164.75	-8.47532	36.47234	0.0617938	0.115174	1076.032
14580.3	-17.4158	-27.8819	-4187.18	-8.54895	36.4308	0.0617234	0.116174	1081.826
14645.3	-17.5241	-27.7929	-4204.11	-8.60213	36.39506	0.0616629	0.116897	1086.2
14705.3	-17.6241	-27.7076	-4219.38	-8.6512	36.35881	0.0616015	0.117564	1090.145
14785.3	-17.7574	-27.5604	-4239.23	-8.71665	36.27706	0.0614630	0.118453	1095.275

Table A7: Monotonic test done on silica powder at 27 kPa.

Time sec	Ext. (mm)	Strain	Load (N)	Vpiston (cm ³)	True Volume (cm ³)	E _v	E ₁	$\sigma_1 - \sigma_3$ (kPa)
0	0	-0.00904	0.192613	0	0.009042	0	0	0
5	-0.00833	-0.02525	-4.07114	-0.00409	0.029334	5.387E-05	5.77E-05	1.079863
10	-0.01666	-0.02962	-3.64715	-0.00818	0.037797	6.942E-05	0.000115	0.967399
15	-0.02505	-0.01991	-3.7688	-0.01229	0.032205	5.915E-05	0.000173	0.999669
20	-0.03332	-0.01048	-3.56262	-0.01636	0.026834	4.928E-05	0.000231	0.944976
25	-0.04171	-0.01901	-3.95254	-0.02047	0.039487	7.252E-05	0.000289	1.048404
30	-0.04998	-0.00745	-4.43863	-0.02453	0.031982	5.874E-05	0.000346	1.177338
35	-0.05842	-0.00062	-4.78793	-0.02868	0.029303	5.382E-05	0.000405	1.26999
40	-0.06675	-0.02548	-5.79238	-0.03277	0.05825	0.0001069	0.000462	1.536418
45	-0.07497	-0.02576	-6.96288	-0.0368	0.06256	0.0001149	0.000519	1.846892
50	-0.0833	-0.02901	-7.92789	-0.04089	0.069903	0.0001283	0.000577	2.102858
55	-0.09174	-0.05485	-9.03501	-0.04503	0.09988	0.0001834	0.000635	2.39652
60	-0.10007	-0.06693	-10.203	-0.04912	0.116049	0.0002131	0.000693	2.706318
65	-0.1084	-0.0731	-10.9818	-0.05321	0.126316	0.0002320	0.000751	2.912906
70	-0.11668	-0.07371	-11.2545	-0.05727	0.130983	0.0002405	0.000808	2.985232
75	-0.12495	-0.08397	-12.2596	-0.06133	0.145306	0.0002668	0.000865	3.25183
80	-0.13339	-0.11281	-13.0577	-0.06548	0.178287	0.0003274	0.000924	3.463535
85	-0.14172	-0.13346	-13.7537	-0.06957	0.203032	0.0003729	0.000981	3.648132
90	-0.15005	-0.15185	-14.5225	-0.07366	0.225511	0.0004141	0.001039	3.852079
95	-0.15833	-0.18141	-15.1001	-0.07772	0.259132	0.0004759	0.001096	4.005279
100	-0.16671	-0.18365	-15.6512	-0.08184	0.265489	0.0004872	0.001154	4.151452
105	-0.17504	-0.21371	-16.2322	-0.08592	0.299639	0.0005503	0.001212	4.305553
110	-0.18332	-0.24092	-16.5833	-0.08999	0.330903	0.0006077	0.001269	4.398692
115	-0.19165	-0.24897	-17.09	-0.09407	0.343041	0.0006300	0.001327	4.533098
120	-0.20003	-0.27783	-17.519	-0.09819	0.37602	0.0006906	0.001385	4.646882
125	-0.20836	-0.30191	-17.9084	-0.10228	0.40419	0.0007421	0.001443	4.750167
130	-0.21664	-0.33379	-18.3099	-0.10634	0.44013	0.0008083	0.0015	4.856675
135	-0.22502	-0.37179	-18.8151	-0.11046	0.482252	0.0008857	0.001558	4.990663
140	-0.2333	-0.37449	-19.0783	-0.11452	0.489013	0.0008981	0.001615	5.060476
145	-0.24174	-0.41396	-19.5324	-0.11866	0.532625	0.0009782	0.001674	5.180923
150	-0.25007	-0.44124	-19.9041	-0.12275	0.563996	0.0010358	0.001732	5.279526
155	-0.25834	-0.46195	-20.1425	-0.12681	0.588765	0.0010813	0.001789	5.342772
160	-0.26667	-0.4763	-20.6673	-0.1309	0.6072	0.0011152	0.001847	5.481961
165	-0.27506	-0.51122	-20.9913	-0.13502	0.646239	0.0011869	0.001905	5.567907

Table A8: Monotonic test done on silica powder done at 40 kPa.

Time sec	Ext. (mm)	Strain	Load (N)	Vpiston (cm ³)	True Volume (cm ³)	E _v	E ₁	$\sigma_1 - \sigma_3$ (kPa)
0	0	-0.01427	-0.01302	0.00E+00	1.43E-02	0.00E+00	0	0
2.5	-0.00408	-0.00102	-0.08131	-2.00E-03	3.02E-03	6.18E-06	0.000295	0.020514
5	-0.00827	-0.00179	-0.04881	-4.06E-03	5.85E-03	1.20E-05	0.000599	0.012313
7.5	-0.01241	0.061545	-0.08224	-6.09E-03	-5.55E-02	-1.13E-04	0.000899	0.020747
10	-0.01666	0.050489	-0.04422	-8.18E-03	-4.23E-02	-8.65E-05	0.001207	0.011156
12.5	-0.02074	0.067952	-0.01861	-1.02E-02	-5.78E-02	-1.18E-04	0.001502	0.004694
15	-0.02493	0.068025	0.020327	-1.22E-02	-5.58E-02	-1.14E-04	0.001806	0.005128
17.5	-0.02913	0.059898	-0.05372	-1.43E-02	-4.56E-02	-9.32E-05	0.002109	0.013554
20	-0.03332	-0.00293	-0.07146	-1.64E-02	1.93E-02	3.94E-05	0.002413	0.018028
22.5	-0.03751	0.045034	-0.15807	-1.84E-02	-2.66E-02	-5.44E-05	0.002717	0.039879
25	-0.04159	0.000113	-0.15145	-2.04E-02	2.03E-02	4.15E-05	0.003012	0.038208
27.5	-0.04573	0.021237	-0.19871	-2.24E-02	1.21E-03	2.47E-06	0.003312	0.050133
30	-0.04998	0.007215	-0.31211	-2.45E-02	1.73E-02	3.54E-05	0.00362	0.078742
32.5	-0.05412	0.024239	-0.41299	-2.66E-02	2.33E-03	4.75E-06	0.003919	0.104193
35	-0.05831	0.01721	-0.66622	-2.86E-02	1.14E-02	2.33E-05	0.004223	0.168081
37.5	-0.06245	0.031781	-1.03939	-3.07E-02	-1.13E-03	-2.30E-06	0.004523	0.262230
40	-0.06658	0.006886	-1.33171	-3.27E-02	2.58E-02	5.27E-05	0.004822	0.335981
42.5	-0.07083	-0.01387	-1.47778	-3.48E-02	4.86E-02	9.94E-05	0.00513	0.372831
45	-0.07491	-0.03009	-1.84921	-3.68E-02	6.69E-02	1.37E-04	0.005426	0.466540
47.5	-0.07916	-0.0097	-2.16936	-3.89E-02	4.86E-02	9.93E-05	0.005733	0.547312
50	-0.0833	-0.02844	-2.38784	-4.09E-02	6.93E-02	1.42E-04	0.006033	0.602434
52.5	-0.08744	-0.02083	-2.66343	-4.29E-02	6.37E-02	1.30E-04	0.006333	0.671963
55	-0.09163	0.001394	-2.90469	-4.50E-02	4.36E-02	8.91E-05	0.006636	0.732831
57.5	-0.09577	0.025338	-3.38474	-4.70E-02	2.17E-02	4.43E-05	0.006936	0.853943
60	-0.10002	0.24101	-4.22528	-4.91E-02	-1.92E-01	-3.92E-04	0.007244	1.066008
62.5	-0.10415	0.234017	-5.10329	-5.11E-02	-1.83E-01	-3.74E-04	0.007543	1.287521
65	-0.10829	0.24727	-5.91246	-5.32E-02	-1.94E-01	-3.97E-04	0.007843	1.491668
67.5	-0.11248	0.216151	-6.72124	-5.52E-02	-1.61E-01	-3.29E-04	0.008147	1.695717
70	-0.11656	0.198029	-7.50309	-5.72E-02	-1.41E-01	-2.88E-04	0.008442	1.892973
72.5	-0.12076	0.189462	-8.21246	-5.93E-02	-1.30E-01	-2.66E-04	0.008746	2.071942
75	-0.12501	0.216773	-8.97149	-6.14E-02	-1.55E-01	-3.18E-04	0.009054	2.263438
77.5	-0.12909	0.208939	-9.61919	-6.34E-02	-1.46E-01	-2.98E-04	0.009349	2.426849
80	-0.13328	0.243096	-10.1755	-6.54E-02	-1.78E-01	-3.63E-04	0.009653	2.567209
82.5	-0.13742	0.174415	-10.6458	-6.75E-02	-1.07E-01	-2.19E-04	0.009952	2.685862
85	-0.14167	0.168484	-11.1549	-6.95E-02	-9.89E-02	-2.02E-04	0.01026	2.814301
87.5	-0.1458	0.22146	-11.6078	-7.16E-02	-1.50E-01	-3.06E-04	0.01056	2.928567
90	-0.14994	0.178442	-11.8968	-7.36E-02	-1.05E-01	-2.14E-04	0.010859	3.001467
92.5	-0.15408	0.172072	-12.2763	-7.56E-02	-9.64E-02	-1.97E-04	0.011159	3.097209

Table A9: Monotonic test done on silica powder at 93 kPa

Time sec	Ext. (mm)	Strain	Load (N)	Vpiston (cm ³)	True Volume (cm ³)	E _v	E _i	$\sigma_1 - \sigma_3$ (kPa)
0	0	0.049412	0.038385	0.00E+00	-4.94E-02	0	0	0
2.5	-0.00414	0.018339	-3.98291	-2.03E-03	-1.63E-02	-3.20E-05	2.819E-05	1.0564
5	-0.00833	0.014734	-5.24679	-4.09E-03	-1.06E-02	-2.09E-05	5.677E-05	1.3917
7.5	-0.01247	0.017335	-6.24228	-6.12E-03	-1.12E-02	-2.20E-05	8.496E-05	1.6557
10	-0.01666	0.010263	-7.30496	-8.18E-03	-2.08E-03	-4.09E-06	0.0001135	1.9376
12.5	-0.0208	0.034583	-8.20257	-1.02E-02	-2.44E-02	-4.79E-05	0.0001417	2.1757
15	-0.02493	-0.0063	-9.11114	-1.22E-02	1.85E-02	3.64E-05	0.0001699	2.4167
17.5	-0.02918	0.02135	-10.0696	-1.43E-02	-7.03E-03	-1.38E-05	0.0001989	2.6709
20	-0.03326	-0.01844	-10.9257	-1.63E-02	3.48E-02	6.83E-05	0.0002267	2.8980
22.5	-0.03746	-0.0204	-11.7227	-1.84E-02	3.88E-02	7.61E-05	0.0002553	3.1094
25	-0.04165	0.003099	-12.585	-2.04E-02	1.73E-02	3.41E-05	0.0002838	3.3381
27.5	-0.04584	-0.02902	-13.4072	-2.25E-02	5.15E-02	1.01E-04	0.0003124	3.556
30	-0.05004	-0.02273	-14.1763	-2.46E-02	4.73E-02	9.28E-05	0.000341	3.760
32.5	-0.05412	-0.00502	-14.847	-2.66E-02	3.16E-02	6.20E-05	0.0003688	3.9381
35	-0.05831	-0.01967	-15.5472	-2.86E-02	4.83E-02	9.48E-05	0.0003974	4.1238
37.5	-0.0625	-0.03892	-16.1104	-3.07E-02	6.96E-02	1.37E-04	0.0004259	4.2732
40	-0.06658	-0.01447	-16.7131	-3.27E-02	4.72E-02	9.26E-05	0.0004537	4.4331
42.5	-0.07083	-0.03372	-17.3118	-3.48E-02	6.85E-02	1.34E-04	0.0004827	4.5919
45	-0.07497	0.025001	-17.8416	-3.68E-02	1.18E-02	2.32E-05	0.0005109	4.7324
47.5	-0.07911	-0.0042	-18.3807	-3.88E-02	4.30E-02	8.45E-05	0.0005391	4.8754
50	-0.08336	-0.03733	-18.8444	-4.09E-02	7.82E-02	1.54E-04	0.0005681	4.9984
52.5	-0.08744	0.001502	-19.3538	-4.29E-02	4.14E-02	8.13E-05	0.0005959	5.1335
55	-0.09163	0.030294	-19.7665	-4.50E-02	1.47E-02	2.88E-05	0.0006244	5.2430
57.5	-0.09582	0.025457	-20.2126	-4.70E-02	2.16E-02	4.24E-05	0.000653	5.3613
60	-0.09996	0.019251	-20.7099	-4.91E-02	2.98E-02	5.85E-05	0.0006812	5.4932
62.5	-0.10421	-0.00758	-21.0493	-5.12E-02	5.87E-02	1.15E-04	0.0007102	5.5832
65	-0.10829	-0.00183	-21.392	-5.32E-02	5.50E-02	1.08E-04	0.000738	5.6742
67.5	-0.11248	0.007525	-21.79	-5.52E-02	4.77E-02	9.36E-05	0.0007665	5.7797
70	-0.11668	-0.02478	-22.1866	-5.73E-02	8.21E-02	1.61E-04	0.0007951	5.8849
72.5	-0.12081	-0.02907	-22.5549	-5.93E-02	8.84E-02	1.73E-04	0.0008233	5.9826
75	-0.12501	-0.02624	-22.8497	-6.14E-02	8.76E-02	1.72E-04	0.0008519	6.0608
77.5	-0.12909	-0.00165	-23.1639	-6.34E-02	6.50E-02	1.28E-04	0.0008797	6.1441
80	-0.13328	-0.00133	-23.4667	-6.54E-02	6.68E-02	1.31E-04	0.0009083	6.2244
82.5	-0.13753	0.030476	-23.6263	-6.75E-02	3.70E-02	7.27E-05	0.0009372	6.2666
85	-0.14161	0.013594	-23.8022	-6.95E-02	5.59E-02	1.10E-04	0.000965	6.3134
87.5	-0.1458	0.016696	-23.8971	-7.16E-02	5.49E-02	1.08E-04	0.0009936	6.3386
90	-0.14994	0.02208	-23.9844	-7.36E-02	5.15E-02	1.01E-04	0.0010218	6.3618

Table A10: Monotonic test done on silica powder at 70 kPa.

Time sec	Extensio n mm	Strain	Load (N)	V piston (cm ³)	True volume (cm ³)	E _v	E ₁	$\sigma_1 - \sigma_3$ (kPa)
0	0	0.009	0.043577	0.00E+00	-9.00E-03	0.00E+00	0	0
2.336	-0.0038	-0.01309	-4.963	-1.86E-03	1.49E-02	3.07E-05	0.000273	1.4162
4.836	-0.00805	-0.01407	-6.91301	-3.95E-03	1.80E-02	3.70E-05	0.000579	1.9727
7.336	-0.01218	0.001796	-8.04895	-5.98E-03	4.18E-03	8.60E-06	0.000877	2.2968
9.836	-0.01632	0.00219	-9.1477	-8.01E-03	5.82E-03	1.20E-05	0.001175	2.6104
12.336	-0.02051	0.009	-10.2652	-1.01E-02	1.07E-03	2.20E-06	0.001477	2.9293
14.836	-0.02465	-0.00435	-11.1451	-1.21E-02	1.64E-02	3.38E-05	0.001774	3.1804
17.336	-0.02884	0.003292	-11.9405	-1.42E-02	1.09E-02	2.23E-05	0.002076	3.4073
19.836	-0.03304	-0.01379	-12.7485	-1.62E-02	3.00E-02	6.16E-05	0.002378	3.6379
22.336	-0.03717	0.060022	-13.467	-1.82E-02	-4.18E-02	-8.58E-05	0.002676	3.8429
24.836	-0.04137	0.010221	-14.135	-2.03E-02	1.01E-02	2.07E-05	0.002978	4.0336
27.336	-0.0455	0.010772	-14.6938	-2.23E-02	1.16E-02	2.38E-05	0.003276	4.1930
29.836	-0.04964	0.002071	-15.2721	-2.44E-02	2.23E-02	4.58E-05	0.003573	4.3581
32.336	-0.05389	0.054195	-15.875	-2.65E-02	-2.77E-02	-5.70E-05	0.003879	4.5301
34.836	-0.05797	-0.00053	-16.3352	-2.85E-02	2.90E-02	5.95E-05	0.004173	4.6614
37.336	-0.06222	0.024433	-16.794	-3.05E-02	6.11E-03	1.26E-05	0.004479	4.792
39.836	-0.06636	0.042936	-17.2784	-3.26E-02	-1.04E-02	-2.13E-05	0.004777	4.930
42.336	-0.07049	0.03707	-17.6691	-3.46E-02	-2.47E-03	-5.07E-06	0.005075	5.0421
44.836	-0.07474	0.011087	-18.1477	-3.67E-02	2.56E-02	5.26E-05	0.00538	5.1787
47.336	-0.07882	0.035259	-18.4889	-3.87E-02	3.43E-03	7.05E-06	0.005674	5.2760
49.836	-0.08302	0.044196	-19.0035	-4.08E-02	-3.44E-03	-7.08E-06	0.005976	5.4229
52.336	-0.08721	0.018134	-19.3672	-4.28E-02	2.47E-02	5.07E-05	0.006278	5.5267
54.836	-0.09135	0.006087	-19.8068	-4.48E-02	3.88E-02	7.96E-05	0.006576	5.6521
57.336	-0.0956	0.075336	-20.1818	-4.69E-02	-2.84E-02	-5.84E-05	0.006882	5.7591
59.836	-0.09968	0.041164	-20.5917	-4.89E-02	7.76E-03	1.59E-05	0.007175	5.8761
62.336	-0.10387	0.088997	-21.011	-5.10E-02	-3.80E-02	-7.81E-05	0.007477	5.9957
64.836	-0.10806	0.041086	-21.3493	-5.30E-02	1.20E-02	2.46E-05	0.007779	6.0923
67.336	-0.11214	0.033881	-21.6693	-5.50E-02	2.12E-02	4.35E-05	0.008073	6.1836
69.836	-0.11639	0.004591	-22.1016	-5.71E-02	5.25E-02	1.08E-04	0.008379	6.3070
72.336	-0.12053	-5.45E-05	-22.3838	-5.92E-02	5.92E-02	1.22E-04	0.008676	6.3875
74.836	-0.12472	-0.03403	-22.7644	-6.12E-02	9.53E-02	1.96E-04	0.008978	6.4961
77.336	-0.12892	0.000615	-22.9544	-6.33E-02	6.27E-02	1.29E-04	0.00928	6.5503
79.836	-0.133	0.021008	-23.2515	-6.53E-02	4.43E-02	9.10E-05	0.009574	6.6351
82.336	-0.13719	0.003646	-23.4166	-6.73E-02	6.37E-02	1.31E-04	0.009876	6.68227

APPENDIX B ELASTIC PARAMETERS

This appendix presents the elastic parameters (Young's modulus and Bulk modulus) determined from the unloading and re-loading cycles of the (σ_1 - σ_3) vs. axial strain curves for silica powder. See Tables B1 and B2.

Table B1: Young's modulus E, and Bulk modulus K, at 27, 40(1), and 70 kPa of confining pressure.

27 kPa	Cycle	σ_1 - σ_3 (kPa)	E(kPa)	K(kPa)
	1	24.76	44420	35265
	2	50.01	56988	59916
	3	75.21	71676	121479
	4	87.82	67380	73252
	5	99.2	76004	130227
40 kPa-	Cycle	σ_1 - σ_3 (kPa)	E(kPa)	K(kPa)
	1	26.26	43484	26316
	2	78.87	69685	105012
	3	131.52	90324	148055
70 kPa	Cycle	σ_1 - σ_3 (kPa)	E(kPa)	K(kPa)
	1	52.37	72528	46836
	2	91.71	84673	65539
	3	130.97	96064	82180
	4	157.17	100422	52546
	5	170.32	104629	155840
	6	183.40	106597	265716

Table B2: Young's modulus E, and Bulk modulus K, at 40 (2nd), 93 and 350 kPa of confining pressure.

40 kPa- (2 nd)	Cycle	$\sigma_1 - \sigma_3$ (kPa)	E(kPa)	K(kPa)
	1	26.26	43484	26316
	2	78.87	69685	105012
	3	131.52	90324	148055
93 kPa	Cycle	$\sigma_1 - \sigma_3$ (kPa)	E(kPa)	K(kPa)
	1	52.41	78236	49968
	2	104.95	95288	88949
	3	157.61	108258	62311
	4	210.28	117683	69633
	5	236.64	120194	337706
	6	262.99	119764	72773
	7	289.27	112954	179674
	8	315.55	121328	79827
350 kPa	Cycle	$\sigma_1 - \sigma_3$ (kPa)	E(kPa)	K(kPa)
	1	129.08	125328	63845
	2	258.25	169690	138931
	3	387.47	183431	83560
	4	516.67	190137	150184
	6	723.35	215173	131808
	7	800.83	193497	1166524
	8	852.49	188770	3615654
	9	904.16	209465	333901
	10	955.83	174675	254762
	11	1033.31	223422	3414135
	12	1162.51	219887	1024865

APPENDIX C DETERMINATION OF PLASTIC STRAINS

This appendix presents the equations needed to determine the plastic collapse strains and plastic expansive strains that correspond to Lade model (1977).

Determination of Plastic Collapse Strains

The yield condition (equation D1) is used to determine the collapse strains using the following rational:

$$\frac{\partial f_c}{\partial \sigma_y} = 2I_1 \frac{\partial I_1}{\partial \sigma_y} + 2 \frac{\partial I_2}{\partial \sigma_y} \quad (C1)$$

where:

$$f_c = I_1^2 + 2 \cdot I_2^2,$$

in general:

$$I_1 = \sigma_{11} + \sigma_{22} + \sigma_{33}$$

$$I_2 = \sigma_{12}^2 + \sigma_{13}^2 + \sigma_{23}^2 - \sigma_{11}\sigma_{22} - \sigma_{11}\sigma_{33} - \sigma_{22}\sigma_{33}$$

$$\begin{aligned} \frac{\partial I_1}{\partial \sigma_{11}} &= 1 & \frac{\partial I_1}{\partial \sigma_{22}} &= 1 & \frac{\partial I_1}{\partial \sigma_{33}} &= 1 \\ \frac{\partial I_1}{\partial \sigma_y} &= \delta_y & & & & \end{aligned} \quad (C2)$$

$$\frac{\partial I_2}{\partial \sigma_{11}} = -\sigma_{22} - \sigma_{33} \quad (C3)$$

$$\frac{\partial I_2}{\partial \sigma_{22}} = -\sigma_{33} - \sigma_{11} \quad (C4)$$

$$\frac{\partial I_2}{\partial \sigma_{33}} = -\sigma_{22} - \sigma_{11} \quad (C5)$$

$$\frac{\partial I_2}{\partial \sigma_{12}} = \sigma_{12} \quad (C6)$$

$$\frac{\partial I_2}{\partial \sigma_{11}} = -(\sigma_{11} + \sigma_{22} + \sigma_{33}) + \sigma_{11} = -I_1 + \sigma_{11} \quad (C7)$$

$$\frac{\partial I_2}{\partial \sigma_{22}} = -I_1 + \sigma_{22} \quad (C8)$$

$$\frac{\partial I_2}{\partial \sigma_{33}} = -I_1 + \sigma_{33} \quad (C9)$$

$$\frac{\partial I_2}{\partial \sigma_{ij}} = \sigma_{ij} \quad i \neq j \quad (C10)$$

so

$$\frac{\partial I_2}{\partial \sigma_{ij}} = \sigma_{ij} - I_1 \delta_{ij} \quad (C11)$$

$$\frac{\partial f_c}{\partial \sigma_{ij}} = 2\sigma_{ij} \quad (\text{Hydrostatic condition}) \quad (C12)$$

$$\frac{\partial f_c}{\partial \sigma_{11}} = 2\sigma_{11} = 2\sigma_3 \quad (C13)$$

$$\frac{\partial f_c}{\partial \sigma_{22}} = \frac{\partial f_c}{\partial \sigma_{33}} = 2\sigma_{22} = 2\sigma_{33} = 2\sigma_3 \quad (C14)$$

The relationship between stress and strain is derived according to the following

$$\text{expression: } d\epsilon^{col} = d\lambda \cdot \left(\frac{\partial g_c}{\partial \sigma_{ij}} \right) \text{ for collapse plastic strains } g_c = f_c$$

$$\Rightarrow \dot{\epsilon}_v^p = \dot{\lambda} 6\sigma_3 \quad (C15)$$

The stress-strain relationship given in equation D15 involves one parameter, λ (consistency parameter) which determines the absolute magnitude of the strain increment.

Determination of $\dot{\lambda}$

$$\frac{\partial f_c}{\partial \sigma_{ij}} \dot{\sigma}_{ij} + \frac{\partial f_c}{\partial W} \dot{W} = 0 \quad (\text{Consistency condition}) \quad (C16)$$

where W is the irreversible stress work $W = \int \sigma_{ij} d\epsilon_{ij}^{irreversible}$

$$\frac{\partial f_c}{\partial \sigma_{ij}} \dot{\sigma}_{ij} + \frac{\partial f_c}{\partial W} \sigma_{ij} \dot{\epsilon}_{ij}^p = 0 \quad (C17)$$

$$\frac{\partial f_c}{\partial \sigma_{ij}} \dot{\sigma}_{ij} + \frac{\partial f_c}{\partial W} \sigma_{ij} \dot{\lambda} \frac{\partial f_c}{\partial \sigma_{ij}} = 0 \quad (C18)$$

For no shear components:

$$\begin{aligned} & \frac{\partial f_c}{\partial \sigma_{11}} \dot{\sigma}_{11} + \frac{\partial f_c}{\partial \sigma_{22}} \dot{\sigma}_{22} + \frac{\partial f_c}{\partial \sigma_{33}} \dot{\sigma}_{33} + \\ & + \left(\frac{\partial f_c}{\partial W} \right) \dot{\lambda} \left(\sigma_{11} \frac{\partial f_c}{\partial \sigma_{11}} + \sigma_{22} \frac{\partial f_c}{\partial \sigma_{22}} + \sigma_{33} \frac{\partial f_c}{\partial \sigma_{33}} \right) = 0 \end{aligned} \quad (C19)$$

For hydrostatic conditions, Lade (1977) proposed the following expression for the collapse yield function of a cohesionless soil:

$$f_c = \left(\frac{W}{U \cdot p_a} \right)^{\frac{1}{d}} p_a^2, \quad (C20)$$

where U and d are material constants and p_a stands for the atmospheric pressure.

Plotting expression D20 into D19 results:

$$(2\sigma_3 \dot{\sigma}_3) \dot{\lambda} + \left[\frac{1}{d} \left(\frac{W}{U \cdot p_a} \right)^{\frac{1}{d}-1} \frac{1}{U \cdot p_a} p_a^2 \right] \dot{\lambda} (3\sigma_3 2\sigma_3) = 0 \quad (C21)$$

$$\dot{\lambda} = \frac{-6\dot{\sigma}_3\dot{\sigma}_3}{3\dot{\sigma}_3 2\dot{\sigma}_3 \left[\frac{1}{d} \left(\frac{W}{Up_a} \right)^{\frac{1}{d}-1} \frac{p_a}{U} \right]} \quad (\text{C22})$$

$$\dot{\varepsilon}_\nu^p = \dot{\lambda}(6\dot{\sigma}_3) = \frac{-6\dot{\sigma}_3}{\frac{p_a}{U \cdot d} \left(\frac{W}{U \cdot p_a} \right)^{\frac{1}{d}-1}} \quad (\text{C23})$$

and

$$W = U \cdot p_a \left(\frac{f_c}{p_a^2} \right)^d = U \cdot p_a \left(\frac{3\dot{\sigma}_3^2}{p_a^2} \right)^d \quad (\text{C24})$$

$$\frac{W}{U \cdot p_a} = \frac{3^d \dot{\sigma}_3^{2d}}{p_a^2} \quad (\text{C25})$$

$$\dot{\varepsilon}_\nu^p = \frac{-6\dot{\sigma}_3}{\frac{p_a}{U \cdot d} \frac{3^{1-d} \dot{\sigma}_3^{2d \left(\frac{1-d}{d} \right)}}{\left(p_a^2 \right)^{\frac{1-d}{d}}}} \quad (\text{C26})$$

$$\dot{\varepsilon}_V^c = \frac{-6\dot{\sigma}_3 U d}{3^{1-d} \dot{\sigma}_3^{2(1-d)} p_a^{1-\frac{2(1-d)}{d}}} \quad (\text{C27})$$

$$\dot{\lambda} = \frac{\dot{W}}{2f_c} \quad (\text{C28})$$

$$\dot{W} = U \cdot d \cdot p_a \left(\frac{p_a^2}{f_c} \right)^{1-d} d \left(\frac{f_c}{p_a^2} \right) \quad (\text{C29})$$

$$f_c = 3\dot{\sigma}_3^2 \quad (\text{C30})$$

Determination of Plastic Expansive Strains

The plastic potential function g_p (equation D32) is used to determine the expansive strains using the following rational:

$$g_p = I_1^3 - \left(27 + \eta_2 \left(\frac{p_a}{I_1} \right)^m \right) I_3 \quad (C31)$$

where η_2 is a constant for a given values of f_p (yield function for plastic expansive strains) and σ_3 (confining pressure). The plastic potential describes a series of surfaces which are normal to the plastic strain increment directions.

The relationship between stress and strain is derived according to the following expression

$$d\epsilon_p = d\lambda_p \cdot \left(\frac{\partial g_p}{\partial \sigma_y} \right) \quad (C32)$$

$$\frac{\partial g_p}{\partial \sigma_y} = 3I_1^2 \frac{\partial I_1}{\partial \sigma_y} - 27 \frac{\partial I_3}{\partial \sigma_y} + I_3 \left(\eta_2 p_a^m m I_1^{m-1} \frac{\partial I_1}{\partial \sigma_y} \right) - \eta_2 \left(\frac{p_a}{I_1} \right)^m \frac{\partial I_3}{\partial \sigma_y} \quad (C33)$$

As a general rule:

$$I_1 = \sigma_{11} + \sigma_{22} + \sigma_{33} \quad \Rightarrow \quad \frac{\partial I_1}{\partial \sigma_{11}} = 1 \quad \frac{\partial I_1}{\partial \sigma_{22}} = 1 \quad \frac{\partial I_1}{\partial \sigma_{33}} = 1$$

$$\frac{\partial I_1}{\partial \sigma_{12}} = 0$$

$$\frac{\partial I_1}{\partial \sigma_{ij}} = \delta_{ij} \quad (C34)$$

$$\frac{\partial g_p}{\partial \sigma_y} \sigma_y = 3I_1^2 \sigma_y \delta_y - \left(27 + \eta_2 \left(\frac{p_a}{I_1} \right)^m \right) \frac{\partial I_3}{\partial \sigma_y} \sigma_y + \left(\frac{I_3}{I_1} \right) \eta_2 m \left(\frac{p_a}{I_1} \right)^m \delta_y \sigma_y \quad (C35)$$

$$\begin{aligned}
\frac{\partial g_p}{\partial \sigma_y} \sigma_y &= 3I_1^3 - 3I_3 \left(27 + \eta_2 \left(\frac{p_a}{I_1} \right)^m \right) + I_3 m \eta_2 \left(\frac{p_a}{I_1} \right)^m = \\
&= 3g_p + m \eta_2 \left(\frac{p_a}{I_1} \right)^m I_3
\end{aligned} \tag{C36}$$

$$I_3 = \det \underline{\sigma} = \sigma_{11} [\sigma_{22} \sigma_{33} - \sigma_{23} \sigma_{32}] - \sigma_{12} [\sigma_{21} \sigma_{33} - \sigma_{23} \sigma_{31}] + \sigma_{13} [\sigma_{21} \sigma_{32} - \sigma_{22} \sigma_{31}] \tag{C37}$$

$$I_3 = \sigma_{11} + \sigma_{22} + \sigma_{33} - \sigma_{11} \sigma_{23}^2 - \sigma_{22} \sigma_{13}^2 - \sigma_{33} \sigma_{12}^2 + 2\sigma_{12} \sigma_{13} \sigma_{23} \tag{C38}$$

$$\frac{\partial I_3}{\partial \sigma_{11}} = \sigma_{22} \sigma_{33} - \sigma_{23}^2 \tag{C39}$$

$$\frac{\partial I_3}{\partial \sigma_{12}} = -\sigma_{21} \sigma_{33} + \sigma_{23} \sigma_{31} \tag{C40}$$

$$\frac{\partial I_3}{\partial \sigma_{21}} = -\sigma_{13} \sigma_{23} + \sigma_{12} \sigma_{33} \tag{C41}$$

$$\frac{\partial I_3}{\partial \sigma_{13}} = -\sigma_{21} \sigma_{23} - \sigma_{22} \sigma_{31} \tag{C42}$$

$$\frac{\partial I_3}{\partial \sigma_y} \sigma_y = \frac{\partial I_3}{\partial \sigma_{11}} \sigma_{11} + \frac{\partial I_3}{\partial \sigma_{22}} \sigma_{22} + \frac{\partial I_3}{\partial \sigma_{33}} \sigma_{33} + 2 \frac{\partial I_3}{\partial \sigma_{12}} \sigma_{12} + 2 \frac{\partial I_3}{\partial \sigma_{13}} \sigma_{13} + 2 \frac{\partial I_3}{\partial \sigma_{23}} \sigma_{23}$$

$$\frac{\partial I_3}{\partial \sigma_y} \sigma_y = 3I_3 \tag{C43}$$

$$d\dot{\varepsilon}_y^p = d\lambda_p \frac{\partial g_p}{\partial \sigma_y} \tag{C44}$$

$$\sigma_y d\varepsilon^p = d\lambda_p \frac{\partial g_p}{\partial \sigma_y} \sigma_y \tag{C45}$$

$$dW^p = d\lambda_p \frac{\partial g_p}{\partial \sigma_{ij}} \sigma_{ij} \quad (C46)$$

$$dW^p = d\lambda_p \left[3g_p + m\eta_2 \left(\frac{p_a}{I_1} \right)^m I_3 \right] \quad (C47)$$

The increment of the plastic work per volume, dW^p can be determined from the relations between W^p and f_p based on experiments. Lade (1977), proposed the following plastic expansive work-hardening function:

$$F(W_p) = H \cdot e^{-BW_p} \left(\frac{W_p}{p_a} \right)^{\frac{1}{z}} \quad (C48)$$

where H, B and z represent constants for a given σ_3

$$f_p = \left(\frac{I_1^3}{I_3} - 27 \right) \left(\frac{I_1}{p_a} \right)^m \quad (C49)$$

$$f_p = \tilde{F}(W^p) \quad (C50)$$

Applying the consistency condition, equation (C16):

$$\frac{\partial \tilde{F}}{\partial W^p} dW^p = \frac{\partial f_p}{\partial \sigma_{ij}} d\sigma_{ij} \quad (C51)$$

$$\frac{\partial \tilde{F}}{\partial W^p} = He^{-BW^p} (-B) \left(\frac{W^p}{p_a} \right)^{\frac{1}{z}} + He^{-BW^p} \frac{1}{z} \left(\frac{W^p}{p_a} \right)^{\frac{1}{z}-1} = f_p [(-B)] + \frac{1}{z} \frac{p_a}{W^p} \quad (C52)$$

$$dW^p = \frac{df_p}{f_p \left(\frac{1}{z} \frac{p_a}{W^p} - B \right)} \quad (C53)$$

$$d\lambda_p = \frac{dW^p}{3g_p + m\eta_2 \left(\frac{p_a}{I_1}\right)^m I_3} \quad (C54)$$

Two parameters are involved in the stress-strain relationship: $d\lambda$ and η_2 . The value of $d\lambda$ determines the magnitude of the plastic strain increment, and the value of η_2 determines the directions of the strain increments. η_2 can be determined using

$\nu^p = -\frac{\Delta \epsilon_3^p}{\Delta \epsilon_1^p}$ and the flow rule (equation C32). Thus, η_2 is expressed as:

$$\eta_2 = \frac{3 \cdot (1 + \nu^p) \cdot I_1^2 - 27 \cdot \sigma_3 \cdot (\sigma_1 + \nu^p \cdot \sigma_3)}{\left(\frac{p_a}{I_1}\right)^m \cdot \left[\sigma_3 \cdot (\sigma_1 + \nu^p \cdot \sigma_3) - \frac{m \cdot (1 + \nu^p) \cdot I_1^2}{f_p \cdot (p_a / I_1)^m + 27} \right]} \quad (C55)$$

APPENDIX D NUMERICAL SIMULATION DETAILS

This section presents closed-form derivatives used in the numerical simulations (Closest Point Projection and Convex Cutting Plane algorithms).

Drucker-Prager Model Simulation

Closest Point Projection: Specific Characteristics

Closed-form solutions of the derivatives of the yield function for a Drucker-Prager model were computed and implemented in the numerical simulations (see Chapter 6).

The calculated derivatives with respect each principal stress are: $\frac{\partial f_{n+1}}{\partial \sigma_1} = \sqrt{2} - \alpha_{DP}$;

$$\frac{\partial f_{n+1}}{\partial \sigma_2} = \frac{\partial f_{n+1}}{\partial \sigma_3} = -\sqrt{2} - 2\alpha_{DP}; \text{ being } f_{n+1} = \sqrt{J_2} - \alpha_{DP}I_1 + k_{DP}, \alpha_{DP} \text{ and } k_{DP} \text{ material}$$

constants.

Lade Model Simulation

Closest Point Projection Applied to Lade Model: Isotropic Conditions

In order to evaluate the flow rule law residuals $\left(R_{n+1}^{(k)}\right)^T$, $\frac{\partial f}{\partial \sigma}$ and $\frac{\partial f}{\partial w_c}$ were

computed in closed-form using the contracted indices convention as:

$$\frac{\partial f}{\partial \sigma} = [2\sigma_1 \quad 2\sigma_2 \quad 2\sigma_3 \quad 0 \quad 0 \quad 0]; \quad \frac{\partial f}{\partial w_c} = -1, \text{ being } f(I_2, I_1, w_c) = I_1^2 + 2 \cdot I_2 - w_c, I_1$$

and I_2 the first and second invariant of the stress tensor, w_c work hardening.

The second derivatives used to determine the consistent tangent moduli, $[A_{n+1}^{(k)}]^{-1}$, were computed as

$$\partial^2_{\sigma\sigma} f_{n+1} = \begin{bmatrix} 2 & 0 & 0 & 0 & 0 & 0 \\ 0 & 2 & 0 & 0 & 0 & 0 \\ 0 & 0 & 2 & 0 & 0 & 0 \\ 0 & 0 & 0 & 0 & 0 & 0 \\ 0 & 0 & 0 & 0 & 0 & 0 \\ 0 & 0 & 0 & 0 & 0 & 0 \end{bmatrix}, \text{ and } \begin{cases} \partial^2_{w_c \sigma} f_{n+1} = [0 & 0 & 0 & 0 & 0 & 0] \\ \partial^2_{\sigma w_c} f_{n+1} = [0 & 0 & 0 & 0 & 0 & 0]^T \\ \partial^2_{w_c w_c} f_{n+1} = 0 \end{cases}$$

Here $\Delta\gamma_{n+1}\partial^2_{\sigma w_c} f_{n+1}$ and $\Delta\gamma_{n+1}\partial^2_{w_c \sigma} f_{n+1}$ differ by a transpose.

Convex Cutting Plane Algorithm Applied to Lade Model: Isotropic Conditions

The value of the hardening moduli was calculated as:

$$h_{n+1}^{(k)} = D_{n+1}^{(k)} \frac{\partial f_{n+1}}{\partial w_c} = -D_{n+1}^{(k)}, \text{ being } f(I_2, I_1, w_c) = I_1^2 + 2 \cdot I_2 - w_c$$

The increments to plastic consistency parameter, $\Delta^2\gamma_{n+1}^{(k)}$ were determined computing

$\frac{\partial f}{\partial \sigma}$ and $\frac{\partial f}{\partial w_c}$ in the same way as it was for the closest point projection algorithm, being:

$$\frac{\partial f}{\partial \sigma} = [2\sigma_1 \quad 2\sigma_2 \quad 2\sigma_3 \quad 0 \quad 0 \quad 0]; \quad \frac{\partial f}{\partial w_c} = -1$$

Convex Cutting Plane Algorithm Applied to Deviatoric Hardening Lade Model

Since the yield function for deviatoric conditions is:

$$f_n(I_3, I_1, w_n) = \left(\frac{I_1^3}{I_3} - 27 \right) \cdot \left(\frac{I_1}{p_a} \right)^m - w_n$$

The derivatives, $\frac{\partial f}{\partial \sigma}$ and $\frac{\partial f}{\partial w}$ were computed in closed-form as:

$$\left[\frac{\partial f}{\partial \sigma_1} \right] = \left[\frac{3 \cdot I_1^2 \cdot I_3 - I_1^3 \cdot \frac{I_3}{\sigma_1}}{I_3^2} \cdot \left(\frac{I_1}{p_a} \right)^m + \left(\frac{I_1^3}{I_3} - 27 \right) \cdot \frac{m}{p_a^m} \cdot I_1^{m-1} \right]$$

$$\left[\frac{\partial f}{\partial \sigma_2} \right] = \left[\frac{3 \cdot I_1^2 \cdot I_3 - I_1^3 \cdot \frac{I_3}{\sigma_2}}{I_3^2} \cdot \left(\frac{I_1}{p_a} \right)^m + \left(\frac{I_1^3}{I_3} - 27 \right) \cdot \frac{m}{p_a^m} \cdot I_1^{m-1} \right]$$

$$\left[\frac{\partial f}{\partial \sigma_3} \right] = \left[\frac{3 \cdot I_1^2 \cdot I_3 - I_1^3 \cdot \frac{I_3}{\sigma_3}}{I_3^2} \cdot \left(\frac{I_1}{p_a} \right)^m + \left(\frac{I_1^3}{I_3} - 27 \right) \cdot \frac{m}{p_a^m} \cdot I_1^{m-1} \right]$$

Using the contracted indices convention,

$$\frac{\partial f}{\partial \sigma} = \left[\frac{\partial f}{\partial \sigma_1} \quad \frac{\partial f}{\partial \sigma_2} \quad \frac{\partial f}{\partial \sigma_3} \quad 0 \quad 0 \quad 0 \right]$$

$$\frac{\partial f}{\partial w} = -1$$

APPENDIX E

PARAMETRIC STUDY OF THE HYDROSTATIC HARDENING LAW

Due to the fact that the accuracy of the simulation results presented in section 6.4.1 (Figure 6.8) was not satisfactory a more extensive investigation was done on the parameters that describe the hydrostatic plastic response of the material. Specifically, a parametric study was performed on d and U , the parameters involved in the formulation of the hardening law: $W = U \cdot p_a \left(\frac{f_c}{p_a} \right)^{\frac{1}{d}}$ (equation 4.12), where $f_c = 3\sigma_3^2$ represents the degree of hardening, U and d are material constants and p_a stands for the atmospheric pressure

While the parametric study on d indicated the best results for $d=1$, we have to remember that d was obtained together with U from a fit for the hardening function. That means that U (hardening constant) must change in order to fit the experimental behavior of the material. A fitting procedure (see chapter 4, section 4.7.1) was performed for the hardening function with $d=1$, showing no considerable change in the value of the constant U (with $d=0.913$, $U=0.0122$; and with $d=1$, $U=0.0122$, with only a small increase in the fitting error). Both fittings provided the same fitting errors, while the numerical simulations obtained with $d=1$ are closer to the experimental data then the one obtained for $d=0.913$ (see Section 6.4.1).

Figure F1 shows the influence of d in the simulations with d taking the values $d=\{0.91, 0.95, 0.99, 1, 1.01, 1.05, 1.09, 1.5\}$. As, can be observed the simulation results

present two regions, one with $d > 1$ and the other with $d < 1$. For d higher than 1, the results are grossly overestimated, approximately 20 times the mean pressure (see Figure E2), while for d less than 1, the simulations were closer to the experimental stresses as d was approaching 1 (see Figure E3).

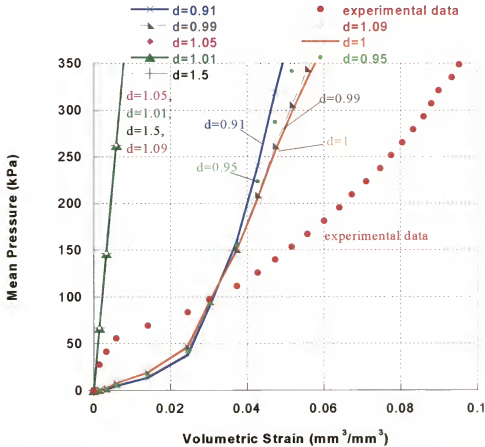


Figure E1: Mean stress vs. volumetric strain. Cutting plane algorithm. Silica's fit for elastic and hardening constants ($K_{\infty} = 2.5 \cdot 10^5$, $\psi = -1.399 \cdot 10^5$, $\beta = 1.21 \cdot 10^{-3}$, $U = 0.0122$, $d = [1.9-0.91]$). Effects of hardening constant (d) on silica powder simulation.

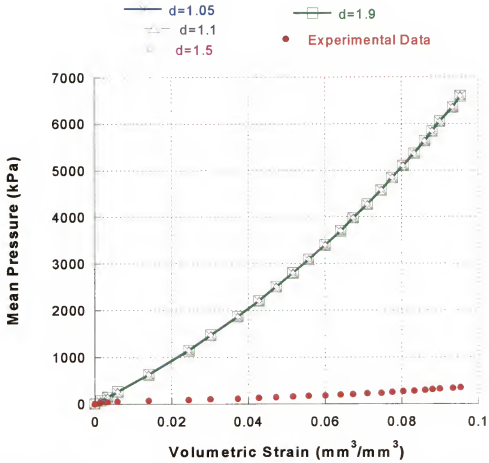


Figure E2: Mean stress vs. volumetric strain. Cutting plane algorithm. Silica's fit for elastic and hardening constants ($K_{\infty} = 2.5 \cdot 10^5$, $\psi = -1.399 \cdot 10^5$, $\beta = 1.21 \cdot 10^{-3}$, $U=0.0122$, $d=[1.9-0.91]$). Effects of hardening constant ($d>1$) on silica powder.

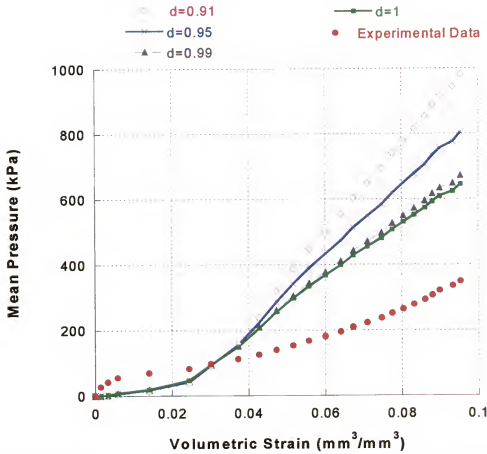


Figure E3: Mean stress vs. volumetric strain. CCP algorithm. Silica's fit for elastic and hardening constants ($K_{\infty} = 2.5 \cdot 10^5$, $\psi = -1.399 \cdot 10^5$, $\beta = 1.21 \cdot 10^{-3}$, $U=0.0122$, $d=[1.9-0.91]$). Effects of hardening constant ($d < 1$) on silica powder. Note that the closest values to those from the experiment are given by $d=1$ which implies constant values for D (plastic moduli).

The best results obtained from the CCP algorithm were achieved with $d=1$ and $U=0.122$.

REFERENCES

- Abdel-Hadi A. I., O.I. Zhupanska and N.D Cristescu, Mechanical Properties of Microcrystalline Cellulose. Part I. Experimental Results, *Mechanics of Materials*, **34** pp. 373-390 (2002).
- Abdel-Hadi A. I., N. D. Cristescu, O. Cazacu and R. A. Bucklin, Development of a New Technique for Measurement Volume Change of Dry Particulate Systems under Very Low Confining Pressures, *Recent Trends in Constitutive Modeling of Advanced Materials*, pp. 65-67 (2000).
- Adams M. J., Agglomerate Strength Measurement using a Uniaxial Confined Compression Test, *Powder Technology*, **78** pp. 5-13 (1993).
- Alawaji H., K. Runnesson, S. Sture and K Axelsson, Implicit Integration in Soil Plasticity under Mixed Control for Drained and Undrained Response, *International Journal of Numerical Analysis Methods*, **16** pp. 737-756 (1992).
- Aloufi M. and J. C. Santamarina, Low and High Strain Macrobbehavior of Grain Masses, *Transactions of the ASAE*, **38** (3) pp. 877-887 (1995).
- Aydin I., B. Bricoe and K. Y. Sanliturk, The Internal Form of Compacted Ceramic Components: A Comparison of a Finite Element Modeling with Experiment, *Powder Technology*, **89** pp. 239-254 (1996).
- Bagster D. F., P. C. Arnold, A. W. Roberts and T. F. Fitzgerald, The Interpretation of Ring Shear Cell Results, *Powder Technology*, **9** pp. 135-139 (1974).
- Baladi G. Y. and B. Rohani, An Elastic-Plastic Constitutive Model for Saturated Sand Subjected to Monotic and/or Cyclic Loadings, *3rd International Conference on Numerical Methods in Geomechanics*, pp. 389-404. Univ of Aachen, West Germany (1979).
- Baladi G. Y., CAP Model for Fitting the Stress-Strain Response of Houston and Reid Bedford Sands, *Constitutive Equations for Granular Non-Cohesive Soils*, A. Saada and G. Bianchini (eds), pp. 115-123, Balkema, Rotterdam (1988).
- Bardett J. P., Lode Dependencies for Isotropic Pressure-Sensitive Elastoplastic Materials, *Transactions of ASME, Journal of Applied Mechanics*, **57** (3) pp. 498-506 (1990).
- Bell T. A., B. J. Ennis, R. J. Grygo, W. J. F. Scholten and M. M. Schenkel, Practical Evaluation of the Johanson Indicizer, *Bulk Solids Handling*, **14** pp.117-125 (1995).

Bishop A. W. and D. J. Henkel, *The Measurements of Soil Properties in Triaxial Test*, pp. 228, Edward Arnold, 2nd edn, London (1962).

Blight G. E. and M. Gohnert, Effects of Varying Horizontal Pressures in Cylindrical Silos, *Powder Handling and Processing*, **5** (4) pp. 337-340 (1993).

Bock R. G., V. M. Puri and H. B. Manbeck, Triaxial Test Sample Size Effect on Stress Relaxation of Wheat en Masse, *Transactions of the ASAE* **34** (3) pp. 966-971 (1991).

Burland J. B., The Yielding and Dilation of Clay, *Geotechnique*, **15** (2) pp. 211-214 (1965).

Carr J. F. and D. M. Walker, An Annular Shear Cell for Granular Materials, *Powder Technology*, **1** pp. 369-373 (1967).

Cazacu O., J. Jin and N. D. Cristescu, A New Model for Alumina Powder Compaction, *Kona*, **15** pp.103-112 (1997).

Chen W. F. and W. O. McCarron, Modeling of Soils and Rocks Based on Concepts of Plasticity', Proc., *Symp. on Recent Developments in Laboratory and Field Test and Analysis of Geotechnical Problems*, pp. 467-510. Asian Institute of Technology, Bangkok, Thailand (1983).

Chou C. S., Interface between fluid-and solid-like behavior in rapid granular flows down bumpy inclines, *International Journal for Numerical and Analytical Methods in Geomechanics*, **23** pp. 1175-1194 (1999).

Chou C. S., J. Y. Hsu and Y. D. Lau, The Granular Flow in a Two-Dimensional Flat-Bottomed Hopper with Eccentric Discharge, *Physica A* **308** pp. 46-58 (2001).

Chtourou H., A. Gakwaya, M. Guillot and M. Hrairi, Implementing a Cap Model for the Simulation of Metal Powder Compaction, AMD, *Net Shape of Powder Materials, ASME* **216** pp. 19-25 (1995).

Chtourou H., A. Gakwaya and M. Guillot, Modeling of the Metal Powder Compaction Process Using the Cap Model. Part I. Experimental Material Characterization and Validation, *International Journal of Solids and Structures* **39** pp. 1059-1075 (2002).

Clower R. E., I. J. Ross and G. M. White, Properties of Compressible Granular Material as Related to Forces in Bulk Storage Structure, *Transactions of the ASAE* pp. 478-481 (1973).

Coulomb C., Application des Regles de Maximis a Quelques Problems de Statique Relatifs a l'architecture', Memoires desavants etrangers de l'Academie des Sciences de Paris (1773).

Crawford J. and P. Lindskog, Constitutive Equations and their role in the modeling of the cold pressing Process, *Scandinavian Journal of Metallurgy*, **12** pp. 271-281 (1983).

Cristescu N. D., *Rock Rheology*. Kluwer Academic Publishers, London (1989).

Daddazio R. P., M. M. Ettouney and I. S. Sandler, Nonlinear Dynamic Slope Stability Analysis, *Journal Geotech Engineering ASCE* **113** (4) pp.285-298 (1987).

DiMaggio F. L. and L.S. Sandler, Material Model for Granular Soils, *Journal of Engineering Mechanics Division, Proceedings of the ASCE*, **79** pp. 935-949 (1971).

Donsi G. and G. Ferrari, Improvement of the Bulk Properties, *Powder Technology*, **65** pp. 469-476 (1991).

Drescher A., *Analytical Methods in Bin-Load Analysis*, Elsevier, New York (1991).

Drucker D. C. and W. Prager, Soil Mechanics and Plastic Analysis or Limit Design, *Quarterly of Applied Mechanics*, **10** (2) pp. 157-165 (1952).

Drucker D. C. , R. E. Gibson and D. J. Henkel, Soil Mechanics and Plastic Analysis or Limit Design. *Trans.*, ASCE pp. 338-346 (1957).

Duncan J. M. and C. Y. Chang, Nonlinear Analysis of Stress and Strain in Soils, *Journal of Soil Mechanics and Foundations*, ASCE pp. 1629-1651 (1970).

Enstad G. G. and L. P. Maltby, Flow Property Testing of Particulate Solids, *Bulk Solids Handling*, **12** (3) pp. 451-455 (1992).

Geldhart D., Types of Gas Fluidization, *Powder Technology*, **7** pp. 285-292 (1973).

Genovese C., O. Cazacu and R. Bucklin, Experimental and Theoretical Investigation of the Behavior of Silica Powder under Compression, in: *4th World Congress On Particle Technology*, Sydney, Australia (2002).

Gerritsen A. H., *A Simple Method for Measurements Powder Flow Function with a View of a Hopper Design*, Preprints, Nuremberg, Germany, (1986).

Gethin D. T., R. W. Lewis, D. V. Tran and A. K. Ariffin, Finite Element Modeling of Multilevel Compaction of Powders, *Advances in Powder Metallurgy and Particulate Materials*, **7** pp. 13-22 (1994).

Gutfraind R. and O. Pouliquen, Study of the Origin of Shear Zones in Quasi-Static Vertical Chute flows by using Discrete Particle Simulations, *Mechanics of Materials* **24** pp. 273-285 (1996).

Hardin B. O., K. O. Hardin, I. J. Ross and S. V. Schwab, Triaxial Compression, Simple Shear and Strength of Wheat en Masse, *Transactions of the ASAE* **33** (90) pp. 933-942 (1990).

Jaeger H. M. and S. R. Nagel, The Physics of the Granular State, *Science* **255** pp. 1523-1531 (1992).

Jaeger H. M., S. R. Nagel and R. P. Behringer, The Physics of the Granular State, *Phys. Today* pp. 32-38 (1996).

Jansen H. Z., Versuche uber Gestreiderdruck in Silozellen, *Zeitschrift des VDI*, **39** pp. 1045-1049 (1895).

Jenike A. W., Gravity Flow of Bulk Solids, Bulletin 108, Utah Engineering Experiment Station, University of Utah, Salt Lake City, Utah (1961).

Jenike A. W., Storage and Flow of Solids, Bulletin 123, Utah Engineering Experiment Station, University of Utah, Salt Lake City, Utah (1964).

Jenkins J. T. and S.B. Savage, A Theory for the Rapid Flow of Identical, Smooth, Nearly Elastic, Spherical Particles. *J. Fluid Mech.*, **130** pp. 187-215 (1983).

Jenkins J. T. and M.W. Richman, Boundary Conditions for Plane Flows of Smooth, Nearly Elastic, Circular Disks, *J. Fluid Mech.*, **171** pp. 53-69 (1986).

Johanson J. R., The Johanson Indicizer System vs. the Jenike Shear Tester, *Bulk Solids Handling*, **12** (2) pp. 237-240 (1992).

Kamath S. and V. M. Puri, Measurement of Powder Flow Constitutive Model Parameters Using a Cubical Triaxial Cell, *Powder Technology*, **90** pp. 59-70 (1997).

Kim M. K. and P. V. Lade, Modeling Rock Strength in Three Dimensions, *International Journal of Rock Mechanics and Min. Sci. Geomech. Abstr.*, **21** (1) pp. 21-33 (1984).

Klausner J. D., D. Chen and R. Mei, Experimental Investigation of Cohesive Powder Rheology, *Powder Technology* **112** pp. 94-101 (2000).

Krieg R. D. and S. W. Key, Implementation of a Time Independent Plasticity Theory into Structural Computer Programs, *Constitutive Equations in Viscoplasticity*, ASME **20** pp. 125-137 (1976) .

Krieg R. D. and D. B. Krieg, Accuracies of Numerical Solution Methods for Elastic-Perfectly Plastic Model, *J. pressure Vessel Technology*, **99** pp. 510-515 (1977).

Lade P. V., Elasto-Plastic Stress-Strain Theory for Cohesionless Soil with Curved Yield Surface, *International Journal of Solids and Structures*, **13** pp. 1014-1035 (1977).

Lade P. V., Failure Criterion for Frictional Materials, *Mechanics of Engineering Materials*, pp. 385-402. C S Desai and R H Gallagher, eds., John Wiley and Sons, Inc., New York, N.Y. (1984).

Lade P. V. and J. M. Duncan, Cubical Triaxial Tests on Cohesionless Soil, *ASCE, Journal Geotechnical Engineering Division* **99** pp. 793-812 (1973).

Lade P. V. and J. M. Duncan, Elastoplastic Stress-Strain Theory for Cohesionless Soil, *J. Geotech. Eng. Div., ASCE*, **101** pp. 1037-1053 (1975).

Lade P. V. and J. M. Duncan, Stress-Path Dependent Behavior of Cohesionless Soil, *ASCE Journal Geotechnical Engineering Division*, **102** pp. 51-68 (1976).

Lade P. V. and S. Boonyachut, Large Stress Reversals in Triaxial Tests on Sand, in: *4th International Conference on Numerical Methods in Geomechanics*, Edmonton, Canada (1982).

Li Y., V. M. Puri and H. B. Manbeck, Elasto-Viscoplastic Cyclic Constitutive Model Parameter Determination and Evaluation for Wheat en Masse. *Transactions of the ASAE* **33** (6) pp. 984-995 (1990).

Lorenzen R. T., Effect of Moisture Content on Mechanical Properties of Small Grain. M S Thesis, University of California, California (1957).

Lun C. K. K., S. B. Savage, D. J. Jeffery and N. Chepurniy, Kinetics Theory for Granular Flow: Inelastic Particles, *J. Fluid Mech.*, **140** pp. 223-256 (1984).

Makino K. and K. Kuramitsu, Estimation Method of Powder Yield Locus, *KONA* **4** pp. 98-103 (1986).

Maltby L. P., Investigation of the Behavior of Powders under and after Consolidation, Telemark Institute of Technology, Porsgum, Norway (1993).

Medelson A., *Plasticity: Theory and Practice*, The Macmillan Company, New York, New York (1968).

Mei R., H. Shang, O. R. Walton and J. F. Klausner, Concentration Non-Uniformity in Simple Shear Flow of Cohesive Powders, *Powder Technology*, **112** pp. 102-110 (2000).

Minuzo E. and W.F. Chen, Plasticity Model and its Application to Geomechanics, *Proc. Symp. on Recent Developments in Laboratory and Field Tests and Analysis of Geomechanical Problems*, pp. 391-426. Rotterdam, The Netherlands (1984).

Molerus O., Effect of Interparticle Cohesive Forces on the Flow Behavior of Powders, *Powder Technology*, **20** pp. 161-175 (1978).

- Nedderman R. M., *Statics and Kinematics of Granular Materials*, Cambridge University Press, Cambridge (1992).
- Nelson R. B. and G.Y. Baladi, Outrunning Ground Shock Computed with Different Models, *Journal of Engineering Mechanics Division, ASCE*, **103** (3) pp. 377-393 (1977).
- Nova R. and D. M. Wood, Constitutive Model for Sand in Triaxial Compression, *International Journal Num. Meth. Geom.* **8** (1079) pp. 255-278 (1979).
- Nyssen C., An Efficient and Accurate Iterative Method Allowing Large Incremental Steps to Solve Elasto-Plastic Problem, *Comp. Struct.* **13**, pp. 63-71 (1981).
- Oka F. and T. Adachi, An Elastoplastic Constitutive Equation of Geologic Materials with Memory, *Proc. 5th Int. Conf. Numer. Meth. Geomech* pp. 293-300 (1985).
- Ortiz M., P. M. Pinsky and R. L. Taylor, Operator Split Methods for the Numerical Solution of the Elastoplastic Dynamic Problem, *Comp. Meth. Appl. Mech. Eng.*, **39** pp. 137-157 (1983).
- Ortiz M. and E. P. Popov, Accuracy and Stability of Integration Algorithms for Elasto-Plastic Constitutive Relations, *International Journal of Numerical Methods in Engineering*, **22** pp. 769-788 (1986).
- Ortiz M. and J.C. Simo, An Analysis of a New Class of Integration Algorithms for Elastoplastic Constitutive Relations, *International Journal of Numerical Methods in Engineering*, **23** pp. 353-366 (1986).
- Papadopoulos P. and R. L. Taylor, On the Application of Multi-Step Integration Methods to Infinitesimal Elasto-Plasticity, *International Journal of Numerical Methods in Engineering*, **37** pp. 3169-3184 (1994).
- Park H. and K. T. Kim, Consolidation Behavior of SiC Powder under Cold Compaction, *Materials Science and Engineering* pp. 116-124 (2001).
- Peric D. and M.A. Ayari, Influence of Lode's Angle on the Pore Pressure Generation in Soils, *International Journal of Plasticity*, **18** pp. 1039-1059 (2000a).
- Peschl I. A. S. Z., Equipment for the Measurement of Mechanical Properties of Bulk Materials, *Powder Handling and Proc.*, **1** pp. 73-81 (1989).
- Poorooshasb H. B., I. Holubec and A. N. Sherbourne, Yielding and Flow of Sand in Triaxial Compression: Part I, *Canadian Geotechnical Journal*, **III** pp. 179-190 (1966).
- Puri V. M., M. A. Tripodi, H. B. Manbeck and G. L. Messing, Constitutive Model for Dry Cohesive Powders with Applications to Powder Compaction, *Kona* **13** pp. 135-150 (1995).

Rankine W., On the Stability of Loose Earth. *Phil. Trans. Roy. Soc. London*, **147** pp. 9-28 (1857).

Rastogi S., S. V. Dhodapkar, E. Cabrejos, J. Baker, M. Weintraub and G. E. Klinzing, Survey of Characterization Techniques of Dry Ultrafine coals and their Relationship to Transport, Handling and Storage, *Powder Technology* **74** pp. 47-59 (1993).

Richards J. C. and R. L. Brown, *Principles of Powder Mechanics-Essays on the Packing and Flow Powders and Solids*, Pergamon press Ltd, Oxford (1970).

Rietma K., *The Dynamics of Fine Powders*, Elsevier (1991).

Roberts I., Determination of the Vertical and Lateral Pressures of Granular Substances, *Proceedings of the Royal Society of London*, **36** pp. 225-240 (1882).

Roscoe K. H. and J. B. Burland, On the Generalized Stress-Strain Behavior of Wet Clay. Engineering Plasticity, edited by J. Heyman and F. A. Leckie. Bentley House, London: Cambridge University Press (1968).

Roscoe K. H., A. N. Schofield and A. Thurairajah, Yielding of Clays in State Wetter than Critical, *Geotechnique*, **13**(3) pp. 211-240 (1963).

Ross I. J., The Forces Acting in Particles Stacks and the Capacity of Enclosed Screw conveyors, PhD Thesis, Purdue University, Lafayette, Indiana (1960).

Runesson K., M. Ristinmaa and L. Mahler, A Comparison of Viscoplasticity Formats and Algorithms, *Mech. Cohesive-Frictional Materials* **4** pp. 75-98 (1999).

Saada O., Assessment of the Flowability of Particulate Systems Using Triaxial Testing, Master thesis, University of Florida, Gainesville, Florida (1999).

Sandler I. S. and D. Rubin, An Algorithm and a Modular Subroutine for the Cap Model, *International Journal of Numerical Analysis Methods in Geomechanics* **3** pp. 173-186 (1979).

Savage S. B. and D. J. Jeffery, The Stress Tensor in a Granular Flow at High Shear Rates, *J. Fluid Mech.*, **110** pp. 255-272 (1981).

Savage S. B. and R. N. Yong, Stresses Developed by Cohesionless Granular Materials in Bins, *Intern. Journal Mech. Sci.* **11** pp. 595-602 (1970).

Saxena S. K., R. K. Reddy and A. Sengupta, Verification of a Constitutive Model for Granular Materials, *Constitutive Equations for Granular Non-Cohesive Materials*, A. Saada and G. Bianchini (eds), Balkema, Rotterdam (1988).

Schofield A. N. and C. P. Wroth, *Critical-State Soil Mechanics*, London, McGraw-Hill (1968).

Schulze D., Flowability and Time Consolidation Measurements Using a Ring Shear Tester, *Powder Handling and Processing*, **8** (3) pp. 221-226 (1996).

Schulze D. and J. Schwedes, Tests on the Application of Discharges Tubes. *Bulk Solids Handling*, **12** (1) pp. 33-39 (1992).

Schwedes D., Measurement of Flow Properties of Bulk Solids. *Powder Technology*, **88**, 285-290 (1996).

Shinohara K., *Handbook of Powder Science and Technology*, M.E. Fayed and L. Otten (Eds.). Van Nostrand Reinhold Comp, New York (1984).

Simo J. C. and T. J. R. Hughes, On the Variational Foundations of Assumed Strain Methods, *Journal of Applied Mechanics*, **53** pp. 51-54 (1986).

Simo J. C. and T. J. R. Hughes, *Computational Inelasticity*, Springer, Berlin (1998).

Sloan S. W., Sub-stepping Schemes for the Numerical Integration of Elasto-Plastic Stress-Strain Relations, *International Journal of Numerical Methods in Engineering*, **33** pp. 893-911 (1987).

Sridhar I. and N. A. Fleck, Yield Behavior of Cold Compacted Composite Powders, *Acta Materiala*, **48** pp. 3341-3352 (2000).

Stewart B. R., Q. A. Hossain and O. R. Krunze, Friction Coefficients of Sorghum Grain in Steel, Teflon and Concrete Surfaces, *Transactions of the ASAE* **11** pp. 260-262 (1968).

Tardos G., A Fluid Approach to Slow, Frictional Flow of Powders, *Powder Technology* **92** pp. 61-74 (1997).

Terzaghi K. and O. K. Peck, *Soil Mechanics in Engineering Practice*, New York, John Wiley (1948).

Thompson S. A. and I. J. Ross, Compressibility and Frictional Coefficients of Wheat. *Transactions of the ASAE* **26** (4) pp. 1171-1176 (1984).

Tomas J., Particle Adhesion Fundamentals and Bulk Powder Consolidation. *Powder Handling and Processing*, **12** (2) pp. 130-138 (2000).

Trasorras J., T. M. Krauss and B. L. Ferguson. Modeling of Powder Compaction Using the Finite Element Method, *Advances in Powder Metallurgy* **1** pp. 85-104 (1989).

Tripodi M. A., V. M. Puri, H. B. Manbeck and G. L. Messing, Triaxial Testing of Dry, Cohesive Powder and its Application to a Modified Cam-Clay Constitutive Model, *Powder Technology* **80** pp. 35-43 (1994a).

Tripodi M. A., V.M. Puri, H. B. Manbeck and G. L. Messing, Elastoplastic Finite Model Development and Validation for Low Pressure Uniaxial Compaction of Dry Cohesive Powders, *Powder Technology*, **85** pp. 241-251 (1994b).

Vermeer P. A., A Double Hardening Model for Sand, *Geotechnique* **28** pp. 413-433 (1978).

van der Kraan M., Techniques for the Measurements of the Flow Properties of Cohesive Powders, pp. 20-30. Delft University Press, TU Delft (1996).

von Karman T., 'Versuche unter allseitigem Druck, Mitteilungen über Forschungsarbeiten', *Ver. dtsch. Ing.* No. **118** (1911).

Wallin M. and M. Ristinmaa, Accurate Stress Updating Algorithm Based on Constant Strain Rate Assumption, *Comput. Methods Appl. Mech. Engrg.* **190** pp. 5583-5601 (2001).

Watson, M. J. Adams, S. L. Rough, B. J. Briscoe and T. Papathanasiou, The Modeling Influence of the Wall Friction on the Characteristics of Pressed Ceramics Parts, *Symposium on Mechanics of Granular and Porous Materials*, 415-426 (1997).

Wilkins M. L., *Calculation of Elastic-Plastic Flow*, Methods of Computational Physics 3, Academic Press, New York (1964).

Wilms H. and J. Schwedes, Interpretation of Ring Shear Tests, *Bulk Solids Handling* **5** (5) pp. 1017-1021 (1985).

Zhang Q., V. M. Puri, H. B. Manbeck and M.C. Wang, Elastoplastic Constitutive Parameters of en Masse Wheat for Cyclic Load Model, *Transactions of the ASAE*, **31** (3) pp. 910-917 (1988).

Zhang Q., V. M. Puri and H. B. Manbeck Finite Element Modeling of Thermally Induced Pressures in Grains Bins Filled with Cohesionless Granular Materials., *Transactions of the ASAE* **29** (1) pp. 248-256 (1986a).

Zhang Q., Y. Li, V. M. Puri and H. B. Manbeck, Physical Properties Effect on Stress-Strain Behavior of Wheat en Masse-Pat II Constitutive Elastoplastic Parameter Dependence on Initial Bulk Density and Moisture Content, *Transactions of the ASAE* **32** (1) pp. 203-209 (1989).

Zhang Q., V. M. Puri and H. B. Manbeck, Determination of Elastoplastic Constitutive Parameters for Wheat en Masse, *Transactions of the ASAE* **29** (6), 1739-1547 (1986b).

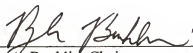
Zienkiewicz O. C., K. H. Leung and M. Pastor, Simple Model for Transient Soil Loading in Earthquake Analysis. I: Basic Model and its Application, *International Numer. Anal. Meth. Geomech.* **9** pp. 453-476 (1985).

Zienkiewicz O. C. and R. L. Taylor, *The Finite Element Method*, vol. **2**, McGraw-Hill, London (1991).

BIOGRAPHICAL SKETCH

Born and raised in Mar del Plata, Buenos Aires, Argentina, Claudia V. Genovese graduated in 1992 with a bachelor's degree in chemical engineering from National University of Mar del Plata. In 1998 she received her master's degree in chemical engineering from the same university in the specialty of waste-water treatment. Deciding to pursue a Ph.D in engineering science, in October 1998 she initially joined the food science group at the University of Florida. Since January 2000, she has worked with Dr. Ray Bucklin and Dr. Oana Cazacu to pursue her Ph.D in agricultural and biological engineering with a minor in food science.

I certify that I have read this study and that in my opinion it conforms to acceptable standards of scholarly presentation and is fully adequate, in scope and quality, as a dissertation for the degree of Doctor of Philosophy.



Ray A. Bucklin, Chair
Professor of Agricultural and Biological
Engineering

I certify that I have read this study and that in my opinion it conforms to acceptable standards of scholarly presentation and is fully adequate, in scope and quality, as a dissertation for the degree of Doctor of Philosophy.



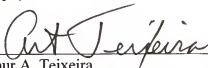
Oana Cazacu, Cochair
Assistant Professor of Mechanical and
Aerospace Engineering, Mechanics and
Engineering Science

I certify that I have read this study and that in my opinion it conforms to acceptable standards of scholarly presentation and is fully adequate, in scope and quality, as a dissertation for the degree of Doctor of Philosophy.




Nicolaie Cristescu
Graduate Research Professor of
Mechanical and Aerospace
Engineering, Mechanics and
Engineering Science

I certify that I have read this study and that in my opinion it conforms to acceptable standards of scholarly presentation and is fully adequate, in scope and quality, as a dissertation for the degree of Doctor of Philosophy.



Arthur A. Teixeira
Professor of Agricultural and Biological
Engineering

I certify that I have read this study and that in my opinion it conforms to acceptable standards of scholarly presentation and is fully adequate, in scope and quality, as a dissertation for the degree of Doctor of Philosophy.


Murat O. Balaban
Professor of Food Science and Human
Nutrition

This dissertation was submitted to the Graduate Faculty of the College of Engineering and to the Graduate School and was accepted as partial fulfillment of the requirements for the degree of Doctor of Philosophy.

August 2003


Pramod P. Khargonekar
Dean, College of Engineering


Winfred M. Phillips
Dean, Graduate School